elektronisches dokument
ULB Sachsen-Anhalt

Electronic Transport in Mesoscopic Systems

Dissertation

zur Erlangung des akademischen Grades
doctor rerum naturalium (Dr. rer. nat.)

vorgelegt der
Mathematisch-Naturwissenschaftlich-Technischen Fakultät
(mathematisch-naturwissenschaftlicher Bereich)
der Martin-Luther-Universität Halle-Wittenberg

von
Georgo Metalidis
geb. am 18. Juni 1980 in Genk, Belgien

Gutachter:

1. Prof. Dr. P. Bruno
2. Prof. Dr. I. Mertig
3. Prof. Dr. B. Kramer

Halle (Saale), den 31. Januar 2007

urn:nbn:de:gbv:3-000011374
[http://nbn-resolving.de/urn/resolver.pl?urn=nbn%3Ade%3Agbv%3A3-000011374]

Contents

Table of Contents i

Words of thanks v

Abstract vii

1 Introduction 1
- 1.1 General remarks 1
- 1.2 Purpose of this thesis 3

I Technicalities 5

2 Landauer-Büttiker formalism 7

3 Tight-binding model 11
- 3.1 Spin-degenerate system 11
  - 3.1.1 Generalities 11
  - 3.1.2 Inhomogeneous fields 13
- 3.2 Including spin degrees of freedom 14
  - 3.2.1 Zeeman/exchange splitting 15
  - 3.2.2 Spin-orbit coupling 15
  - 3.2.3 Rashba spin-orbit coupling 17

4 Green's function formalism 19
- 4.1 Green's functions: The basics 19
- 4.2 Transmission coefficients and the Green's function 20
- 4.3 Lattice Green's function method 21
  - 4.3.1 Semiinfinite leads: Self-energy description 22
  - 4.3.2 Recursive technique: Standard method 23
  - 4.3.3 Recursive technique: An extension 26

II Results **29**

5 Imaging coherent electron flow through a quantum point contact **31**
  5.1 Introduction . . . 31
  5.2 Experiment . . . 32
    5.2.1 Setup and measurement procedure . . . 32
    5.2.2 Experimental results . . . 33
  5.3 Numerical simulation: Imaging modes . . . 36
    5.3.1 Scanning probe used as a local scatterer . . . 36
    5.3.2 Scanning probe used as a local voltage probe . . . 38
    5.3.3 Current density in the absence of a tip . . . 41
  5.4 Numerical simulation: Device modeling . . . 43
    5.4.1 Tight-binding parameters for the 2DEG . . . 44
    5.4.2 Introducing disorder . . . 44
    5.4.3 Quantum point contact model . . . 45
  5.5 Simulation results . . . 46
    5.5.1 Modal pattern close to the QPC . . . 46
    5.5.2 Branching at larger distances from the QPC . . . 47
    5.5.3 Magnetic field influence . . . 51
    5.5.4 Double QPC setup . . . 54
  5.6 Conclusions . . . 56

6 Noncoherent effects in transport through a four-contact ring **59**
  6.1 Introduction . . . 59
  6.2 Modeling inelastic effects . . . 60
    6.2.1 Büttiker’s proposal . . . 60
    6.2.2 Tight-binding implementation . . . 62
  6.3 Transport in a four-contact ring . . . 64
    6.3.1 Hall effect without Lorentz force . . . 64
    6.3.2 An expression for the Hall resistance . . . 65
    6.3.3 Results . . . 66
  6.4 Conclusions . . . 68

7 Topological Hall effect **71**
  7.1 Introduction . . . 71
  7.2 Berry phase . . . 73
    7.2.1 Generalities . . . 73
    7.2.2 A simple example . . . 76
  7.3 Topological Hall effect . . . 77
    7.3.1 Theory . . . 77
    7.3.2 A first example . . . 80
  7.4 Transition between nonadiabatic and adiabatic regime . . . 83
    7.4.1 Adiabaticity criteria . . . 83
    7.4.2 Calculation of the Hall resistivity . . . 84

7.4.3 Results 85
7.5 Conclusions 87

8 Conclusions 89

Zusammenfassung 93

III Appendix 95

A Tight-binding model for the spin-orbit coupling Hamiltonian 97
A.1 Strictly two-dimensional system 97
A.2 Rashba spin-orbit coupling 99

B Surface Green’s function of a semiinfinite lead 101

C Derivation of the current density expressions 105
C.1 Current operator 105
C.2 Green’s function expression for the currents 107
C.2.1 Longitudinal current 108
C.2.2 Transverse current 110

D Persistent and transport contributions to the current density 111

E Efficient evaluation of the conductance decrease flow map 115

F Effective Hamiltonian for an electron in a magnetic texture 117

G Calculation of the Hall resistivity 121

Bibliography 125

Words of thanks

The preparation of a PhD thesis is not a completely independent accomplishment, and I should deeply thank a number of people. Without their support, this thesis would likely not have matured.

Basically, many thanks go out to my supervisor, Prof. Patrick Bruno, for freeing some time whenever I wanted to discuss, for showing me the light when I reached a dead end in my project, and for guiding me through the physics labyrinth in general. After our short cooperation during my master studies, I was convinced he would make an excellent PhD supervisor. Indeed, I can not be grateful enough for all the opportunities he has given me.

Many many thanks should also be sent to my family. My mother, for spending hours and hours on the telephone giving me support when I felt homesick or alone, when my work did not progress, or when I just felt blue. My father, for supporting me in everything I want to accomplish, also in physics: giving good advice on how to beat unwanted mesoscopic conductance fluctuations without ever hearing about the Schrödinger equation is quite something! Also my brother, for his many talks about cars (I should say, about Honda), about F1, or about which exhaust to fit on his Civic. And my sister, for making me feel not completely useless whenever I could help with her archeology studies, and for her kind words of reassurance in difficult times.

Two people are invaluable for the good operation of the theory department: thank you very much to our secretary Ina, and to Udo, our system administrator. Always friendly, always ready to help.

Thanks also to all the friends that I gained in the three years in Halle. Special mentions go out to “El Commandante” (Alex), “Salvatore” (Maged), and the “Panda” (Radu). We had a great time together, and I hope our roads will cross again somewhere, some time, maybe?

Katja, I believe I have found the missing piece of my puzzle…

Abstract

The phase coherence of charge carriers gives rise to the unique transport properties of mesoscopic systems. This makes them interesting to study from a fundamental point of view, but also gives these small systems a possible future in nanoelectronics applications.

In the present work, a numerical method is implemented in order to contribute to the understanding of two-dimensional mesoscopic systems. The method allows for the calculation of a wide range of transport quantities, incorporating a complete description of both the charge and spin degrees of freedom of the electron. As such, it constitutes a valuable tool in the study of mesoscopic devices. This is illustrated by applying the numerics to three distinct problems.

First, the method gives an efficient means of simulating recent scanning probe experiments in which the coherent flow of electrons through a two-dimensional sample is visualized. This is done by measuring the conductance decrease of the sample as a function of the position of a perturbing probe. For electrons passing through a narrow constriction, the obtained flow visualizations show a separation of the current into several branches, which is in agreement with experimental observations. The influence of a magnetic field on these branches is studied, and the formation of cyclotron orbits at the sample edges is visualized, although only after a new measurement setup is proposed. Furthermore, a wealth of interference phenomena are present in the flow maps, illustrating the coherent nature of electrons in the system.

Second, the numerical scheme also permits a phenomenological modeling of phase breaking scattering centers in the sample. As an application of this model, the influence of phase randomizing processes on the transport characteristics of a four-contact ring is investigated.

Third, transport of electrons through a noncoplanar magnetic texture is studied, and a Hall effect is observed even in the absence of a net Lorentz force and without invoking any form of spin-orbit coupling. This Hall effect is due to the Berry phase picked up by electrons when their spin follows the local magnetization direction. Using numerics in simple magnetic texture models, both the limit where the spin follows the magnetization adiabatically and its nonadiabatic counterpart can be addressed, including the effect of disorder. By investigating the transition between both limits, an ongoing discussion in the literature about the relevant adiabaticity criterion in the diffusive regime is clarified.

Chapter 1

Introduction

1.1 General remarks

Mesoscopic physics is most often referred to as the field studying systems with dimensions that are intermediate between the microscopic and the macroscopic. A more quantitative definition of the relevant length scale of a mesoscopic system is the phase coherence length, i.e., the length over which the carriers in the system retain their quantum-mechanical phase information. As such, mesoscopic phenomena can be observed in systems within a wide range of sizes going from the nanometer regime, to a few micrometers in high mobility semiconductor structures[1].

It is obvious then that mesoscopic systems will exhibit a behavior dictated by quantum (interference) effects, which makes them interesting already from a pure physical point of view. One of the landmark experiments in mesoscopic physics was the observation of the Aharonov-Bohm effect in the conductance of small metallic rings pierced by a magnetic flux through their center [1]. Since then, the field of mesoscopic transport physics has been growing exponentially, and a wide range of new physical concepts have been discovered: mesoscopic resistors in series do not follow simple addition rules [2, 3], the conductance of very narrow constrictions is quantized [4, 5], the conductance of disordered systems shows sample specific reproducible fluctuations with a universal amplitude [6], weak localization [7, 8], and many more. A good understanding of such new concepts has to be pursued not only because of fundamental research reasons, but also with an eye to future nanoscale devices. Indeed, the urge for miniaturization in electronic device technology will eventually lead to devices which approach mesoscopic dimensions so that engineers might have to cope with quantum transport in the future.

The sudden rise of mesoscopic physics has been fed by the development of high precision microfabrication processes. Molecular beam epitaxy (MBE), e.g., allows for fabricating semiconductor heterostructures with nearly single atomic layer precision. Electrons at the interface of a GaAs-AlGaAs heterostructure grown with MBE are effectively confined to move in two dimensions and create a two-dimensional electron gas (2DEG). In such a 2DEG, a wide variety of nanostructures can be defined using current state-of-the-art lithographic techniques: e.g., narrow constrictions (quantum point contacts), quantum dots, ring-shaped structures, and electron billiards to mention but a few. Furthermore, the extraordinary precision with which this can be done allows for creating all these structures with sizes smaller than the phase coherence length, and therefore the 2DEG became the perfect playground for mesoscopic physicists.

---

[1] Since the phase coherence length is sensitive to temperature, most experiments have to be done at low temperatures (liquid helium), in order to minimize the effect of phase breaking scattering events by phonons.

The ultimate limit in nanofabrication has been reached by using a scanning tunneling microscope (STM) to move around single atoms on a substrate [9]. More commonly, scanning probe methods are used in order to probe local sample properties: scanning tunneling and atomic force microscopes (AFM) allow to obtain a topographic image of the sample surface under study, and this with (near) atomic resolution. However, since a 2DEG is buried inside a heterostructure, other methods had to be developed in order to probe the behavior of electrons in such a system [10–13]. Very promising in this respect is a technique that is able to image the coherent flow of electrons through a 2DEG [14, 15]. It is based on perturbing the electron flow with an AFM tip, and simultaneously measuring conductance changes in the sample.

A recent development in nanoscale technology is the exploitation of the spin degree of freedom. The ultimate goal consists of developing a new kind of electronics, termed spintronics, that operates using both the spin and the charge of the electron. Compared to ordinary charge-based electronics, the spin degree of freedom can give extra functionality. Furthermore, because of long spin decoherence times, such devices could eventually also play a role in quantum computer architectures. Research into spintronics has been initiated in 1988, by the discovery of the giant magnetoresistance (GMR) effect [16, 17]. The GMR effect is a very large resistance increase of a ferromagnet/metal/ferromagnet multilayer structure when the magnetization of the magnetic layers changes from parallel to antiparallel. Only ten years after its discovery, this effect already found commercial applications in the form of read heads for harddisks, or magnetic field sensors. However, to really speak about spin electronics, one should be able to *transport* spins through a device, i.e., one should find a way to produce spin-polarized currents, and equally important, to detect such currents. It is clear that in order to pursue this goal, understanding how to control the spin degrees of freedom is of prime importance.

The most straightforward way to control the electron spin consists of making use of magnetic (or exchange) fields. For example, one might think of injecting a spin current from a ferromagnet into a semiconductor[2] [20]. Another example, from a more fundamental point of view, concerns using the Berry phase that electrons pick up while moving in an inhomogeneous field, and exploiting the resultant quantum interference effects in order to create new functionalities (see, e.g., the spin switch in Ref. [21]). A second possibility to control the electron spin, and one of great interest at present, is to exploit the coupling of the spin and orbital degrees of freedom of the electron (spin-orbit coupling). In this way, one has access to the spin via the orbital movement of the electron. Since the spin-orbit interaction is sensitive to electric fields, this would allow to control the electron spin fully electrically, without the need to use any magnetic material. Research in this direction has lead to a plethora of device proposals: e.g., the spin field effect transistor [22], and several spin interference based devices (see, e.g., Refs. [23, 24]). A very recent (r)evolution worth mentioning is the discovery of the so-called spin Hall effect, in which a longitudinal unpolarized charge current can induce a transverse pure spin current due to spin-orbit interactions [25–27].

---

[2] This is only efficient with a tunneling barrier between both materials [18, 19].

Several review papers on mesoscopic physics, nanoelectronics and spintronics [28–30]) together with some textbooks [2, 3, 31] have appeared in a rather short time span, proving that this is a rapidly developing, exciting and challenging area of physics, and will stay so for many more years.

1.2 Purpose of this thesis

The purpose of this thesis is to study mesoscopic transport phenomena in general, where we will restrict ourselves to two-dimensional systems like the ones created experimentally within a 2DEG. To reach this goal, we have chosen a numerical approach. It is based on a real space tight-binding description of the system under study, so it has the advantage that different system geometries are easily accessible. We are also able to take into account explicitly multiple leads that are attached to the sample: such leads are always present in a real experimental situation, and it is known that they can have a major impact on the transport properties in mesoscopic systems. Furthermore, the full influence of magnetic fields, both on the orbital and spin degrees of freedom, are correctly described. On top of that, spin-orbit interaction effects can also be implemented. All in all, this gives us a general purpose approach that can be used to attack a wealth of problems relevant to the fields of mesoscopic physics, nanoelectronics and spintronics. Although the basic philosophy behind our numerical approach is well known nowadays, we were able to extend the existing techniques allowing us to calculate a wider range of physical transport properties, and to do some calculations with far greater efficiency. All this will be made clear in the next three chapters where our numerical method is discussed in detail.

Subsequently, our method will be applied to three quite independent systems, which just shows the variety of problems that can be handled with our technique. In Chap. 5, we will consider scanning probe experiments that were used recently to image coherent flow of electrons through a narrow constriction [14, 15]. In particular, we will show that we are able to simulate such experiments very efficiently within our numerical framework. To aid in the interpretation of these experiments, we will also compare the experimentally measured quantity (a conductance decrease of the sample as a function of the position of the perturbing tip) with the exact current density in the sample. The influence of a magnetic field will also be studied, and the cyclotron orbits of the electrons moving through the sample are clearly observed. Furthermore, several interesting interference effects will be discussed.

In Chap. 6, we will show how our numerical method can lead to an efficient way of modeling phenomenologically the influence of phase coherence breaking scatterers. Doing so, the washing out of certain interference effects in a four-probe ring will be investigated.

Finally, in Chap. 7, electrons moving in an inhomogeneous magnetic texture are considered. The Berry phase that electrons pick up when their spin adiabatically follows the local magnetization direction during their movement can give rise to a Hall effect even when there is no net Lorentz force (nor any spin-orbit coupling) acting on the electrons. This recently discovered effect was termed "topological Hall effect" in the literature [32], and will be studied in detail in simple models in this thesis. The advantage of using numerics here lies in the fact that we can easily address the nonadiabatic limit, something which is much harder with analytical calculations.

Part I

Technicalities

Chapter 2

Landauer-Büttiker formalism

The transport properties of systems scaled down to the mesoscopic regime revealed quite a few surprises: e.g., the resistance of a ballistic waveguide was found to be nonzero and quantized as a function of its width [4, 5]. Another example is the appearance of discrete steps in the Hall resistance as a function of the applied magnetic field (quantum Hall effect[1]) [33], whereas classically one would expect this resistance to increase linearly with the field.

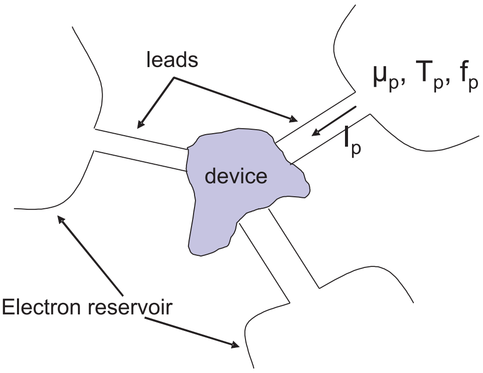

Figure 2.1: Setup for the Landauer-Büttiker formalism.

A widely used approach for understanding the peculiarities of mesoscopic transport is the so-called Landauer-Büttiker formalism [34, 35]. In this approach, the current through a sample is related to the probability for an electron to transmit through the sample, which is intuitively very appealing. Although the Landauer-Büttiker approach can be used for arbitrary dimensions, we will consider only two-dimensional samples, as depicted in Fig. 2.1. A central device is connected to semiinfinite leads that feed it with electrons from an electron reservoir. The

---

[1] Strictly speaking, one could argue that the quantum Hall effect is not a mesoscopic effect, since the effect is destroyed when the size of the system becomes smaller than the relevant quantum size in the problem, which in this case is the cyclotron radius of the magnetic field.

Landauer-Büttiker formulas then give a relationship between the currents flowing through the leads and the chemical potential of the reservoirs:

$$I_p = \frac{-e}{h} \sum_q \int \mathrm{d}E \, T_{pq}(E) \, \left[f_p(E) - f_q(E)\right], \tag{2.1}$$

where p, q label the different leads, $-e$ is the electronic charge, $f_p(E)$ is the Fermi-Dirac distribution for reservoir p (assumed to be in thermal equilibrium), and T_{pq} are the transmission coefficients for electrons to go from lead q to lead p.

For small biases between the reservoirs, this relationship can be linearized to obtain (we will also assume temperature $T = 0$ from now on)

$$I_p = \frac{e^2}{h} \sum_q T_{pq}(E_F) \, (V_p - V_q), \tag{2.2}$$

where $V_p = \mu_p/e$ is the voltage on reservoir p and E_F is the Fermi energy of the system. As such, the current-voltage characteristics of the device can be fully determined by calculating the transmission coefficients T_{pq} between all leads.

These transmission coefficients can be written as sums of transmission probabilities

$$T_{pq} = \sum_{m,n} \mid t^{pq}_{mn} \mid^2 \tag{2.3}$$

where t^{pq}_{mn} is the electron flux amplitude for an electron leaving the device through channel m in lead p, when the incoming flux amplitude in channel n in lead q is set to 1. In order to define such incoming and outgoing wave amplitudes, one needs the leads to be translationally invariant in the longitudinal direction. The channel indexes m, n then refer to both the discrete transverse modes of the leads (resulting from size quantization in the transverse direction) and the spin. The amplitudes t^{pq}_{mn} are thus nothing else than the elements of the scattering matrix of our system. Current conservation ($\sum_p I_p = 0$) is reflected in the unitarity of the scattering matrix, and it leads to the following constraint for the transmission coefficients T_{pq}:

$$\sum_p T_{pq}(E) = \sum_p T_{qp}(E). \tag{2.4}$$

It is clear that the Landauer-Büttiker approach is only valid for phase coherent (i.e., mesoscopic) devices, otherwise the description in terms of in- and outgoing waves loses its validity. Nevertheless, it is important to note that inelastic effects are taking place inside the electron reservoirs, because they have to maintain an equilibrium distribution even in the presence of transport. As such, energy dissipation is taking place in the reservoirs only.

A final point to mention are the following symmetry relations for the transmission coefficients under time reversal:

$$T_{pq}(+\mathbf{B}) = T_{qp}(-\mathbf{B}). \tag{2.5}$$

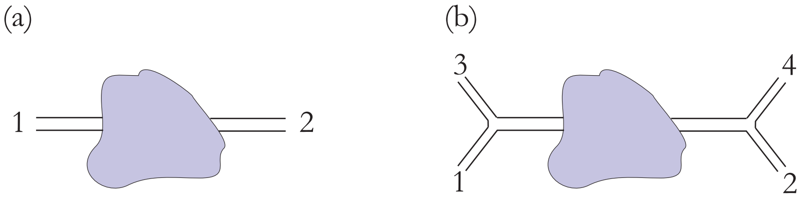

Figure 2.2: Two-terminal (a) and four-terminal (b) measurement setups for obtaining the resistance of a mesoscopic sample.

For a two-probe measurement as in Fig. 2.2(a), they lead [together with Eq. (2.4)] to $T_{12}(+\mathbf{B}) = T_{12}(-\mathbf{B})$, giving a sample resistance that is symmetric under time reversal. On the other hand, when multiple leads are connected to the device, the situation becomes slightly more complicated. Experimentally, e.g., one uses quite often a four-terminal geometry as in Fig. 2.2(b) where two leads (labeled 1 and 2) are used to pass current through the sample and two other leads (labeled 3 and 4) are used to measure the voltage drop over the sample. In this case, the measured resistance $R_{12,34} = \frac{V_4 - V_3}{I_1}$ is not symmetric with respect to time reversal. Instead, based on Eqs. (2.2) and (2.5), a symmetry relation can be derived between two measurements in which the role of current and voltage leads are reversed [36]:

$$R_{12,34}(+\mathbf{B}) = R_{34,12}(-\mathbf{B}). \tag{2.6}$$

It thus becomes clear that the measurement setup itself plays an important role in mesoscopic transport. One of the strong points of the Landauer-Büttiker formalism is that it allows to take the role of the current/voltage probe configuration explicitly into account so that one is able to closely mimic a real experimental setup. Therefore, coupled with its intuitive appeal, the formalism has found widespread use and some major developments in the mesoscopic transport theory are centered around it: e.g., both the quantum Hall effect and the nonzero resistance of a ballistic conductor can be explained with it.

Chapter 3

Tight-binding model

For the numerical calculation of physical quantities, such as the transmission coefficients in the Landauer-Büttiker formulas, it is convenient to have a numerical representation of the problem that is easy to use and of sufficiently general purpose. In this chapter, a tight-binding representation is seen to fulfill such requirements.

The tight-binding model of a system is obtained by discretizing its Hamiltonian on a lattice. The smaller one chooses the lattice cell size, the better this representation represents the continuum limit. As such, not every lattice site corresponds to an atom as in ab-initio theories; rather a site may represent a region containing many atoms, but this region should be small compared to physically relevant quantities such as the Fermi wavelength.

Although this kind of tight-binding approach is widely used nowadays, some new viewpoints will be presented in this chapter, e.g., considering a gauge for describing inhomogeneous fields, and the description of spin-orbit coupling. The application of the tight-binding approach to spin-dependent transport calculations will be treated in some detail since this is a more recent development, while spin-degenerate systems are only briefly discussed because their treatment can be found in textbooks nowadays (see, e.g., Ref. [2]).

3.1 Spin-degenerate system

3.1.1 Generalities

The Hamiltonian for a spinless electron in a two-dimensional system moving in a magnetic field is given by

$$H = \frac{1}{2m^*}\Big(\mathrm{i}\hbar\nabla - e\mathbf{A}\Big)^2 + V, \tag{3.1}$$

where m^* and $-e$ are the effective mass and the electronic charge respectively. The potential V comprises both the potential that confines the electrons and the one due to impurities (disorder) in the system. The vector potential $\mathbf{A}$ describes the influence of a magnetic field $\mathbf{B} = \nabla \times \mathbf{A}$. Since we are considering a 2D system, only fields applied perpendicular to the sample will have an influence on the orbit of the electron.

The general scheme for discretizing this Hamiltonian looks as follows. First, one constructs a square lattice with lattice parameter a by defining points $(n,m) = (x\!=\!na, y\!=\!ma)$ with n and m integer. By approximating the derivative operators on this lattice as $\partial_x f = 1/a[f(x\!+\!a/2)-f(x\!-\!a/2)]$ (and an equivalent expression for $\partial_y f$), one can show that the Hamiltonian (3.1) can be mapped onto a nearest-neighbor tight-binding Hamiltonian [2]

$$\begin{aligned}\mathcal{H} &= \sum_n\sum_m \left[t^x_{nm}\,|n+1,m\,\rangle\langle\,n,m| + t^y_{nm}\,|n,m+1\,\rangle\langle\,n,m| + \text{H.c.}\right] + \\ &\qquad + \sum_n\sum_m \epsilon_{nm}\,|n,m\,\rangle\langle\,n,m|, \qquad (3.2)\end{aligned}$$

that acts in the discrete space spanned by the states $|n,m\,\rangle = |x=na, y=ma\,\rangle$.

The on-site energies ϵ_{nm} in this Hamiltonian are

$$\epsilon_{nm} = 4t + V_{nm}, \qquad (3.3)$$

with $V_{nm} = V(na,ma)$. They have been shifted up by an amount $4t$ so that the energy band for free electrons ($V = 0$) in an infinite lattice,

$$\varepsilon = 2t\big(2-\cos k_x a - \cos k_y a\big), \qquad (3.4)$$

has a value of zero at the bottom. The k_x and k_y are wavevectors belonging to the first Brillouin zone of the square lattice. It can be seen that the tight-binding model is a good approximation only when $k_x a, k_y a \ll 1$, i.e., when the lattice spacing is smaller than the Fermi wavelength, since the dispersion relation then becomes approximately parabolic like in the continuum case.

The quantities t^x_{nm} and t^y_{nm} in the tight-binding Hamiltonian give the hopping amplitude in the horizontal, respectively vertical direction. In the absence of a magnetic field they are given by:

$$t^x_{nm} = t^y_{nm} = -t = -\frac{\hbar^2}{2m^* a^2}. \qquad (3.5)$$

When the vector potential $\mathbf{A}$ is included, the hopping parameters change to

$$t^{x(y)}_{nm} = -t\, e^{-\mathrm{i}\, e/\hbar \int \mathbf{A}.\mathrm{d}\mathbf{l}}, \qquad (3.6)$$

where $\int \mathbf{A}\,.\,\mathrm{d}\mathbf{l}$ is the integral of the vector potential along the hopping path[1]. This is called the Peierls substitution [38, 39]. Given a certain magnetic field distribution, we still have the freedom to choose the gauge for the vector potential that suits best to our needs. One very convenient gauge for representing a homogeneous field $B\mathbf{e_z}$

---

[1] A lucid discussion on the physics of Eq. (3.6) is given in Ref. [37] on page 21-2.

is the Landau gauge: $\mathbf{A} = -By\mathbf{e_x}$. In this gauge, the hopping parameters found from Eq. (3.6) are explicitly given by

$$t^x_{nm} = -t\, e^{\mathrm{i}2\pi(m-1)\Phi/\Phi_0}, \tag{3.7a}$$

$$t^y_{nm} = -t, \tag{3.7b}$$

where we have defined $\Phi = Ba^2$ as the magnetic flux per lattice cell, and $\Phi_0 = h/e$ the magnetic flux quantum. This gauge is particularly interesting for describing fields in the leads because it conserves translational invariance along the X axis. Choosing in every lead a coordinate system with the local X axis pointing along the longitudinal direction[2], the conservation of translational invariance along this axis assures that one is still able to speak of in- and outgoing waves in the leads, which is necessary to define the transmission coefficients in the Landauer-Büttiker formalism [see Eq. (2.3) and the discussion thereafter].

3.1.2 Inhomogeneous fields

The Peierls substitution method gives a very convenient way of dealing with magnetic fields in a tight-binding model. However, although the Landau gauge proved to be very convenient for describing homogeneous fields, it is not always clear what gauge to choose for more exotic field distributions. It is for instance not obvious how the vector potential $\mathbf{A}$ should look like when one has a completely random magnetic field in the device.

Nevertheless, we have found a convenient gauge for any possible field distribution, as will be explained with the help of Fig. 3.1. Suppose that one has a perpendicular magnetic field with strength B that is localized on a single lattice cell. The influence of this local field can be described by changing all the hopping parameters t^x_{mn} *above* the flux tube as follows:

$$t^x_{nm} \to -t\, e^{\mathrm{i}2\pi\Phi_1/\Phi_0}, \quad \text{for } m > m_1, \tag{3.8}$$

where Φ_1 is the magnetic flux enclosed by the unit cell: $\Phi_1 = B_1 a^2$. An electron traveling along any closed path around the flux tube will then pick up a phase $2\pi\Phi_1/\Phi_0$, thus giving a correct description of the field. A second localized flux tube in the same column will contribute another phase change Φ_2, but again only to the hopping parameters *above* the second flux tube. The total change of the hopping parameters is then the sum of both contributions (see Fig. 3.1):

$$t^x_{nm} \to \begin{cases} -t & , m < m_1 < m_2 \\ -t\, e^{\mathrm{i}2\pi\Phi_1/\Phi_0} & , m_1 < m \leq m_2 \\ -t\, e^{\mathrm{i}2\pi(\Phi_1+\Phi_2)/\Phi_0} & , m_1 < m_2 < m \end{cases} \tag{3.9}$$

---

[2] A proof that the gauge for the vector potential can indeed always be chosen to be Landau-like in every lead is given in Ref. [40].

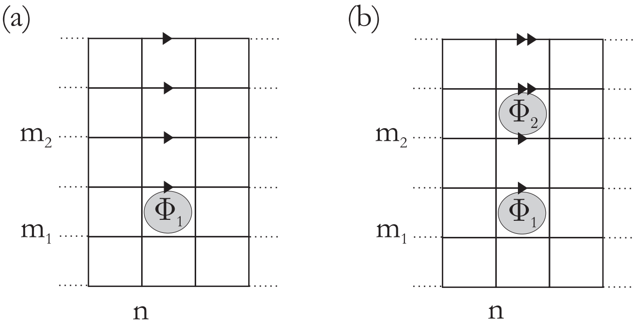

Figure 3.1: An arbitrary magnetic field is composed of flux tubes localized on single lattice cells. For a single flux tube, all hopping parameters above it change their phase by ϕ_1 [single arrow in (a)]. If a second flux tube is included above the first one, hopping parameters located above both cells will change their phase by $\phi_1 + \phi_2$ [double arrows in (b)].

This line of reasoning can be easily generalized to a situation where every unit cell encompasses a single flux tube. One just changes the hopping parameters as:

$$t^x_{nm} \to -t\, e^{\mathrm{i}2\pi \sum_{m'<m} \Phi_{nm'}/\Phi_0}, \tag{3.10}$$

where $\Phi_{nm'}$ is the flux through the lattice cell above the link connecting site (n, m') with site $(n+1, m')$. As such, one can describe an arbitrary magnetic field in the device by choosing the appropriate flux tube distribution through the different lattice cells.

From comparison with Eq. (3.6), the description above corresponds to choosing the following gauge for the vector potential:

$$\begin{array}{lcc} A^x_{n\leftrightarrow n+1,m} & = & -\frac{1}{a}\sum_{l<m}\Phi_{nl} \\ A^y & = & 0 \end{array}, \tag{3.11}$$

where $A^x_{n\leftrightarrow n+1,m}$ is the vector potential at the vertex connecting sites (n, m) and $(n+1, m)$. Note that for a homogeneous field where all lattice cells comprise the same flux $\Phi_{nm} = \Phi = Ba^2$, the gauge choice above corresponds to the Landau gauge.

3.2 Including spin degrees of freedom

When including spin in the problem, the state space will be extended: it is now spanned by product states $|n, m, \sigma\rangle = |n, m\rangle \otimes |\sigma\rangle$, where $|\sigma\rangle$ defines the spin state of the electron. In a matrix representation of the Hamiltonian, this means that every element of the "spinless" representation now becomes a 2×2 spin matrix itself.

When treating the spin-independent terms in the Hamiltonian, this spin matrix is proportional to the identity matrix. In other words, the Hamiltonian $\mathcal{H}$ in

Eq. (3.2) can be written to act in the extended space by just putting $\mathcal{H} \rightarrow \mathcal{H} \otimes \mathbf{1}$ with $\mathbf{1}$ the identity matrix, and no extra work is needed for finding a tight-binding description for the spin-degenerate Hamiltonian. For operators acting on the spin degrees of freedom however, we still have to derive a tight-binding representation. In the next sections, this will be done for both the Zeeman (or exchange) splitting and spin-orbit coupling terms.

3.2.1 Zeeman/exchange splitting

In a preceding section we discussed the influence of a magnetic field on the orbit of the electron and described it by the Peierls substitution. However, the effect of the field on the spin of the electron was neglected. In fact, an extra term

$$H_S = -\frac{1}{2}\, g^* \mu_B \, \mathbf{B}_{\text{eff}} \cdot \boldsymbol{\sigma}, \tag{3.12}$$

should be added to the Hamiltonian, where g^* is the effective Landé factor for the electron and μ_B is the Bohr magneton, while $\boldsymbol{\sigma}$ is a vector containing the Pauli spin matrices: $\boldsymbol{\sigma} = (\sigma^x, \sigma^y, \sigma^z)$. We have written the field as an effective field $\mathbf{B}_{\text{eff}}$, to make it clear that it can be due to an externally applied field, an exchange field (in a ferromagnet, e.g.), or a combination of both. This Hamiltonian will split the energy bands: a spin-up state (with respect to $\mathbf{B}_{\text{eff}}$) will be shifted down in energy by $1/2\, g^* \mu_B \|\mathbf{B}_{\text{eff}}\|$, while a spin-down state will be shifted up by the same amount.

Since it only acts in spin space, this operator will lead to an on-site term in the tight-binding Hamiltonian:

$$\mathcal{H}_S = -\frac{1}{2} g^* \mu_B \sum_{n,m} |n,m\,\rangle\langle\, n,m| \otimes \big(\mathbf{B}^{\text{eff}}_{nm} \cdot \boldsymbol{\sigma}\big), \tag{3.13}$$

with $\mathbf{B}^{\text{eff}}_{nm} = \mathbf{B}_{\text{eff}}(x\!=\!na, y\!=\!ma)$. It should be noted that the orbit of the electron is only influenced by the component of the magnetic field perpendicular to the 2D sample, while the spin splitting of course depends on all three components of the field.

3.2.2 Spin-orbit coupling

When a particle with spin moves in an electric field, its spin and orbital degrees of freedom will be coupled. This so-called spin-orbit interaction is essentially a relativistic effect, and gives rise to a Hamiltonian of the form

$$H_{\text{SO}} = \lambda\, \mathbf{P} \cdot \big(\nabla V \times \boldsymbol{\sigma}\big), \tag{3.14}$$

where V is the electrostatic potential felt by the electron, and $\mathbf{P}$ the mechanical momentum operator. The parameter λ is a material constant describing the strength of the coupling.

Instead of deriving this Hamiltonian explicitly by making an expansion in v/c of the Dirac equation, we will give some physical arguments as to why a Hamiltonian of the form above can be expected. Suppose an electron moves with velocity $\mathbf{v}$ in an electric field $\mathbf{E}$. Doing a Lorentz transformation to its rest frame, the electron feels a magnetic field (to first order in v/c)

$$\mathbf{B} = -\frac{1}{c^2}(\mathbf{v} \times \mathbf{E}). \tag{3.15}$$

The magnetic moment of the electron can interact with this field, giving rise to a Zeeman-like term

$$H_{\text{SO}} = -\frac{1}{2}\, g^* \, \mu_B \, \mathbf{B} \cdot \boldsymbol{\sigma}. \tag{3.16}$$

Substituting the magnetic field in this expression with Eq. (3.15), and using that $\mathbf{v} = \mathbf{P}/m^*$, one obtains finally

$$H_{\text{SO}} = g^* \frac{e\hbar}{4{m^*}^2 c^2} \big(\mathbf{P} \times \mathbf{E}\big) \cdot \boldsymbol{\sigma}. \tag{3.17}$$

Writing the electric field as $\mathbf{E} = \nabla V/e$, with V the electrostatic potential, this indeed leads to a spin-orbit Hamiltonian of the form (3.14), with the parameter λ given by[3]

$$\lambda = \frac{g^* \hbar}{4{m^*}^2 c^2}. \tag{3.18}$$

In a strictly 2D system, the electrostatic potential V depends only on the coordinates (x, y). In this case, we can write the spin-orbit Hamiltonian (3.14) as

$$H_{\text{SO}} = \lambda\, \sigma^z \left[\left(\frac{\hbar}{\mathrm{i}} \partial_x + eA^x \right) \partial_y V - \left(\frac{\hbar}{\mathrm{i}} \partial_y + eA^y \right) \partial_x V \right], \tag{3.19}$$

where we used $\mathbf{P} = \mathbf{p} + e\mathbf{A} = \frac{\hbar}{\mathrm{i}}\nabla + e\mathbf{A}$ for the mechanical momentum. For deriving the tight-binding version of the Hamiltonian (3.19), we need to discretize this operator on a lattice. Since this involves quite a few technical operations, we have shifted such a discussion into Appendix A. The end result is:

$$\begin{aligned} \mathcal{H}_{\text{SO}} = \frac{\lambda\hbar}{2a} \sum_{n,m} \Bigg\{ & [\partial_x V]_{n,m\leftrightarrow m+1} \Big(|n, m\rangle\langle n, m+1| \otimes \mathrm{i}\sigma^z \Big) \qquad (3.20) \\ & -[\partial_y V]_{n\leftrightarrow n+1,m}\; e^{-\mathrm{i}\,2\pi \sum_{l<m} \frac{\Phi_{n,l}}{\Phi_0}} \Big(|n, m\rangle\langle n+1, m| \otimes \mathrm{i}\sigma^z \Big) + \text{H.c.} \Bigg\}, \end{aligned}$$

---

[3] In our naive derivation, we did not treat the Lorentz transformation between the lab frame and the electron's rest frame completely correctly. An electron moving in an electric field that has a component perpendicular to the electron's velocity describes a curved trajectory. The transformation between the lab frame and the electron's rest frame therefore involves two noncollinear Lorentz transformations. As a consequence, an observer in the electron's rest frame will find that an additional rotation is necessary to align his axes with the axes obtained by just boosting the labframe using the instantaneous velocity of the electron. This results in an extra precession of the electron spin, called Thomas precession. The effect changes the magnitude of the interaction in Eq. (3.16), and will introduce a factor of 1/2 in the expression for λ. We will assume this factor to be absorbed in the definition of g^*. For a more thorough discussion, see, e.g., Ref. [41].

with the derivatives of the potential on the vertices defined as

$$[\partial_y V]_{n\leftrightarrow n+1,m} \approx \frac{1}{2a}\left[\frac{1}{2}\Big(V_{n,m+1}+V_{n+1,m+1}\Big)-\frac{1}{2}\Big(V_{n,m-1}+V_{n+1,m-1}\Big)\right]$$
$$[\partial_x V]_{n,m\leftrightarrow m+1} \approx \frac{1}{2a}\left[\frac{1}{2}\Big(V_{n+1,m}+V_{n+1,m+1}\Big)-\frac{1}{2}\Big(V_{n-1,m}+V_{n-1,m+1}\Big)\right].$$

This Hamiltonian describes a spin-dependent hopping to nearest neighbor sites, clearly illustrating the coupling between spin and orbital degrees of freedom. Upon hopping in the X direction to a neighboring site, the electron will pick up the same phase factor that was due to the presence of a magnetic field (see Sec. 3.1.2).

3.2.3 Rashba spin-orbit coupling

Experimentally, a two-dimensional electron gas is often created at the interface of a semiconductor heterostructure. Electrons are then confined by an approximately triangular potential well $V(z)$ in the growth direction (see Fig. 3.2). If this well is narrow enough electrons will only occupy the lowest eigenstate and the movement along the Z direction is effectively frozen out so that electrons are only free to move in a two-dimensional plane.

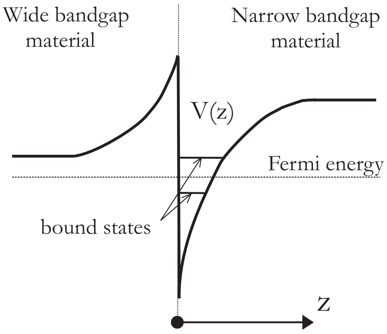

Figure 3.2: Conduction band at the interface of a semiconductor heterostructure. Band bending creates a potential well $V(z)$ confining the electrons to the XY plane. The asymmetry of this well leads to Rashba spin-orbit coupling.

However, the influence of the triangular potential well goes further than confining the electrons in a plane: it can give rise to the so-called the Rashba spin-orbit interaction [42, 43]. Indeed, the potential well $V(z)$ has a nonzero gradient and it will give rise to a spin-orbit coupling according to Eq. (3.14):

$$H_{\text{RSO}} = \lambda \frac{\mathrm{d}V}{\mathrm{d}z}\mathbf{P}\cdot\big(\mathbf{e}_z\times\boldsymbol{\sigma}\big). \tag{3.21}$$

When the well is not exactly triangular, the gradient $\frac{\mathrm{d}V}{\mathrm{d}z}$ is not constant and one has to calculate an average, using the density distribution for electrons in the Z direction as a weight function. Writing out the cross-product in Eq. (3.21), one obtains an expression for the Rashba term of the form

$$H_{\text{RSO}} = \frac{\alpha}{\hbar}\left(P_y\sigma^x - P_x\sigma^y\right), \tag{3.22}$$

where $\alpha = \lambda\hbar\left\langle \mathrm{d}V/\mathrm{d}z \right\rangle$ is a material parameter that contains the details of the averaging procedure described above. It is clear that α will only be different from zero when the confining potential is not symmetric. In real heterostructures, α can take on typical values in the range of 1 to 10×10^{-10} eVcm for a large variety of systems (mostly used are GaAs/AlGaAs and InAs/InAlAs heterostructures), depending on the exact shape of the confining potential well. It should be noted that the shape of the confining well, and thus the coupling strength α can be varied by applying a voltage on an electrostatic gate mounted on top of the electron gas [44, 45]. This gives some control on the strength of the spin-orbit interaction and it has lead to proposals for a variety of devices based upon controlling the spin degrees of freedom electrically (rather than with magnetic fields) via the Rashba spin-orbit coupling. Most famous among these is the spin field effect transistor [22].

The tight-binding representation for the Rashba Hamiltonian in Eq. (3.22) is derived in full detail in Appendix A. We only state the end result here:

$$\begin{aligned}\mathcal{H}_{\text{RSO}} = -t_{\text{SO}}\sum_{n,m}\Bigg\{ & e^{-\mathrm{i}2\pi\sum_{l<m}\Phi_{n,l}/\Phi_0}\Big(|n,m\rangle\langle n+1,m|\otimes \mathrm{i}\sigma^y\Big) \\ & -\Big(|n,m\rangle\langle n,m+1|\otimes \mathrm{i}\sigma^x\Big) + \text{H.c.}\Bigg\},\end{aligned} \tag{3.23}$$

where we have defined $t_{\text{SO}} = \alpha/2a$. The Rashba Hamiltonian thus describes a hopping between neighboring sites paired with a spin flip. Again, a phase factor is picked up when hopping in the X direction in the presence of a magnetic flux.

Chapter 4

Green’s function formalism

Having a numerical representation of the system in terms of a tight-binding model, one still needs a mathematical framework within which different physical properties can be calculated. Green’s functions can be a valuable tool in this respect. One of their advantages is the relative ease with which they can be calculated, compared to a direct numerical solution of the Schrödinger equation. In particular, a very efficient recursive method is available for obtaining the Green’s functions necessary for the evaluation of the transmission coefficients in the Landauer-Büttiker formalism [2, 31]. This method will be discussed in some detail in the current chapter, where parts of the discussion will follow Refs. [2, 31]. We will also show how to extend this standard recursive technique, allowing for an extra set of Green’s functions to be calculated with the same high efficiency. With this larger set of Green’s functions, a wider range of physical properties comes in our reach, but it will also allow us to do certain calculations in the next chapters more efficiently.

4.1 Green’s functions: The basics

In quantum physics, the single-particle Green’s function operator $\widehat{G}(E)$ of a system described by a Hamiltonian $\widehat{H}$ can be defined as the solution to the operator equation [2, 31, 46]

$$\big[E - \widehat{H}\big]\,\widehat{G}(E) = 1, \tag{4.1}$$

A formal solution to this equation would be given by $\widehat{G}(E) = (E - \widehat{H})^{-1}$. However, such a solution is not well defined for values of E corresponding to the eigenvalues of the Hamiltonian. This subtlety can be appreciated more when going to the position-spin representation of Eq. (4.1):

$$\big[E - H(\mathbf{x})\big]\,G(\mathbf{x},\mathbf{x}',E) = \delta(\mathbf{x}-\mathbf{x}'). \tag{4.2}$$

The vector $\mathbf{x}$ contains both the position and spin variables $\mathbf{x} = (\mathbf{r},\sigma)$, and the function

$$G(\mathbf{x},\mathbf{x}',E) = \langle\,\mathbf{x}|\widehat{G}(E)|\mathbf{x}'\,\rangle \tag{4.3}$$

is called the Green's function of the system. From Eq. (4.2), it can be seen that the Green's function can be considered as a wavefunction at $\mathbf{r}$ resulting from a unit excitation at $\mathbf{r}'$. But on the other hand, G can also be considered as the source for such an excitation. Both solutions satisfy Eq. (4.2), but they correspond to different boundary conditions: if H would be the Hamiltonian for a particle moving in a constant potential, then the first solution would correspond to an outgoing wave from the point $\mathbf{r}'$, while the second solution would be an incoming wave. In order to incorporate such boundary conditions into a unique definition for the Green's function, one adds an infinitesimal imaginary variable into the energy, which leads to the following definitions:

$$G^{\pm}(\mathbf{x},\mathbf{x}',E) \equiv \lim_{\eta\to 0^+} G(\mathbf{x},\mathbf{x}',E \pm \mathrm{i}\eta), \tag{4.4}$$

where the functions $G^{\pm}$ satisfy

$$\left[E \pm \mathrm{i}\eta - H(\mathbf{x})\right] G^{\pm}(\mathbf{x},\mathbf{x}',E) = \delta(\mathbf{x}-\mathbf{x}'). \tag{4.5}$$

The functions G^+ and G^- are called respectively the retarded and advanced Green's function. In the example given above, the retarded Green's function would correspond to the outgoing wave and the advanced Green's function to the incoming wave. More generally, when Fourier transforming the functions $G^{\pm}$ to the time domain using a closed contour integration in the complex plane, they would correspond to causal and anticausal solutions [47].

In the operator language, the retarded and advanced Green's function operators are defined uniquely for all real values of E by the relation

$$\widehat{G}^{\pm}(E) \equiv \lim_{\eta\to 0^+} \frac{1}{E \pm \mathrm{i}\eta - \widehat{H}}, \tag{4.6}$$

and they can thus essentially be calculated by inverting the Hamiltonian.

In the next sections, we will stop writing the hat in $\widehat{G}$ to denote an operator. It will be clear from the context whether G stands for a function (or a matrix in a discrete system) or an operator. We will also drop the subscript $\pm$ for distinguishing between the retarded or advanced Green's function: G will always stand for a retarded Green's function. From Eq. (4.6), it is clear that the advanced Green's function corresponds to the hermitian conjugate of the retarded one, i.e., $G^- = (G^+)^\dagger \equiv G^\dagger$.

4.2 Transmission coefficients and the Green's function

In the Landauer-Büttiker formalism presented in Chap. 2, a central device is connected to perfect leads, and its current-voltage characteristics can be expressed in terms of transmission coefficients between those leads. These transmission coefficients can be related to the Green's function of the central device, thereby justifying the effort we will make in the next sections to find this Green's function. We will suffice with merely stating this relation here, since it is standard nowadays, and since a thorough derivation would take us too far[1]. In a tight-binding representation of the system, the transmission coefficient between leads p and q is given by [2, 49]:

$$T_{pq} = \mathrm{Tr}\Big[\Gamma_p G_{pq} \Gamma_q G_{pq}^\dagger\Big]. \tag{4.7}$$

The Green's function G_{pq} in this expression is a submatrix of the Green's function G of the whole system: it contains only the elements of G between sites in the central device that connect to leads p and q: in particular, if $\mathcal{P}_{p(q)}$ is a projection operator onto the sites of the central device to which lead p (q) is connected, then

$$G_{pq} = \mathcal{P}_p \, G \, \mathcal{P}_q. \tag{4.8}$$

The matrix Γ_p in Eq. (4.7) is the so-called broadening function of lead p. It is given in terms of what is known as the self-energy Σ_p of the lead:

$$\Gamma_p = \mathrm{i}\big(\Sigma_p - \Sigma_p^\dagger\big). \tag{4.9}$$

This self-energy is related to elements of the Green's function between sites at the surface of the lead. The exact definition, and a more detailed discussion of these self-energies will be given in the next section [see Eq. (4.13].

4.3 Lattice Green's function method

One could have the impression that all has been said already about the Green's function technique: one just derives the tight-binding Hamiltonian of the system, writes it out in matrix form, and calculates the Green's function by inverting the matrix $E + \mathrm{i}\eta - H$. Physical quantities, like the transmission coefficients of the Landauer-Büttiker formalism, can then be calculated by expressing them in terms of this Green's function.

However, since we are concerned with an open system (there are semiinfinite leads connected to the sample), the tight-binding Hamiltonian matrix describing the complete system has infinite dimension and cannot be inverted numerically. Furthermore, even if one is able to truncate the Hamiltonian matrix, its direct inversion turns out to be numerically very expensive. These issues will be addressed in the current section. During the discussion, we will use quite often the notation $G_{nn'}$ to denote a submatrix of the total Green's function matrix G. $G_{nn'}$ "connects" sites of columns n and n', i.e.,

$$\langle\, m, \sigma | G_{nn'}(E) | m', \sigma' \,\rangle = G_{nm\sigma, n'm'\sigma'}(E) = \langle\, nm\sigma | G(E) | n'm'\sigma' \,\rangle, \tag{4.10}$$

where (m, n) label the sites in the tight-binding lattice, and σ, σ' are the spin indices.

---

[1] The interested reader can find such a derivation in Ref. [48].

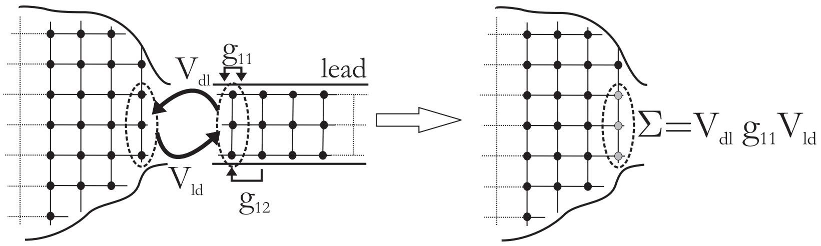

Figure 4.1: The influence of a lead can be described by adding its self-energy to the Hamiltonian of the device.

4.3.1 Semiinfinite leads: Self-energy description

Within the Landauer-Büttiker formalism, the system is composed of a central device connected to leads (see Fig. 2.1), and its Hamiltonian can therefore be subdivided as:

$$H = H_{cd} + \sum_i \left(H_l^i + V_{ld}^i + V_{dl}^i\right). \tag{4.11}$$

H_{cd} is the Hamiltonian for the central device, and H_l^i the Hamiltonian for lead i. The coupling between lead and device is described by V_{ld}^i (and its hermitian conjugate V_{dl}^i). A direct inversion $\left[E + \mathrm{i}\eta - H\right]^{-1}$ to obtain the Green's function is numerically impossible, since every H_l^i has infinite dimension.

The standard way to resolve this problem consists of describing the lead influence by a self-energy term: it can be shown (see, e.g., Refs. [2, 31]) that the central device, including the influence of the leads on it, is described by a *finite-dimensional* Hamiltonian

$$\mathcal{H}_{cd} = H_{cd} + \sum_i \Sigma^i, \tag{4.12}$$

where Σ^i is called the (retarded) self-energy[2] of lead i:

$$\Sigma^i = V_{dl}^i \, g_l^i \, V_{ld}^i. \tag{4.13}$$

The quantity g_l^i in this expression is the Green's function of the isolated semiinfinite lead: $g_l^i = [E + \mathrm{i}\eta - H_l^i]^{-1}$. At first sight it seems that the problem is just shifted, since now the calculation of g_l^i will involve the inversion of the infinite-dimensional Hamiltonian H_l^i. However, since a nearest-neighbor tight-binding model is used, the matrices V_{dl}^i and V_{ld}^i have nonzero elements only between sites on the surface of the lead and their neighboring sites in the device. This means that only the surface Green's function $(g_l^i)_{11}$ is needed in Eq. (4.13) (see also Fig. 4.1), and

---

[2] In many-body physics, self-energy terms are sometimes introduced to describe coupling of the system to phonons or to describe many-body interactions [47]. In these cases, the self-energies are usually only calculated up to some order in perturbation theory, so that the Hamiltonian one obtains is only an approximation. However, in our case the truncation of the device Hamiltonian by describing the influence of the leads by their self-energies is exact: no approximations whatsoever are made.

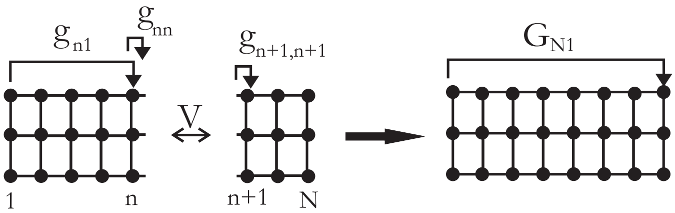

Figure 4.2: Attaching two isolated sections with Dyson's equation to obtain Green's functions for the connected system.

the point is that several methods are at our disposal for calculating this Green's function: in the absence of a magnetic field it is known analytically [2], while in the case of a magnetic field one can resort to several numerical methods (see, e.g., Refs. [50, 51]). The particular method we have used will be explained in Appendix B, in order not to drown the reader into a too dense technical discussion at this point.

Now, if the central device comprises C lattice sites, the Hamiltonian $\mathcal{H}_{cd}$ in Eq. (4.12) can be represented by a $2C \times 2C$ matrix (the factor 2 arises from spin) and the corresponding Green's function can in principle be obtained from

$$G_{cd} = \left[E + \mathrm{i}\eta - \mathcal{H}_{cd}\right]^{-1}. \tag{4.14}$$

Nevertheless, the number of floating point operations necessary to invert a $2C \times 2C$ matrix scales as $(2C)^3$, and therefore the inversion in Eq. (4.14) puts heavy constraints on the numerically reachable system size. Fortunately, more efficient recursive methods exist for obtaining G_{cd}, and these will form the subject of the next sections.

4.3.2 Recursive technique: Standard method

Recursive methods for the evaluation of Green's functions are based upon the division of the device in smaller sections of which the Green's functions can be calculated easily. These sections are then "glued together" by using the so-called Dyson's equation [47],

$$G = g + g\,V\,G, \tag{4.15}$$

which allows to relate the Green's function g of two disconnected subsystems to the Green's function G of the connected system, where V describes the hopping between the subsystems.

Before embarking upon a detailed discussion of the recursive Green's function technique, we will illustrate the use of Dyson's equation with an example, depicted in Fig. 4.2. Consider a system consisting of two parts, and suppose that we have access to the Green's function g describing the *isolated* parts. Now we would like to obtain G_{N1}, i.e., elements of the Green's function between the first and last column of the *coupled* device. This can be done by projecting Eq. (4.15) between columns N and 1:

$$\begin{aligned} G_{N1} &= \langle\, N|G|1\,\rangle && (4.16a)\\ &= \langle\, N|g|1\,\rangle + \sum_{|\alpha\,\rangle,|\beta\,\rangle} \langle\, N|g|\alpha\,\rangle\langle\,\alpha|V|\beta\,\rangle\langle\,\beta|G|1\,\rangle && (4.16b)\\ &= \langle\, N|g|n\,\rangle\,\langle\, n|V|n+1\,\rangle\,\langle\, n+1|G|1\,\rangle && (4.16c)\\ &= g_{Nn}\,V_{n,n+1}\,G_{n+1,1}. && (4.16d) \end{aligned}$$

Equation (4.16c) is obtained by noting that the hopping matrix V between the disconnected systems has only nonzero elements between columns n and $n+1$ in our nearest neighbor tight-binding model. Furthermore, we have $g_{N1} = 0$ since g is for the disconnected system only. We can proceed now to find the unknown $G_{n+1,1}$ in Eq. (4.16d) by taking again the appropriate matrix elements of Dyson's equation. This procedure can be continued until we have found a closed set of equations. We immediately write down the resulting equations:

$$\begin{aligned} G_{n+1,1} &= g_{n+1,n+1}\,V_{n+1,n}\,G_{n1}, \quad \text{with} && (4.17a)\\ G_{n1} &= g_{n1} + g_{nn}\,V_{n,n+1}\,G_{n+1,1}. && (4.17b) \end{aligned}$$

From these equations, we obtain:

$$G_{n+1,1} = \Big[1 - g_{n+1,n+1}\,V_{n+1,n}\,g_{nn}\,V_{n,n+1}\Big]^{-1} g_{n+1,n+1}\,V_{n+1,n}\,g_{n1}. \qquad (4.18)$$

Substituting this in Eq. (4.16d), we will get an expression for G_{N1} in terms of Green's functions for the isolated sections, which was our initial goal.

We now have enough technical luggage to proceed to the recursive Green's function technique [31, 52]. In the following, we will consider a central device discretized on a rectangular tight-binding lattice consisting of M rows and N columns (Fig. 4.3). The influence of the leads that are attached to this central device will be described by their self-energy, giving rise to a finite-dimensional Hamiltonian $\mathcal{H}_{cd}$ for the device, as discussed in the preceding section. It will be assumed that all leads are attached at the left and right edges of the central device so that their self-energies only influence sites of the first and last column of the device (depicted gray in the figures). If this would not be the case, self-energy terms could introduce an effective hopping between lattice columns that are not nearest neighbors, and in this case the recursive technique cannot be applied: in the example above, V would have nonzero contributions between columns different from n and $n+1$, leading to much more complicated expressions in Eq. (4.16c).

A wide range of physical quantities of such a system can be written in terms of the small subset of Green's function matrices that is depicted in Fig. 4.3: it concerns elements of the Green's function between the first/last column of the device and any intermediate column. The first step towards calculating these consists of separating

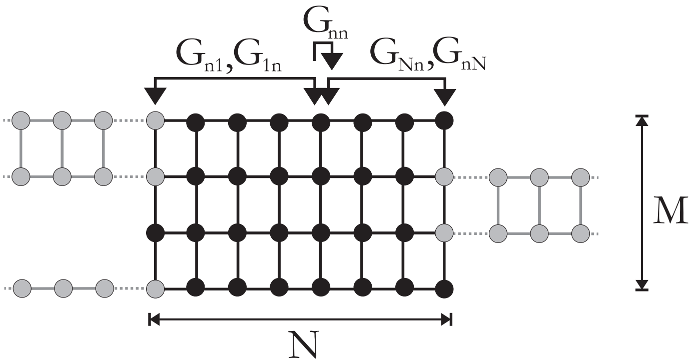

Figure 4.3: Subset of device Green's functions needed for calculating the physical quantities of interest. Leads attached to the central device are depicted in gray.

the device in isolated columns, and calculating the Green's function G_{ii}^{isol} for every isolated column $i = 1, 2, ..., N$ by doing a direct inversion:

$$G_{ii}^{\text{isol}} = \Big[E + \mathrm{i}\eta - \langle\, i|\mathcal{H}_{cd}|i\,\rangle\Big]^{-1}, \tag{4.19}$$

where $\langle\, i|\mathcal{H}_{cd}|i\,\rangle$ is the tight-binding Hamiltonian of column i. This step is depicted in Fig. 4.4(a).

The next step consists of assembling the complete device by gluing together the columns one by one, as shown in Fig. 4.4(b). Suppose we already have the Green's functions G_{n1}^L, G_{1n}^L, G_{nn}^L of a strip of n columns connected together. The superscript L is added to denote the fact that they only represent a part of the device (namely a strip of n columns), not the whole device. The Green's functions $G_{n+1,1}^L, G_{1,n+1}^L$, and $G_{n+1,n+1}^L$ for a section of $n+1$ columns can then be derived by projecting Dyson's equation [Eq. (4.15)] between the appropriate columns, in a similar way to what has been done in the simple example discussed above. We will only state the end result here:

$$\begin{aligned}
G_{n+1,n+1}^L &= \Big[1 - G_{n+1,n+1}^{\text{isol}}\, V_{n+1,n}\, G_{n,n}^L\, V_{n,n+1}\Big]^{-1} G_{n+1,n+1}^{\text{isol}}, && \text{(4.20a)}\\
G_{n+1,1}^L &= G_{n+1,n+1}^L\, V_{n+1,n}\, G_{n,1}^L, && \text{(4.20b)}\\
G_{1,n+1}^L &= G_{1n}^L\, V_{n,n+1}\, G_{n+1,n+1}^L. && \text{(4.20c)}
\end{aligned}$$

Starting from the leftmost column $n = 1$ with $G_{1,1}^L = G_{1,1}^{\text{isol}}$, one can proceed in this way through the whole sample and calculate the G_{n1}^L, G_{1n}^L and G_{nn}^L for all n. After connecting the last column, one obtains the Green's function submatrices $G_{N1}^L = G_{N1}$ and $G_{1N}^L = G_{1N}$ connecting the first and last column of the complete device. These steps complete the *standard* recursive Green's function method [31, 52], and they suffice for describing transport quantities within the Landauer-Büttiker formalism. Indeed, all leads are connected to the left or right edge of the system,

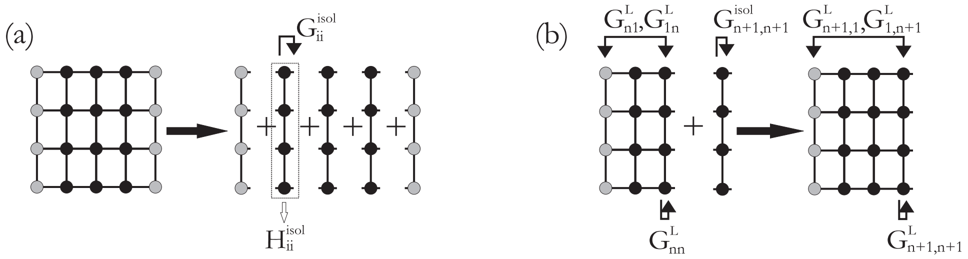
(a)
$G^{\rm isol}_{\rm ii}$
$H^{\rm isol}_{\rm ii}$
(b)
$G^{\rm L}_{\rm n1}, G^{\rm L}_{\rm 1n}$
$G^{\rm isol}_{\rm n+1,n+1}$
$G^{\rm L}_{\rm n+1,1}, G^{\rm L}_{\rm 1,n+1}$
$G^{\rm L}_{\rm nn}$
$G^{\rm L}_{\rm n+1,n+1}$

Figure 4.4: Standard recursive technique. The device is divided into its separate columns (a), and Dyson's equation is used to glue them together and to find the relevant Green's functions (b).

and the relation in Eq. (4.7) thus expresses the transmission coefficients in terms of the Green's functions G_{N1} or G_{1N}.

Looking back at the Eqs. (4.19)-(4.20), one can see that the computational operations necessary for obtaining the final Green's functions are either products or inversions of $2M \times 2M$ matrices, and the total amount of such operations is proportional the length N of our system. Since the computational effort for a matrix product or inversion scales as $(2M)^3$ in the number of floating point operations, the total numerical effort for the recursive technique scales as M^3N for large systems ($N \gg 1$). In this way, we gain a factor of N^2 in efficiency compared to the direct inversion of the complete $(2MN) \times (2MN)$ matrix $E + \mathrm{i}\eta - \mathcal{H}_{cd}$, which scaled as M^3N^3. The price one has to pay for the increased efficiency is that one can only calculate a smaller subset of Green's functions (direct inversion would give us $G_{nn'}$ for all n, n').

4.3.3 Recursive technique: An extension

We have extended the standard recursive technique in order to obtain the additional Green's functions G_{Nn}, G_{nN}, G_{n1}, G_{1n} and G_{nn} depicted in Fig. 4.3. Having such functions available will prove to be convenient in the next chapters.

We proceed as follows. After having completed the standard technique, we start over from the Green's functions of the isolated columns, and glue them together as we did previously on the basis of Dyson's equation, but now beginning from the right column. This is depicted in Fig. 4.5(a). The Green's functions we calculate with every step are G^R_{Nn}, G^R_{nn} and G^R_{nN}. They can be given in terms of the $G^R_{N,n+1}$, $G^R_{n+1,n+1}$ and $G^R_{n+1,N}$ as:

$$
\begin{aligned}
G^R_{nn} &= \left[1 - G^{\rm isol}_{nn}\, V_{n,n+1}\, G^R_{n+1,n+1}\, V_{n+1,n}\right]^{-1} G^{\rm isol}_{nn}, && (4.21a)\\
G^R_{Nn} &= G^R_{N,n+1}\, V_{n+1,n}\, G^R_{n,n}, && (4.21b)\\
G^R_{nN} &= G^R_{nn}\, V_{n,n+1}\, G^R_{n+1,N}. && (4.21c)
\end{aligned}
$$

Starting from $G^R_{NN} = G^{\rm isol}_{NN}$, one can obtain G^R_{Nn}, G^R_{nN} and G^R_{nn} for all $n =$

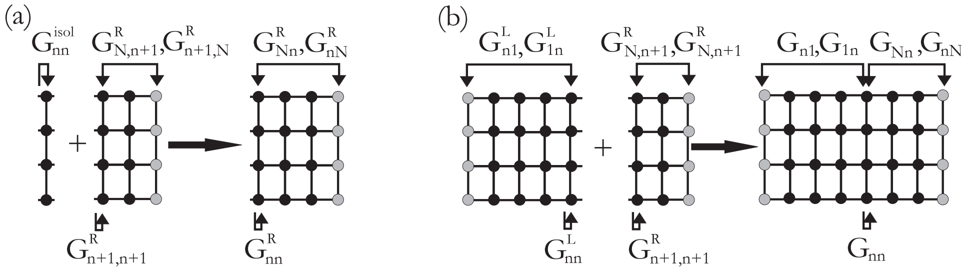

Figure 4.5: Extension of the standard recursive technique. The isolated columns are glued together, but now starting from the righthand side (a). The final step consists of adding these strips of columns to the ones calculated in Fig. 4.4 (b).

$N-1, N-2, ..., 1$. Again, the superscript R has been added to denote that these are Green's functions for a subsection of the complete device.

The final step consists of attaching the previously calculated Green's functions G^L and G^R in pairs, as illustrated in Fig. 4.5(b). One attaches a strip of connected columns 1 to n (with known Green's functions G^L_{n1} and G^L_{nn}) to the strip of columns $n+1$ to N (with Green's functions $G^R_{N,n+1}$ and $G^R_{n+1,n+1}$), and this is done for all $n = 1, ..., N$. Again, projection of Dyson's equation leads to the relevant mathematical expressions:

$$G_{n1} = \left[1 - G^L_{nn}\, V_{n,n+1}\, G^R_{n+1,n+1}\, V_{n+1,n}\right]^{-1} G^L_{n1}, \tag{4.22a}$$

$$G_{1n} = G^L_{1n} + G^L_{1n}\, V_{n,n+1}\, G^R_{n+1,n+1}\, V_{n+1,n}\, G_{nn}, \tag{4.22b}$$

$$G_{nn} = \left[1 - G^L_{nn}\, V_{n,n+1}\, G^R_{n+1,n+1}\, V_{n+1,n}\right]^{-1} G^L_{nn}, \tag{4.22c}$$

$$G_{Nn} = G^R_{N,n+1}\, V_{n+1,n}\, G_{n,n}, \tag{4.22d}$$

$$G_{nN} = G_{nn}\, V_{n,n+1}\, G^R_{n+1,N}, \tag{4.22e}$$

Both these additional steps consist of doing a number of matrix multiplications and inversions that scales linear in N. The numerical computation of the extra Green's functions with our extended recursive method thus has the same efficiency as the standard technique.

Having access to these extra Green's functions will prove to be very convenient in the following chapters: it will allow us to obtain quantities like the current density distribution, and furthermore, certain calculations can be done with greater efficiency than with the standard Green's functions G_{N1} and G_{1N} alone.

Part II

Results

Chapter 5

Imaging coherent electron flow through a quantum point contact

5.1 Introduction

Most people studying electronic transport in mesoscopic systems have been concentrating on global transport properties that can be obtained by passing a current through the sample and measuring the voltage drop between the leads connected to it. Proceeding this way, the mesoscopic systems already had a few surprising phenomena in store: think, e.g., about the universal conductance fluctuations [6], or the quantized conductance in quantum point contacts [4, 5].

Although most of these transport phenomena are well understood nowadays, even without explicitly referring to (current) density distributions in the device, it can be interesting to obtain more local information on the flow of electrons through the system. For example, electron states localized at the edges of the sample play a prominent role in the explanation of the quantum Hall effect. Nevertheless, such local properties of the system remained experimentally unreachable for quite a long time. Only recently have experimentalists succeeded in probing the electron flow in a two-dimensional electron gas (2DEG) locally with a scanning probe microscope [14, 15]. In these experiments, the scanning probe tip functions as a local scatterer for electrons and a spatial map of electron flow is obtained by measuring the conductance decrease of the sample as a function of the tip position.

This technique was originally applied for studying electron flow through a narrow constriction (point contact) in a high-mobility 2DEG at the interface of a semiconductor heterostructure, and some interesting (coherence) effects were observed [14, 15, 53]. From a theoretical point of view, most of the observed effects were interpreted using either electron density or semiclassical current density calculations. However, the relation between these quantities and the measured observable, i.e., a conductance decrease, is not clear a priori. Therefore, a direct numerical simulation of the experiment can be very interesting and will be the main topic of the current chapter. It will result in a deeper understanding of the observed effects, and at the same time it will also allow for a convenient way of predicting new effects, and for giving clear guidelines in studying them experimentally.

Some progress in simulating the scanning probe experiments was already made in Refs. [54, 55], but the use of rather inefficient numerical techniques puts rather stringent limits on the practical applicability to larger systems. In this chapter we will show that, making full use of our extended recursive technique, we are able not only to simulate the experimental results in a very efficient way, but on top of that a fully quantum mechanical current density distribution in the sample can be obtained simultaneously without much extra effort. Doing so, we are able to reproduce numerically all features of electron flow through a quantum point contact that were observed experimentally. Furthermore, a one-to-one comparison with the calculated current density will make it clear that the scanning probe technique really visualizes current flow through the sample.

Numerical simulations in a high magnetic field will reveal the inadequateness of the original scanning probe method in visualizing electron flow in this regime. In order to be able to obtain an image of electron flow in a magnetic field, a measurement technique will be proposed in which the probe tip is used to locally measure the chemical potential. This imaging method can give relevant information about the current flow through a two-dimensional sample, both in the presence and absence of a magnetic field.

The chapter will be subdivided as follows. In the next section, the experimental setup and measuring procedure is described in full detail. After this, we discuss the different imaging quantities that we can obtain numerically, and show how they can be calculated efficiently within our numerical framework. Subsequently a small discussion will follow on the experimental parameters of the 2DEG, and on how they translate into tight-binding parameters for our model. The main results of the chapter are found in Sec. 5.5, where visualizations of electron flow through a quantum point contact are presented.

5.2 Experiment

5.2.1 Setup and measurement procedure

The experimental setup used in Refs. [14, 15] is depicted in Fig. 5.1(a). A two-dimensional electron gas (2DEG), formed at the interface of a GaAs/AlGaAs heterostructure, is electrically connected to two Ohmic contacts which can be used to pas a current through the electron gas. Two metallic split gates are attached on top of the structure. Applying a negative voltage on these gates results in a depletion of the electron gas underneath them, due to Coulomb repulsion. As such, a narrow constriction (quantum point contact) can be formed in the 2DEG for the electrons to flow through, and the width of this constriction can be tuned by varying the voltage on the split gates.

Now suppose the tip of a scanning tunneling microscope (STM) is put at a certain position above the electron gas. The electrostatic potential resulting from a

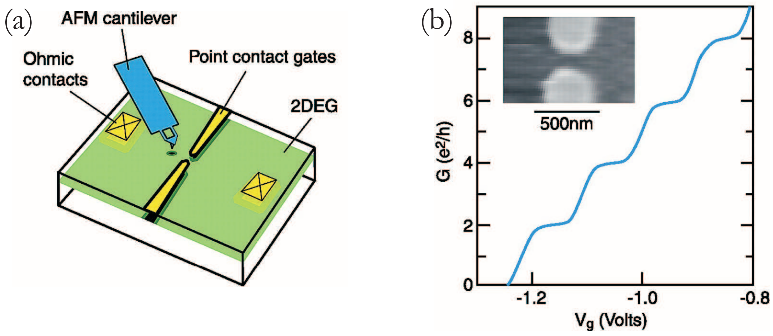

Figure 5.1: Measurement setup for imaging electron flow through a quantum point contact (a). The conductance of a point contact quantized (b). Image from Ref. [14].

negative voltage on the tip can deplete a small spot of the 2DEG at the tip position, which can act as a local scatterer for electrons. As a result, the conductance of the sample will decrease compared to the situation with no tip present. This conductance decrease will be large when the tip is positioned over a region where a lot of electrons are flowing since then a lot of electrons can be backscattered, while it will be small if there are less electrons flowing underneath the tip. As such, by moving the tip across the whole sample and by measuring the conductance decrease for every single tip position, one can obtain an image of where electrons are flowing through the sample.

It is obvious that this imaging method is sufficiently general so that it can be used for a wide range of two-dimensional geometries. Nevertheless, at the moment of this writing, it has only been applied to the quantum point contact (QPC) geometry [14, 15, 53]: the experimental results for this system will be presented in the next section.

5.2.2 Experimental results

When measuring the conductance of the quantum point contact (in the absence of the STM tip), it is found to be quantized in steps of $2e^2/h$ as a function of the voltage on the split gates, as depicted in Fig. 5.1(b). Conductance quantization in point contacts is not new: it was already observed almost two decades ago [4, 5] and can be fully understood within the Landauer-Büttiker formalism, as will be explained next.

The conductance of the sample can be expressed in terms of the transmission coefficient T between the sample edges (see Chap. 2):

$$G = \frac{2e^2}{h} T = \frac{2e^2}{h} \sum_n T_n. \tag{5.1}$$

The point contact creates a quasi-1D channel in the 2DEG, so that different discrete transverse modes n with energies E_n can be defined. In Eq. (5.1), T has been subdivided in transmission probabilities T_n for these individual modes. When the motion of the electrons is ballistic (i.e., there is no impurity scattering) and the width of the constriction varies smoothly along the propagating direction, there will be no scattering between different modes and the coefficients T_n can take only values of either 0 or 1 [56, 57]: $T_n = 1$ if the Fermi energy $E_F > E_n$, and zero otherwise[1]. In this case, the conductance of the point contact is thus proportional to the number of modes transmitting through it. A larger number of modes can transmit when the QPC is made wider (since all E_n will shift to lower values), which is done by adjusting the voltage on the split gates to less negative values. Every additional transmitting mode increases the conductance by $2e^2/h$ according to Eq. (5.1) and gives rise to a discrete step in the conductance. Such steps are clearly visible in Fig. 5.1(b), although they are not as sharp as expected from the theory above. This is because the motion of the electrons is never fully ballistic in an experimental situation and because the width of a quantum point contact cannot change in a perfectly adiabatic manner.

Electron flow images in a QPC obtained with the scanning probe technique described in the preceding section are shown in Fig. 5.2. In the first picture, the voltage on the split gates is tuned so that the conductance of the point contact lies on the first plateau ($G = 2e^2/h$). In this case the region of large conductance decrease, and thus large electron flow, is concentrated in one lobe, corresponding to electrons in the first mode of the QPC flowing through the constriction. With two channels transmitting through the QPC [Fig. 5.2(b)], one can see two lobes of electron flow. In general, mode n will contribute n lobes to the spatial pattern of electron flow. As such, electron flow shows a modal pattern reflecting the different channels transmitting through the QPC.

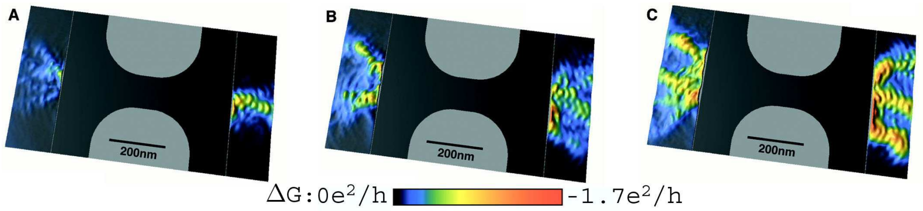

Figure 5.2: Electron flow maps obtained with the scanning probe technique. The amount of channels transmitting through the QPC can be varied by changing the split gate voltage. Results are shown for a single channel (a), two channels (b), and three channels (c) open for transmission. The QPC contour is depicted in gray. The black strip on both sides of the QPC corresponds to a region where no data is available: placing the tip in such a region would pinch off the QPC, making a conductance measurement useless. Image from Ref. [53].

---

[1] The quantum mechanical possibility of tunneling will be neglected here.

Another striking feature of the flow maps are fringes spaced at half the Fermi wavelength. These are an interference effect resulting from back-and-forth scattering between the scanning probe tip and the quantum point contact. As such, they are remnants of the experimental technique, but nevertheless they are interesting features to study: for instance, the fringe spacing is directly related to the Fermi wavelength and thus to the electron density, so that spatial variations of this spacing can be used to measure the local electron density [58].

At larger distances from the point contact, the flow maps show a quite surprising branching behavior, as shown in Fig. 5.3. The branches in this picture are not just continuations of the different lobes seen in Fig. 5.2. For example, in Fig. 5.3 there are multiple branches although it is taken on the first conductance plateau of the QPC with only a single channel open [and thus a single lobe in Fig. 5.2(a)]. Furthermore, existent branches fork into new branches in an irregular way so that the number of branches increases as one moves further from the point contact [59]. The source of this branching behavior is disorder in the system: the Coulomb po-

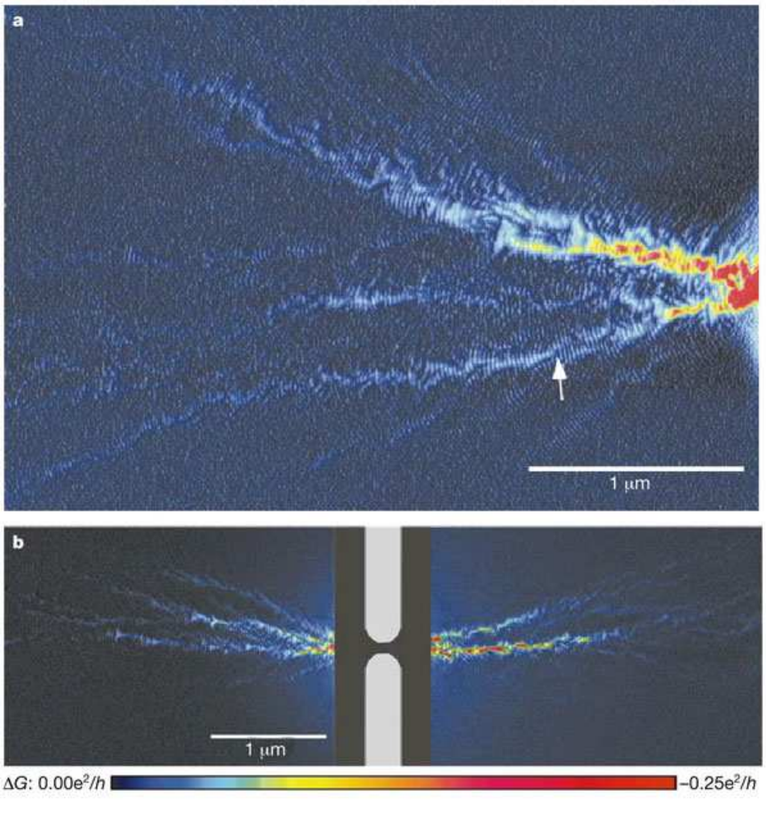

Figure 5.3: Scanning probe map showing branching electron flow at larger distances from the QPC. Interference fringes are present throughout the sample. Only the part on the left of the QPC is shown in (a), while in (b), the branching behavior is shown on both sides of a *different* QPC. Picture from Ref. [15].

tential of the donor atoms used to inject carriers in the 2DEG creates a potential landscape that consists of small dips and bumps. The branches are not resulting from electrons flowing in the valleys of this impurity potential, since the Fermi energy of the electrons in the experiment was large compared to the height of these structures. Rather it was proven that they result from multiple small-angle scattering events off the bumps and dips in the potential [59–61]. Every bump or dip can be understood to act as a small lens for the electron flow, and a large number of such lenses can then contribute to the "collimation" of electron flow in branches. Please note also that all branches remain decorated with the interference fringes spaced at half the Fermi wavelength.

5.3 Numerical simulation: Imaging modes

From Figs. 5.2 and 5.3, it is clear that the scanning probe technique can offer nice visualizations of electrons flowing through the sample. A numerical simulation of such experiments can therefore be interesting since on one hand it can aid in a better understanding of the physics behind the experimental results, for example by comparing the measured quantity (a conductance decrease) with different physical observables (e.g., the current density). On the other hand, a range of new systems can be simulated which can result in proposals for new effects to be measured experimentally. In the next sections, a detailed account will be given on the simulation possibilities that are available within the numerical framework we have presented in the previous three chapters.

5.3.1 Scanning probe used as a local scatterer

Let's first look at how we can simulate the scanning probe experiment. In our numerical calculations, we will consider a device that is discretized onto a rectangular tight-binding lattice of N columns and M rows, as in Fig. 5.4. Two leads (depicted gray in the figure) are attached to the device at the left and right side. These leads have a width of M rows, spanning the whole width of the sample edges. Only spin-independent processes will be taken into account, so Green's functions between columns (like G_{N1}) can be represented by $M \times M$ matrices.

For numerical convenience, the electrostatic influence of the scanning probe tip on this device will be modeled by a delta-function potential V^{tip} at the lattice site over which the tip is positioned. An image of electron flow is then obtained by evaluating the conductance decrease of the sample for all possible lattice positions of the tip. We will refer to this imaging method as the local scatterer method, for obvious reasons.

Using the Landauer-Büttiker formalism, the conductance decrease of the device under influence of the tip can be written as

$$\Delta G(n,m) = \frac{2e^2}{h}\big[T_0 - T(n,m)\big], \tag{5.2}$$

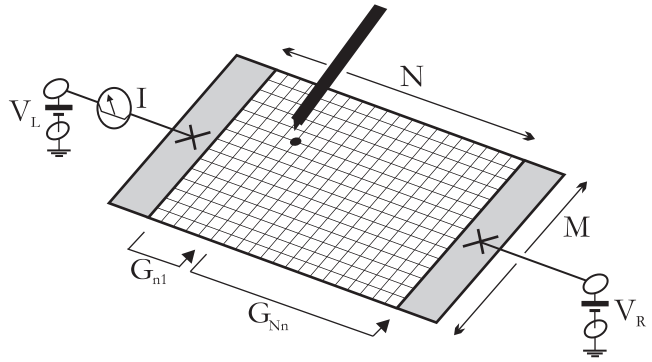

Figure 5.4: Tight-binding setup for the local scatterer measurement technique. The on-site energy of the lattice site under the scanning probe tip is increased, resulting in a local scattering potential. The conductance of the sample is obtained by calculating the current I through the leads when a bias voltage $V_R - V_L$ is applied.

where T_0 is the transmission coefficient between the leads in the absence of the tip, and $T(n,m)$ is the same quantity with the tip positioned over site (n,m). The transmission coefficients can be expressed in terms of Green's functions (see Sec. 4.2):

$$T(n,m) = \mathrm{Tr}\left[\Gamma_R\, G_{N1}\, \Gamma_L\, G_{N1}^{\dagger}\right], \tag{5.3}$$

where $\Gamma_L(R)$ is the broadening function of the left (right) lead [Eq. (4.9)].

For calculating the Green's function G_{N1} between the leads one could in principle proceed as follows. For a certain tip position, one first adds the repulsive potential V^{tip} to the Hamiltonian of the system and consequently uses the standard recursive Green's function method (Sec. 4.3.2) for calculating G_{N1} for this particular tip location. This would mean that the recursive technique has to be started over and over again for every single tip position. The numerical effort for such a procedure is quite big: a single recursive step takes a numerical effort scaling as M^3N (see Sec. 4.3.2), so the complete flow map containing MN sites requires an effort of M^4N^2. Nevertheless, this technique has been used in Ref. [54] to study the modal pattern of electron flow close to the point contact, but the low efficiency puts severe constraints on the possible lattice size and therefore the results were not completely satisfactory.

We have found a more efficient way of arranging things. First, all the Green's functions depicted in Fig. 4.3 of Chap. 4 are calculated for the system *without* the scanning probe tip. These will be depicted with a superscript 0 from now on. Next, for every single tip position (n,m), the Green's function G_{N1}, taking into account the tip influence, can be calculated by projecting Dyson's equation,

$$G = G^0 + G^0\, V^{\mathrm{tip}}\, G, \tag{5.4}$$

between columns N and 1. This leads to

$$G_{N1} = G_{N1}^0 + G_{Nn}^0\, V_{nn}^{\mathrm{tip}}\, (1 - G_{nn}^0\, V_{nn}^{\mathrm{tip}})^{-1}\, G_{n1}^0, \tag{5.5}$$

giving G_{N1} in terms of Green's functions for the system without the tip. The point now is that the calculation of the necessary Green's functions G^0 without the tip only takes an effort scaling as M^3N with the extended recursive technique presented in Chap. 4. Furthermore, the evaluation of the conductance decrease in Eq. (5.2) for all possible tip locations also requires an effort scaling only as M^3N when using Eqs. (5.5) and (5.3), as will be commented further upon in Appendix E. As such, one gains a factor of MN in efficiency compared to the standard method used in Ref. [54], allowing for larger systems to be studied.

One final note can be made concerning the symmetry of the obtained electron flow map in the presence of a magnetic field. Since the flow map is essentially obtained by making two-terminal measurements of current and voltage, it will be symmetric with respect to reversal of the magnetic field direction (see Fig. 2.2 and the discussion underneath it in Chap. 2).

5.3.2 Scanning probe used as a local voltage probe

The experimental results discussed in Sec. 5.2 already have proven that the local scatterer method can give very interesting visualizations of electron flow through a two-dimensional sample. Unfortunately, this imaging technique will not always yield the expected results when magnetic fields are present, as will be explained now.

Electrons in a magnetic field describe cyclotron orbits. Upon introducing boundaries to the sample, these orbits will lead to a cycloidal motion of the electrons along the edges of the sample as depicted in Fig. 5.5, at least if the magnetic field is strong enough. Electrons traveling in opposite directions will be located on opposite sample edges, so the overlap of their wavefunctions will be small and electron backscattering will be suppressed as a consequence. Since backscattering by the scanning probe tip (and the resultant conductance decrease) was the main working principle behind the local scatterer method, it can therefore not give the desired results in a high field regime.

However, it is clear from this picture of edge state transport (Fig. 5.5), that every single electron emanating from the left lead enters the edge states carrying

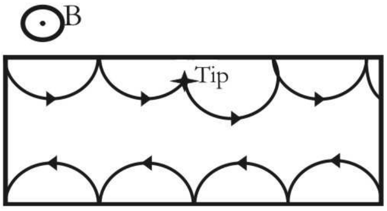

Figure 5.5: Cycloidal motion of electrons along the edges of a 2D sample in a strong magnetic field. Electrons cannot be backscattered by a scanning probe tip because paths with opposite propagation direction are well separated.

current to the right and ends up in the right contact, while all electrons coming out of the right contact enter the edge states on the opposite side of the sample and empty in the left contact, precisely because there is no possibility for backscattering. Therefore, edge states carrying current to the right (left) are in equilibrium with the left (right) contact and one should clearly see different chemical potentials at opposite edges. As such, a picture of edge-state transport in a magnetic field could be obtained when one is able to locally measure the chemical potential in the sample.

Measuring the local chemical potential can be done using a scanning probe tip as a voltage probe: in this case, tunneling of electrons between sample and tip is made possible, and a voltage meter is connected to the tip, as in Fig. 5.6. Since this voltage meter ideally draws no current, every electron tunneling into the tip has to come out at a later instant and the voltage on the tip will therefore equilibrate itself to the local chemical potential in the sample.

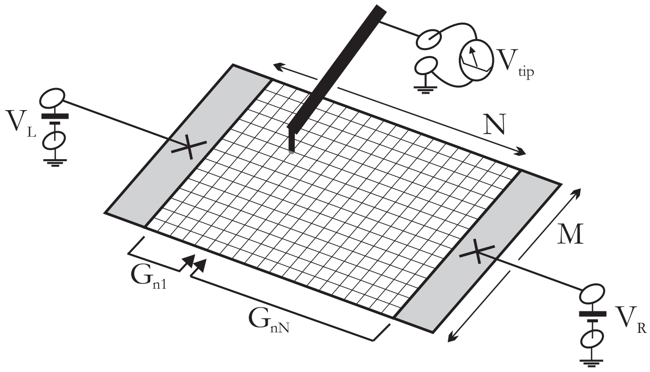

Figure 5.6: Tight-binding setup for the voltage probe measurement technique. The voltage on the scanning probe tip V_{tip} is measured as a function of its position when tunneling between the tip and the lattice site underneath is allowed.

The principle behind this technique is not new as it has already been used experimentally to probe the potential distribution at metal-insulator-metal interfaces [62] or at grain boundaries [63]. Nevertheless, this technique has not yet been applied experimentally to the study of mesoscopic systems, although some theoretical considerations have been put forward in Refs. [64, 65]. Our numerical simulations will prove it to be an interesting imaging technique even in the mesoscopic regime.

Within our numerical framework, the scanning probe tip in the voltage probe configuration will be modeled by an extra one-dimensional semiinfite lead attached to a site of our tight-binding model of our sample. This lead can be thought to extend in a direction perpendicular to the sample. Now one has three leads: the left and right lead through which a current is passed, and the STM tip that measures a voltage. For such a multi-lead structure, the currents and voltages through the leads are given within the Landauer-Büttiker formalism (see Chap. 2):

$$I_p = \frac{2e^2}{h} \sum_q T_{pq} \big(V_p - V_q\big), \tag{5.6}$$

where p and q label the leads, and T_{pq} are transmission coefficients between the leads. Using current conservation, combined with the fact that the STM tip draws no current, one can solve Eq. (5.6) for the voltage measured on the STM tip:

$$V_{\text{tip}} - V_L = \frac{T_{\text{tip},L}}{T_{\text{tip},L} + T_{\text{tip},R}} \big(V_R - V_L\big). \tag{5.7}$$

Our numerical method thus should be able to calculate the transmission coefficients $T_{\text{tip},L(R)}$ from the left and right contact to the STM tip, and this as a function of the tip position. These coefficients can be expressed as (with the tip at site (n, m)):

$$\begin{aligned} T_{\text{tip},L} &= \text{Tr}\,\big[\Gamma_{\text{tip}}\, G_{n1}\, \Gamma_L\, G^\dagger_{n1}\big], && (5.8\text{a}) \\ T_{\text{tip},R} &= \text{Tr}\,\big[\Gamma_{\text{tip}}\, G_{nN}\, \Gamma_R\, G^\dagger_{nN}\big]. && (5.8\text{b}) \end{aligned}$$

Γ_{tip} is related to the self-energy of the tip as $\Gamma_{\text{tip}} = \mathrm{i}\,(\Sigma_{\text{tip}} - \Sigma^\dagger_{\text{tip}})$. For a one-dimensional lead, this self energy Σ_{tip} is known analytically [2]:

$$\langle\, nm|\Sigma_{\text{tip}}|nm\,\rangle = -t\, e^{\mathrm{i}\arccos\left[1 - E_F/(2t)\right]}, \tag{5.9}$$

where t is the hopping parameter of the tight-binding model, and E_F the Fermi energy of the electrons.

To obtain the most efficient numerical procedure for evaluating the Eqs. (5.8), we calculate first the Green's functions without the influence of the tip (again denoted by a superscript 0 in the following), and only then calculate the Green's functions G_{n1} and G_{nN} that include the tip influence by using Dyson's equation [Eq. (5.4)]. The potential V in Dyson's equation now corresponds to the self-energy of the tip: $V = V^{\text{tip}} = \Sigma_{\text{tip}}\,|nm\,\rangle\langle\, nm|$. Projection of Dyson's equation between the relevant columns eventually gives

$$\begin{aligned} G_{n1} &= (1 - G^0_{nn}\, V^{\text{tip}}_{nn})^{-1}\, G^0_{n1}, && (5.10\text{a}) \\ G_{nN} &= (1 - G^0_{nn}\, V^{\text{tip}}_{nn})^{-1}\, G^0_{nN}. && (5.10\text{b}) \end{aligned}$$

The matrix inversion in this expression will boil down to the inversion of a scalar, because V^{tip}_{nn} has only one nonzero element (due to the one-dimensional model of the tip). Furthermore, calculation of the traces in Eqs. (5.8) is also not computationally expensive since Γ_{tip} has also only a single nonzero element. Therefore, the major computational effort for obtaining the chemical potential map comes from the calculation of the Green's functions without the influence of the tip. Scaling as M^3N, the computational procedure is thus as efficient as for the local scatterer method.

Since this imaging mode corresponds to making a three-terminal measurement, the map of the local chemical potential will not be invariant under magnetic field reversal. It is therefore clear that this imaging technique should contribute differently to our understanding of electron flow, compared to the local scatterer method.

5.3.3 Current density in the absence of a tip

Intuitively one expects the local scatterer measurement method to give information about the current density in the sample. From a strictly theoretical point of view however, the correspondence between the measured quantity, i.e., a conductance decrease, and the current density is not a priori clear. Therefore, it would be useful to compare the numerical flow map obtained with the local scatterer technique with a calculation of the current density in one and the same sample, and to see if and how they correspond.

Within our numerical framework, we are indeed able to calculate the current density in the sample, based on expressions that were first presented by Cresti *et al.* in Refs. [66, 67]. These expressions can be written in terms of the Green's functions that are available with our extended recursive technique. The results will be shortly stated here, while a full derivation can be found in Appendix C.

Equilibrium Current

Without an applied bias, no net current is flowing through the leads. This does not mean however that the current density distribution is necessarily zero: persistent currents can be flowing through the device when a magnetic field is present. In recent papers, an expression for this equilibrium current was derived [66, 67]. Adapted to our notation, the expression for the charge current flowing from one node to a neighboring node reads (m labels the rows of the lattice, n the columns):

$$I_{(n-1,m)\to(n,m)} = \frac{2e}{\hbar}\int\frac{\mathrm{d}E}{2\pi}\, f(E)\, A \tag{5.11a}$$

$$I_{(n,m)\to(n,m+1)} = \frac{2e}{\hbar}\int\frac{\mathrm{d}E}{2\pi}\, f(E)\, C. \tag{5.11b}$$

with the matrix elements

$$A = 2\,\mathrm{Re}\left\langle m\middle|\, G_{nn}\,\Sigma_n^l - \Sigma_n^l\, G_{nn}\,\middle| m\right\rangle, \tag{5.12a}$$

$$C = 2\,\mathrm{Re}\left\langle m+1\middle|\, (t^y_{m,n})^*\,(G_{nn} - G^\dagger_{nn})\,\middle| m\right\rangle. \tag{5.12b}$$

Here, $f(E)$ is the Fermi-Dirac distribution function of the sample, and $-e$ is the electronic charge. We have also introduced:

$$\Sigma_n^l = V_{n,n-1}\, G^L_{n-1,n-1}\, V_{n-1,n}, \tag{5.13}$$

where the matrices $G^L_{n-1,n-1}$ were defined in Fig. 4.4(b) of Chap. 4. All Green's functions in these expressions can be calculated with our extended recursive technique.

The physical validity of these equations can be checked as follows. When summing the longitudinal vertex currents over the row indices m, the total current through a single column is found to be zero: $\sum_m I_{(n-1,m)\to(n,m)} = 0$ (because

$\mathrm{Tr}\big[G_{nn}\,\Sigma_n^l\big] = \mathrm{Tr}\big[\Sigma_n^l\,G_{nn}\,\big]$). As expected there will be no net current through the leads in an equilibrium situation. Furthermore, when no magnetic field is present, all Green's functions are symmetric: $G(\mathrm{r},\mathrm{r}',E) = G(\mathrm{r}',\mathrm{r},E)$. This will lead to a vanishing equilibrium current density: in the absence of a magnetic field there are no persistent currents.

Nonequilibrium Current

In the nonequilibrium situation, we apply a bias voltage so that the chemical potential of one of the leads is higher than that of the other lead. The current density distribution in this situation is written as (see Appendix C):

$$\begin{aligned} I_{(n-1,m)\to(n,m)} &= \frac{2e}{\hbar}\int\frac{\mathrm{d}E}{2\pi}\,\Big[f_L A - \big(f_L - f_R\big)B\Big], && (5.14\mathrm{a}) \\ I_{(n,m)\to(n,m+1)} &= \frac{2e}{\hbar}\int\frac{\mathrm{d}E}{2\pi}\,\Big[f_L C - \big(f_L - f_R\big)D\Big], && (5.14\mathrm{b}) \end{aligned}$$

with the matrix elements A and C given in Eqs. (5.12), while B and D are given by

$$\begin{aligned} B &= 2\,\mathrm{Im}\Big\langle m\Big|\,G_{nn}\,\Gamma_n^r\,G_{nn}^\dagger\,\big(\Sigma_n^l\big)^\dagger\,\Big|m\Big\rangle\,, && (5.15\mathrm{a}) \\ D &= 2\,\mathrm{Im}\Big\langle m+1\Big|\,(t_{m,n}^y)^*\,G_{nn}\,\Gamma_n^r\,G_{nn}^\dagger\,\Big|m\Big\rangle\,. && (5.15\mathrm{b}) \end{aligned}$$

In these expressions, we have defined

$$\begin{aligned} \Sigma_n^r &= V_{n,n+1}\,G_{n+1,n+1}^R\,V_{n+1,n}, && (5.16\mathrm{a}) \\ \Gamma_n^r &= \mathrm{i}\,\Big[\Sigma_n^r - \big(\Sigma_n^r\big)^\dagger\Big]. && (5.16\mathrm{b}) \end{aligned}$$

In Eqs. (5.14), both the longitudinal and the transverse vertex currents are written as a sum of two terms. The first one depends only on the Fermi-Dirac distribution f_L in the left lead, while the second one is dependent on the difference $f_L - f_R$. This has lead the authors of Refs. [66, 67] to name the first term the persistent (or equilibrium) current contribution, and the second term the transport current (or nonequilibrium) contribution. However, this subdivision cannot be physically relevant: e.g., Eq. (5.14a) can equivalently be written as:

$$I_{(n-1,m)\to(n,m)} = \frac{2e}{\hbar}\int\frac{\mathrm{d}E}{2\pi}\,\Big[f_R A - \big(f_L - f_R\big)\big(B - A\big)\Big]. \qquad (5.17)$$

It is clear that, based on this equation, the division in a transport and persistent current density contribution will be different from the one obtained from Eq. (5.14a), although the total current density remains the same in both cases. Therefore, this kind of separation of the current density in a persistent and transport part cannot be assigned a clear physical meaning as it is not unique.

Nevertheless, since persistent currents are antisymmetric with respect to magnetic field reversal, one could define a pure "transport" current density as the symmetric part of the total current density. Since the matrix elements A and C can be shown to be antisymmetric upon field reversal, this symmetrization procedure would lead to a unique definition of the transport current [Eqs. (5.14a) and (5.17) would give the same result]. Please note that this is different from attributing the persistent contribution to the matrix elements A and C as done in Refs. [66, 67]: the matrix elements B and D are not purely symmetric upon field reversal and they can therefore also contain part of the persistent current density. A more detailed account on issues related to defining transport and persistent current densities can be found in Appendix D.

In the future, when referring to the *transport* current density, we will always mean that part of the total current density in Eqs. (5.14) that is symmetric with respect to time reversal. Since the flow map obtained from the local scatterer method has the same symmetry, it is this transport current that should be relevant. For calculating this symmetric part, we only need to consider the energy integrals in Eqs. (5.14) that have the difference $f_L - f_R$ in their argument, since the matrix elements A and C are asymmetric with respect to time reversal. These integrals can be linearized for small biases:

$$\int \mathrm{d}E \,\big(f_L - f_R\big)\, \alpha(E) = -eV\,\alpha(E_F), \tag{5.18}$$

with the quantity α in the integrand evaluated at the Fermi energy of the device, and $V = V_L - V_R$ the voltage difference over the leads. This has the advantage that one does not need to do a costly numerical integration for obtaining the transport current density in the linear response regime.

It should be noted that although some semiclassical calculations of the current density already showed the branching behavior at large distances from the QPC [15, 61], our fully quantum mechanical calculation will reveal some new (interference) features, as we will see in the next sections. Furthermore, the efficiency of our complete technique will allow for a better comparison between the scanning probe maps and the current density.

5.4 Numerical simulation: Device modeling

One of the goals in the current chapter is a comparison of a numerical simulation of electron flow through a QPC with the experimental results described in Sec. 5.2. In order to do so, we have to choose our model parameters as close as possible to the relevant experimental parameters. In the next three sections, this will be done for the two-dimensional electron gas (2DEG), the disorder in the system, and the QPC model.

5.4.1 Tight-binding parameters for the 2DEG

In Refs. [14, 15], one used a 2DEG at the interface of a GaAs/AlGaAs heterostructure with an electron density $n = 4.5 \times 10^{11}\,\text{cm}^{-2}$. This density corresponds to a Fermi energy of $E_F = 16\,\text{meV}$ and a Fermi wavelength of $\lambda_F = 37\,\text{nm}$. A high mobility of $\mu = 1.0 \times 10^6\,\text{cm}^2 V^{-1} s^{-1}$ could be reached for the 2DEG by using a δ-doping technique: carriers are introduced in the 2DEG by putting the dopant atoms in a separate layer above the 2DEG. This has the advantage that it separates the donor impurities from the conduction electrons in the gas and thus leads to a very high mobility: the elastic mean free path corresponding to the mobility above is $l_m = 11\,\mu\text{m}$, which is larger than the region of a few micrometers over which the probe was scanned. Furthermore, since interference fringes were observed over the whole scanning region, the phase coherence length must have been larger than the system size.

In our calculations, such a system will be discretized on a tight-binding lattice with a lattice constant of $a = 6.2\,\text{nm}$, corresponding to a hopping parameter $t = \hbar^2/(2m^* a^2) = 14.5\,\text{meV}$ (the effective mass of GaAs is $m^* = 0.068\,m$). The Fermi energy is $E_F = 1.1t$, giving a wavelength of $\lambda_F = 6a$, which corresponds exactly to the experimental parameters above. The lattice consists of $N = 1001$ columns and $M = 351$ rows, corresponding to a length of $6.2\,\mu$m, and a width of approximately $2.2\,\mu$m. In our model, this region is bounded by hard-wall boundaries on the top and bottom, while perfect semiinfinite leads are connected to the left and right edges of the sample. The leads have the same width as the sample, namely $M = 351$ lattice sites.

5.4.2 Introducing disorder

Disorder plays a fundamental role in creating the branching behavior of electron flow and should therefore be considered in our model. In a tight-binding Hamiltonian, disorder is most often introduced using the Anderson model [68], which comes down to distributing the on-site energies randomly in an interval $[-W, +W]$. However, electron flow branches could not be observed clearly with this disorder model because the on-site energies vary on too short a length scale so that *smooth* bumps and dips in the potential landscape, which are the driving force behind the branching, are not present.

Therefore we have chosen to use a more realistic disorder model. In a two-dimensional electron gas, there are two main contributions to the disorder potential. One is due to the Coulomb potential of the donor atoms in the two-dimensional δ-layer above the 2DEG, while the other comes from general impurities in the crystal structure of the semiconductor materials used for creating the 2DEG. When comparing experimental values of the sheet density of the donor atoms ($\sigma = 8 \times 10^{12}\,\text{cm}^{-2}$) with the bulk density of the impurities ($\rho = 1.25 \times 10^{15}\,\text{cm}^{-3}$), and taking into account that the donor atoms are positioned quite close to the 2DEG while the impurities are distributed randomly throughout the whole material, one comes to the conclusion that the most significant contribution should come from the donor atoms. For this reason, only these will be considered in our calculations.

The donor atoms will be modeled by point-like positive charges distributed randomly in a two-dimensional lattice above the 2DEG. The distance between the electron gas and this impurity lattice was chosen to be $d = 6a$, while only 1% of the lattice sites was taken to be occupied by a donor atom. Taking into account the effect of screening, the long-range Coulomb potential felt by the electrons in the gas was taken to fall off as α/r^3 (r is the distance from the impurity) [69]. The parameter α describes the strength of the potential: in our calculations, a value of $\alpha = 9a^3t$ was chosen. The values for the concentration of donors, the distance d, and the strength α were chosen to give a sufficiently smooth potential with a mobility of the same order of magnitude as the experimental one: for our disorder configuration we found an elastic mean free path of $l_m \approx 4 \times 10^3 a$ (within the Born approximation), corresponding to a mobility of $\mu \approx 2 \times 10^6\,\mathrm{cm}^2 V^{-1} s^{-1}$).

5.4.3 Quantum point contact model

In principle, one could consider the exact geometry of the split gates used experimentally, and solve the Poisson equation self-consistently to calculate the potential that electrons in the 2DEG experience [70–72]. However, the experimentally observed features are not critically dependent on the exact shape of the quantum point contact and therefore such a thorough (and demanding) approach will not be taken in this thesis. Rather, a simple model approach is found to be sufficient.

A lot of different quantum point contact models have already been proposed in the literature (see, e.g., Refs. [73, 74]), some allowing a better fine-tuning of the potential shape than others. We propose to use a potential of the form

$$V_{\text{QPC}} = W_y\, e^{(x-x_0)^2/\xi^2}\, (y-y_0)^2. \tag{5.19}$$

This potential has a parabolic shape in the transverse direction and its width increases exponentially along the propagating direction. For values $|x - x_0| \gg \xi$, the potential will take a value very close to zero and as such it connects smoothly to the flat potential in the semiinfinite leads. The width of the QPC can be tuned with the parameter W_y, while a larger ξ leads to a smoother (i.e., more adiabatic) variation of the width along the longitudinal direction. A contour plot of the QPC potential is shown in Fig. 5.7(a).

In Fig. 5.7(b), we have calculated the conductance of the quantum point contact as a function of its width. A fixed value of $\xi = 10a$ is taken and only W_y is varied in order to obtain a simple two-dimensional plot, although experimentally a bigger voltage on the split gates would correspond to increase both W_y and ξ in our model. Nevertheless, the quantized steps in the conductance are clearly visible, which means that the chosen value of ξ is sufficiently large to assure that the width of the QPC varies smooth enough even for the largest values of W_y. The conductance steps are not as equally spaced as in the experiment, due to the parabolic model we are using. At $x = x_0$, the parabolic potential has its eigenenergies at

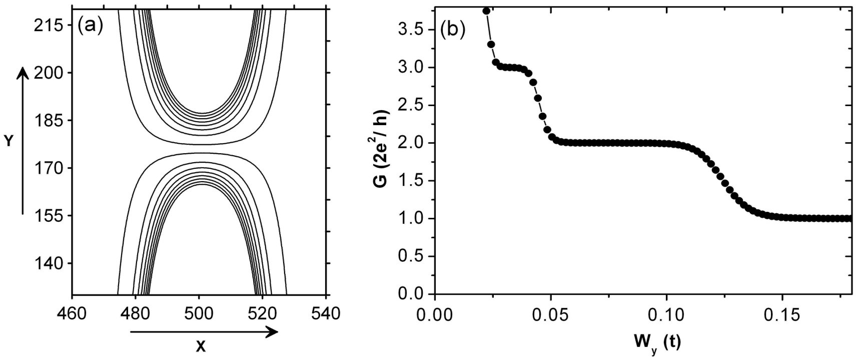

Figure 5.7: Contour plot of the potential used to model the quantum point contact [$\xi = 10a$ and $W_y = 0.56t$] (a). Contours are plotted for energy values of $E = 1, 10, 20, 30, \ldots, 70t$, and lengths on the axes are in units of the lattice constant a. The conductance through the QPC is quantized in steps of $2e^2/h$ [$\xi = 10a$], as depicted in (b).

$E_n = \hbar\omega\,(n + 1/2)$, with $\omega = (2W_y/m^*)^{1/2}$. The n^{th} mode becomes available for transmission when $E_F \geq E_n$: in terms of our tight-binding parameters, the first step is therefore expected at $W_y \approx 1.1t$, the second at $W_y \approx 0.14t$, and the third one at $W_y \approx 0.05t$. Although this model is very simple, we find good agreement with the position of the steps in Fig. 5.7(b) [the step from $G = 0$ to $G = 2e^2/h$ at $W_y \approx 1.1t$ is not shown in the figure].

5.5 Simulation results

5.5.1 Modal pattern close to the QPC

As a first step, we calculated electron flow images at a relatively small distance ($\approx 0.5\,\mu$m) from the quantum point contact. The results are summarized in Fig. 5.8 and should be compared to the experimental ones in Fig. 5.2. The modal pattern of electron flow in this regime is obvious: every time a new mode becomes available for transmission, an extra lobe of flow appears. Furthermore, this pattern is present both with the local scatterer technique as well as with the voltage probe method.

For the local scatterer method, the interference fringes spaced at half the Fermi wavelength resulting from back-and-forth scattering between the scanning probe tip and the QPC are also reproduced in the simulation. On the local chemical potential image, a similar interference effect can be seen. This is due to interference between paths that emerge from the leads and directly enter the voltage probe, and paths that first pass the probe and only enter it after being backscattered off the point contact. This interference leads to small fringes (with wavelength $\lambda_F/2$) in the image obtained with the voltage probe technique. In the current density distribution, such interference fringes are of course absent because they are an “artefact”

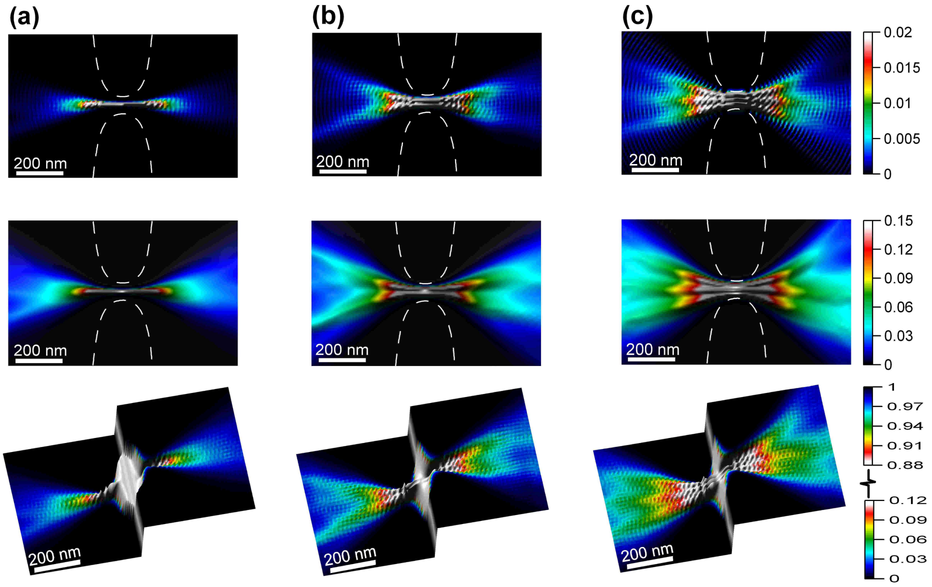

Figure 5.8: Maps of electron flow close to the QPC. In (a), a single mode of the QPC is open for transmission ($W_y = 0.03t$), while (b) and (c) show two and three modes open respectively ($W_y = 0.075t$ and $W_y = 0.56t$). Every new mode creates an extra flow lobe. From top to bottom we show: the local scatterer map, the current density, and the voltage probe map. The Fermi energy contour is depicted as a dotted white line. The color scale has units of $2e^2/h$ for the local scatterer method, while the current density is measured in units of $2e^2(V_R - V_L)/(ha)$. For the voltage probe method, the voltage on the left lead was put $V_L = 0$, and voltage was measured in units of V_R.

of the scanning probe techniques. Apart from this, there is a clear one-to-one correspondence between the scanning probe images and the current density distribution, which proves that both probe techniques are able to visualize local currents in the sample.

When comparing the simulation results for the local scatterer technique with the experimentally measured flow maps in Fig. 5.2, the agreement is very convincing although the magnitude of the conductance decrease in our simulations is smaller than what is observed experimentally. This discrepancy results from modeling the tip as a delta function potential whereas it has a finite width in the experiment.

5.5.2 Branching at larger distances from the QPC

At large distances from the point contact, the experiments showed a striking branching behavior (Fig. 5.3). This feature can also be reproduced with our simulation, as will be shown next. Please note that all images shown in the subsequent sections are taken with a single mode transmitting through the QPC ($W_y = 0.56t$).

In Fig 5.9(a), the calculated current density is shown. The electron flow clearly evolves from a single lobe close to the point contact into multiple branches at larger distances. The number of branches increases as one moves away from the point contact. Branches are reflected upon hitting the top and bottom sample borders, which is a clear indicator for the (quasi)ballistic regime.

Looking closely in the region around such reflection points, an interesting effect is taking place: interference fringes directed perpendicular to the border are visible. This fringe pattern is due to a crossing of two or more coherent electron beams: in

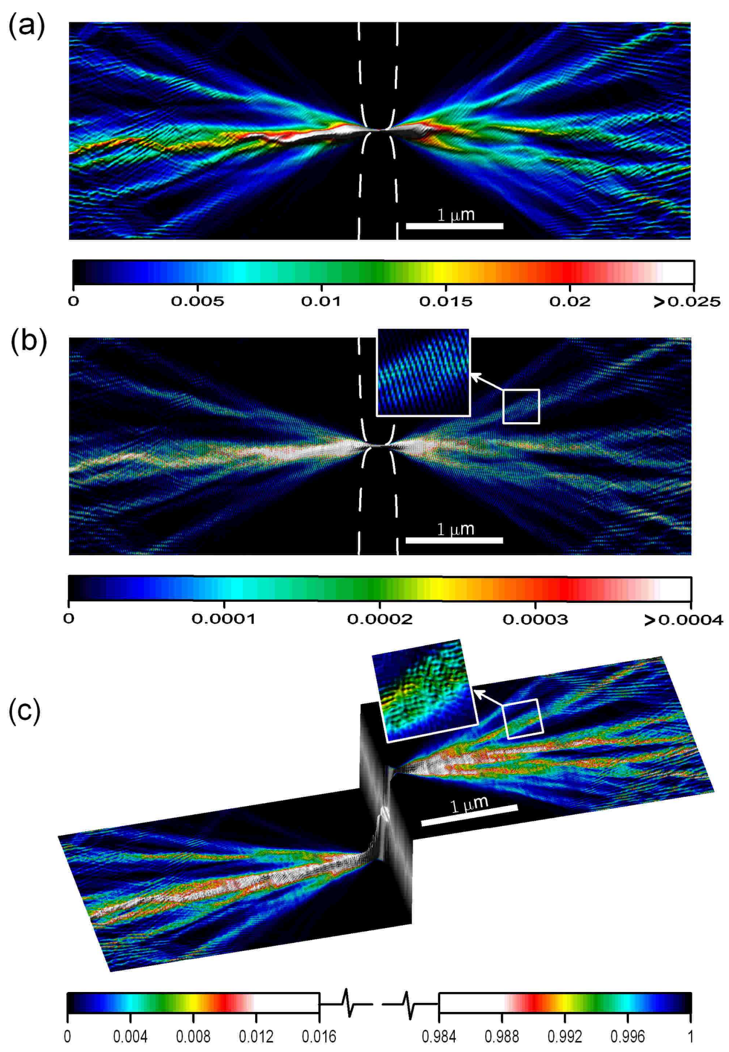

Figure 5.9: Maps of electron flow through a quantum point contact. Current density distribution (a), scanning probe conductance map (b), and scanning probe voltage map (c). Units on the color scales are the same as in Fig. 5.8. The Fermi energy contour is depicted as a dotted white line.

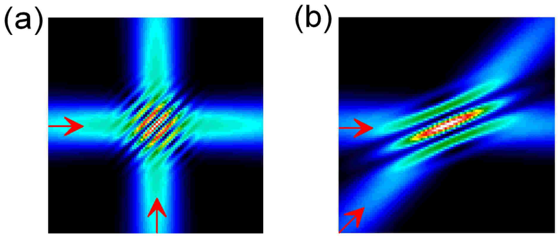

Figure 5.10: Interference between two crossing Gaussian beams. The wavelength of the interference pattern depends on the angle between the beams. Fringes are more closely spaced for an angle of $\pi/2$ (a) than for an angle $\pi/4$ (b).

Fig. 5.9(a), the interference effect is not limited to the boundaries of the sample, but indeed seems to occur at every crossing between branches. To get more insight in this effect, the current density for a model of two crossing Gaussian beams with wavevectors $\mathbf{k_1}$ and $\mathbf{k_2}$ is shown in Fig. 5.10. Interference fringes directed along $\mathbf{k_1} - \mathbf{k_2}$ can clearly be observed, similar to what is observed in Fig. 5.9(a). Comparing Figs. 5.10(a) and 5.10(b), the fringe spacing is seen to depend on the angle θ between the crossing beams: using a simple plane wave model, the wavelength Λ of the interference pattern can be shown to depend on this angle as

$$\Lambda = \frac{\lambda_F}{2\sin(\theta/2)}, \tag{5.20}$$

where $\|\mathbf{k_1}\| = \|\mathbf{k_2}\| = 2\pi/\lambda_F$.

It should be stressed that in the experiments in Refs. [14, 15], this kind of interference behavior was not studied. The small interference fringes observed in the experiments resulted from back-and-forth scattering between the scanning probe tip and the quantum point contact: as such they are an “artefact” of the experimental technique, and do not show up in a current density calculation. Also, they had a fixed wavelength corresponding to $\lambda_F/2$. Although semiclassical calculations of the current density were able to show the branches of electron flow [15, 61], they were of course unable to visualize interference effects between the branches. As such, the interference pattern between crossing branches in Fig. 5.9 is a quite new observation.

With the scanning probe used as a local scatterer [Fig. 5.9(b)], the branches of electron flow can be visualized, as well as their reflections upon sample edges. Even the interference between crossing beams can be observed with this technique, so that in principle this effect could be studied experimentally. There is a clear one-to-one correspondence between the current density in Fig. 5.9(a) and the flow map in Fig. 5.9(b). This proves again that the experimental scanning probe technique is really able to image the current density in the sample. Furthermore, in Fig. 5.9(b), the smaller interference fringes spaced at half the Fermi wavelength are also visible throughout the whole plot [see inset of Fig. 5.9(b)]. As such, all experimental features are reproduced with our simulation (we even predicted a new one), although the magnitude of the conductance decrease in our calculations is again smaller than what is observed experimentally due to the delta function model for the tip.

The voltage probe technique [Fig. 5.9(c)] gives similar information as the previous plots. In our calculations, the voltage on the left lead V_L is put equal to zero, and the right lead is at a positive voltage so that electrons are flowing from left to right. On the left side of the QPC branches appear as regions with increased voltage compared to the voltage on the left lead. This corresponds to a decreased chemical potential ($\mu = -eV$!) due to a deficit of electrons resulting from the nonequilibrium transport process. On the right, the current flow appears as regions with a decreased voltage compared to the voltage on the right lead, corresponding to an increased chemical potential as there is an excess of electrons due to the transport process in this region[2]. Not only the branching behavior can be visualized with the voltage probe method, but also the interference pattern between crossing branches is visible, as well as the smaller interference fringes resulting from back-and-forth scattering between QPC and tip [see inset in Fig. 5.9(c)].

The different interference periodicities in the flow maps can be made more visible by making a Fourier transformation. Fig. 5.11 shows the results of such a transformation on columns 1 to 400 of the three flow maps. In both maps that are produced by the scanning probe techniques, a circle centered on $(k_x, k_y) = (0, 0)$ can be seen. It has a radius of approximately $\frac{2\pi}{3a} = 0.34\,\text{nm}^{-1}$, corresponding to a wavelength $\lambda_F/2$ (remember that $\lambda_F = 6a = 37\,\text{nm}$ in our model). Therefore it corresponds to the interference fringes that decorate the branches, and result from scattering between tip and QPC. Since the branches extend roughly in all directions, the circle shape would indeed be expected. This circle is of course absent in the Fourier transform of the current density.

On the other hand, in all Fourier transformations, including the one of the current density, two smaller circles are present. These result from the interference between crossing branches. They are centered on the X axis because they result from a main beam propagating in the X direction, and other beams at different angles interfering with it. From Fig. 5.9, it is clear that there is indeed a main beam of several branches along the X axis, while other branches are crossing it after they reflect from the borders. Mathematically speaking, if $\mathbf{k_1} = \pm\mathbf{e_x}$ and $\mathbf{k_2} = \cos(\theta)\mathbf{e_x} + \sin(\theta)\mathbf{e_y}$, then the interference fringes are directed along $\mathbf{k_1} - \mathbf{k_2}$ and thus make an angle

$$\phi = \arctan\left[-\frac{\sin\theta}{\pm 1 - \cos\theta}\right] \tag{5.21}$$

with the X axis. The small circles on the Fourier transform in Fig. 5.11 then correspond in principle to nothing more than a plot of $2\pi/(\Lambda e^{\mathrm{i}\phi})$ in the complex plane,

---

[2] In principle, one could compare such picture with water streaming through a constriction at a waterfall from a high plateau to a lower one: the water level will be decreased at the higher plateau at places where water streams, while it will be increased at such places in the lower plateau since water is added there.

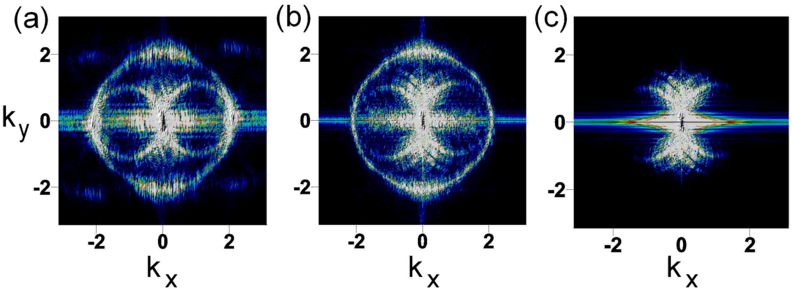

Figure 5.11: Fourier transforms of the flow maps without a magnetic field: local scatterer method (a), voltage probe method (b), and current density distribution (c). Wavevectors are in units of $1/a = 0.16\,\mathrm{nm}^{-1}$, the color scale has arbitrary units.

for all possible values of θ and with the wavelength Λ of the fringes given in Eq. (5.20). Such a plot would indeed reproduce two circles centered on the X axis.

5.5.3 Magnetic field influence

Studying the influence of a magnetic field on the electron flow branches would be the next natural thing to do. However, the effect of a magnetic field is devastating for the local scatterer technique since backscattering will be strongly suppressed, as explained in Sec. 5.3.2. Therefore, no experimental maps of electron flow in the presence of a field are available. Nevertheless, using the scanning probe as a voltage meter, one could in principle obtain flow visualizations in this regime, as we will see next.

In Fig. 5.12, a moderate field is applied to the sample. The magnitude of the field is characterized by a cyclotron radius[3] $r_C = 835a = 5.2\,\mu$m, which is of the same order of magnitude as the sample size. The current density plot shows that the branches of electron flow are bending under influence of the field. The curvature radius roughly corresponds to r_C, so we are seeing here the onset of the cycloidal movement of electrons that was depicted a few pages ago in Fig. 5.5. As expected, the flow map obtained with the local scatterer method [Fig. 5.12(b)] is quite unclear. But still, the tendency of the branches to curve is apparent. The voltage probe method, originally proposed to visualize electron flow in magnetic fields, gives more satisfactory results indeed: the branch bending can be clearly observed in Fig. 5.12(c). When comparing this plot with the current density however, they do not seem to correspond at first sight. This is due to the different symmetry of both plots: the transport current density shown in Fig. 5.12(a) was defined to be symmetric under reversal of the magnetic field. The voltage probe map does not

---

[3] The cyclotron radius is the radius of the circular orbit described by a free electron with velocity v in a magnetic field B: $r_C = m^*v/(eB)$.

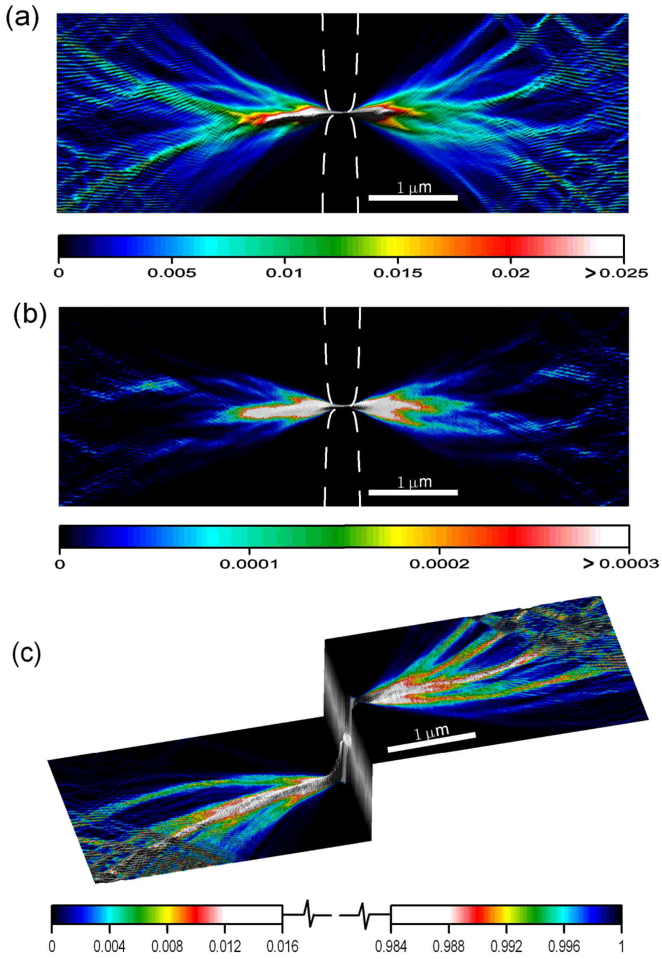

Figure 5.12: Maps of electron flow through a quantum point contact when a moderate magnetic field is applied. Transport current density distribution (a), scanning probe conductance map (b) and scanning probe voltage map (c). Units on the color scales are the same as in Fig. 5.8.

have this symmetry, and therefore the results are different a priori. Nevertheless, when comparing the branches that are present on both plots, they seem to agree very well. The "asymmetry" of the chemical potential map will be discussed in some more detail further down.

When the cyclotron radius becomes smaller than the sample size, one enters the so-called quantum Hall regime, where electrons describe a cycloidal motion along the sample edges. In Fig. 5.13, a magnetic field with a cyclotron radius of $r_C = 24a = 150\,\mathrm{nm}$ is applied to the sample, and the skipping orbits are clearly visible, at least in a plot of the current density. In this regime, the local scatterer method completely fails: the flow map in Fig. 5.13(b) shows no structure at all. Only in the middle of the quantum point contact there is some conductance decrease because it is the only region in which electron waves traveling in opposite directions are overlapping: only here backscattering by a scanning probe tip is possible.

On the other hand, the results in Fig. 5.13(c) very convincingly show that cyclotron orbits can be made visible by using the scanning probe as a voltage probe. Again, the asymmetry of this plot looks strange at first sight, but it has a very clear physical interpretation as will be explained now. Since the magnetic field in our

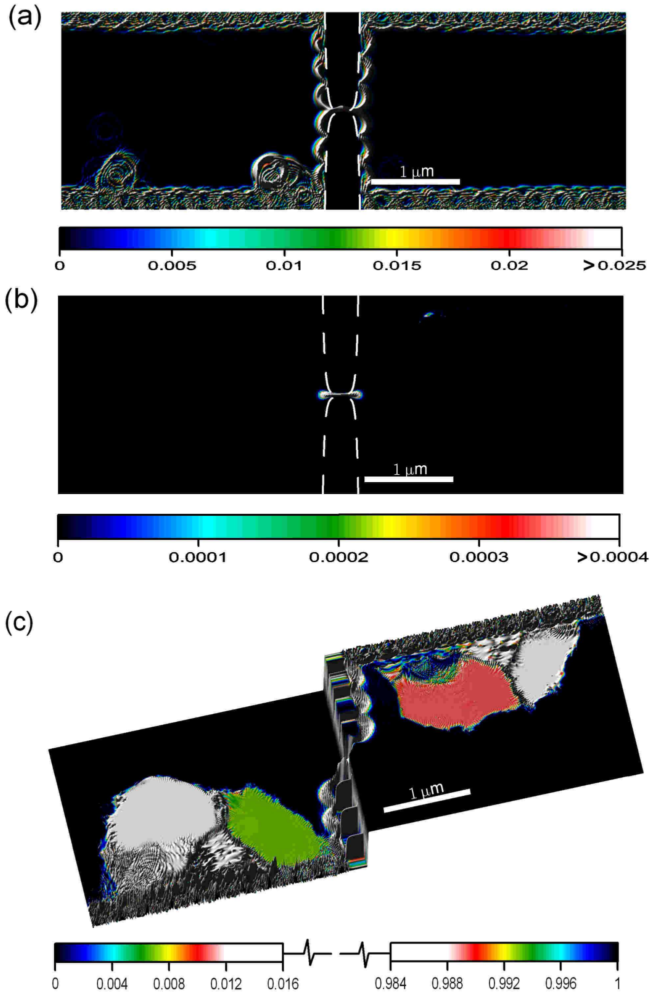

Figure 5.13: Maps of electron flow through a quantum point contact when a high magnetic field is applied. Transport current density distribution (a), scanning probe conductance map (b) and scanning probe voltage map (c). Units on the color scales are the same as in Fig. 5.8.

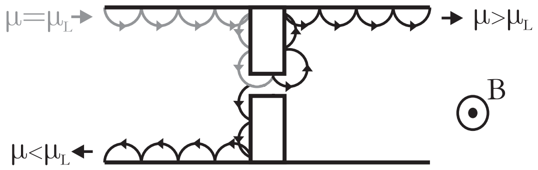

Figure 5.14: Electrons describing skipping orbits while moving from left to right through a constriction. Only in regions where the chemical potential differs from that of the leads will such orbits show up in a voltage probe flow map.

calculations points out of the plane of the paper, and since $V_L < V_R$, electrons are flowing as depicted schematically in Fig. 5.14. All electrons flowing at the upper left edge emerge from the left reservoir, meaning that this edge should have the same chemical potential μ_L as the left lead. This means that the voltage measured on the tip is always equal to V_L at the upper left edge, and we cannot observe skipping orbit structures here (they are depicted gray in Fig. 5.14). When the electron stream reaches the point contact, some electrons are transmitted through it and continue their way at the upper right edge, while others are reflected and continue their path along the lower left edge. The electrons that are transmitted give rise to a chemical potential on the upper right edge that is higher than the one of the right lead (there are an excess of electrons flowing towards the right lead), at least locally in regions where electrons flow. This is picked up by the voltage probe and therefore skipping orbits are visible on this edge. Since part of the electron stream was transmitted towards the right, there are less electrons flowing back to the left lead (along the lower left edge) than originally emerged from it. This means that the chemical potential on the lower left edge will be lower than that of the left lead, and so skipping orbits can also be visualized on this edge. This reasoning explains why skipping orbits can be observed at only two of the four edges with the voltage probe technique.

In conclusion, the voltage probe method is able to visualize local electron transport in the high field regime, whereas the original local scatterer method is not.

5.5.4 Double QPC setup

If one looks at the plot of the transport current with a moderate magnetic field [Fig. 5.12(a)], one can see that some branches bend upwards, while other bend downwards under influence of the magnetic field. This can be interpreted as follows. In the device, the chemical potential will be somewhere between that of the left and the right lead. If one assumes that the chemical potential on the left lead is larger than that on the right, the *transport* current density will have two contributions: one comes from electrons filling scattering states flowing from left to right, the other comes from a deficit of electrons in scattering states going from right to left. This is explained in detail in Appendix D, in Fig. D.2(c). Now, since scattering states going in opposite directions bend in opposite ways under influence of a magnetic field (the direction of the Lorentz force depends on the velocity direction), both up- and downward bending branches are observed.

But this also means that branches curving upwards are emerging from a different lead (reservoir) than the ones bending downwards, so that branches with different chirality should be incoherent. Therefore, an interference pattern at the crossing of two branches as discussed in Sec. 5.5.2 (Fig. 5.10), cannot form between branches with opposite chirality.

In order to prove this statement, a system of two QPCs placed above each other can be considered. Results are shown in Fig. 5.15 for a moderate magnetic field ($r_C = 835a$). One can see the interference between beams with the same chirality,

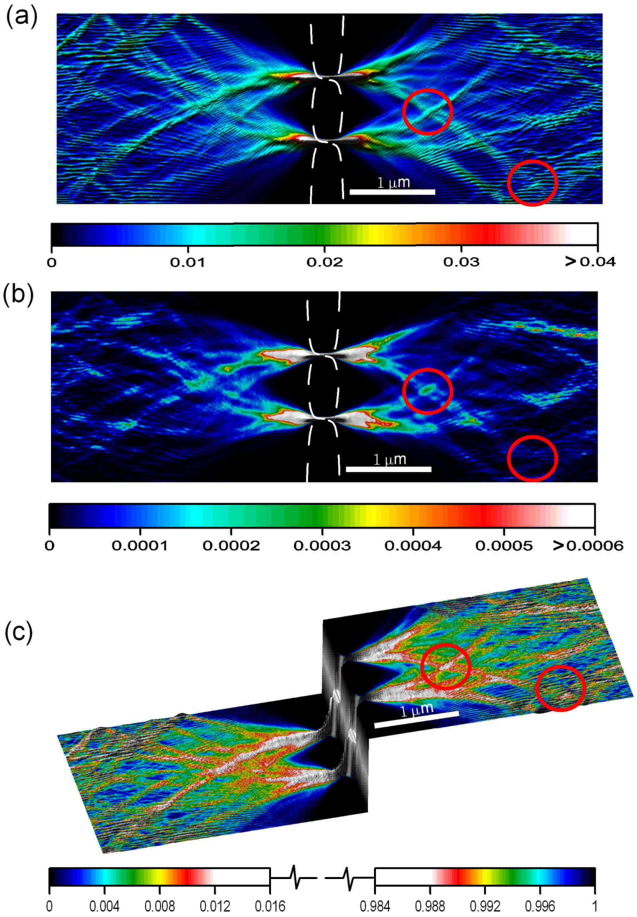

Figure 5.15: Maps of electron flow through a double quantum point contact with a moderate magnetic field. Transport current density distribution (a), scanning probe conductance map (b) and scanning probe voltage map (c). Units on the color scales are the same as in Fig. 5.8.

but there is no interference at the crossing of two beams with opposite chirality, as we expected. This distinction becomes clear when comparing the crossings encircled in Fig. 5.15. To make things more visible, we have smoothed out the interference fringes in Fig. 5.15(b) resulting from scattering between tip and QPC which had a wavelength of $\lambda_F/2$. In Fig. 5.15(c), we symmetrized the voltage probe plot with respect to the direction of the magnetic field in order to be able to compare it to the current density. In all plots, the behavior for coherent beams crossing is different from that for incoherent branches proving that the difference could be studied experimentally.

5.6 Conclusions

In recent experiments, a scanning probe technique was used to obtain local information about electron flow in a two-dimensional electron gas. The obtained images are interesting both from an experimental and theoretical point of view.

In this chapter, it was shown that our extended Green's function technique allows for a very efficient numerical simulation of the scanning probe experiments. One of the aims of such simulations consisted in facilitating the interpretation of the experiments. In particular, calculations on electron flow through a quantum point contact reproduced all features observed experimentally. On top of this, we were able to calculate the current density distribution in the sample in a fully quantum mechanical way. The one-to-one correspondence between the latter quantity and a simulation of the experiment proved that the scanning probe technique is really able to image current flow through a two-dimensional sample.

It was further argued that the original scanning probe method cannot give the desired results when a magnetic field is present. To resolve this, another probe technique was proposed that allows for a measurement of the local chemical potential in the sample. Cyclotron orbits of electrons along the borders of the sample could be successfully visualized in the high field regime, which proved the usefulness of the technique.

Another new result concerns an interference phenomenon resulting from the crossing of coherent beams of electron flow. This effect could be visualized with both probe techniques, so that in principle an experimental investigation of the effect should be possible in the future. At crossings of incoherent beams, the interference effect does not take place, and a setup with two point contacts was proposed for distinguishing between crossings of coherent and incoherent beams in one and the same sample.

Our simulation method is sufficiently general, and the information obtained by the different imaging tools very broad so that it can be used to study electron flow in a wide variety of two-dimensional systems, ranging from, e.g., the quantum Hall effect [33] to quantum chaos in electron billiards [75]. Moreover, including the spin degrees of freedom is straightforward: in principle all Green's functions expressions shown in this chapter are still valid when spin is included. The difference would be that matrix elements of the Green's function operators become 2×2 spinors themselves (as explained in Chap. 3), leading only to a longer computing time. Including spin allows for an even broader range of phenomena to be studied: e.g., we may hope to shed some light on transport in the spin Hall regime [25–27], which is a heavily debated topic at the moment in which lots of questions remain to be answered.

Chapter 6

Noncoherent effects in transport through a four-contact ring

6.1 Introduction

Quantum coherence in a mesoscopic system can lead to very interesting features in its transport properties. This was already beautifully demonstrated in the previous chapter, where a wealth of interference effects left their signature in the calculated electron flow maps. If one uses the Landauer-Büttiker formalism to explain such features, the phase coherence length of the sample is intrinsically assumed to be infinite. In practice however inelastic scattering events, e.g., phonon or electron-electron scattering, are always present and the coherence length of the sample is finite. As a result, all interference effects will be smeared out to some extent.

A modeling of such phase randomizing processes proves to be difficult because it is in general a many-body problem. In principle, the Keldysh Green's function formalism [76–79] is able to incorporate phase-breaking interactions on the microscopic level into the transport equations of a device, but the formalism is quite tedious and the obtained equations are in general quite sophisticated so that one looses the overview in the problem pretty fast. However, it was Büttiker who proposed that phase-breaking processes can be modeled even within the Landauer-Büttiker formalism: in his proposal, an extra voltage probe attached to the sample can act as an inelastic scattering center [80]. Although the model is purely phenomenological, it can give some insight into the influence of inelastic effects while simultaneously keeping hold of the intuitive clearness of the Landauer-Büttiker formalism. Nevertheless, only few papers [81–83] have implemented the proposal, and this because of numerical reasons: standard recursive Green's function techniques are unable to calculate all necessary transmission coefficients between the extra attached voltage probes, so that one has to resort to inefficient direct inversion methods for solving the problem.

In this chapter, it will be shown how to treat the regime of weak inelastic scattering very efficiently with a perturbation approach of Büttiker's proposal. Within this approach all necessary transmission coefficients can be obtained by our extended recursive technique, resulting in a highly efficient method. Although we will only be able to treat phase coherence lengths that are larger than the system size, this is in principle exactly the interesting regime for mesoscopic systems.

Our method will be applied to the study of transport in a ring connected to four leads. When a magnetic flux pierces through the center of such a ring, a Hall effect can be observed that does not rely on the Lorentz force. Instead it is completely due to interference between clockwise and counterclockwise propagating paths around the ring [84, 85]. Therefore, this Hall effect is expected to be washed out slowly when decreasing the phase coherence length, something we will confirm with our numerical simulations.

6.2 Modeling inelastic effects

6.2.1 Büttiker's proposal

As explained in Chap. 2, the Landauer-Büttiker (LB) formalism is concerned with systems consisting of a central device connected to leads which are used to measure current-voltage relationships, and the formalism can in principle only be applied when transport in the central device is coherent. Nevertheless, the leads are connected to large reservoirs with a chemical potential that is assumed to be well-defined even in the presence of electronic transport through the device. For such an assumption to be reasonable it is clear that phase breaking (equilibration) processes must be taking place inside the reservoirs because otherwise they cannot have a well-defined equilibrium distribution.

It is this insight that was exploited by Büttiker to arrive at the idea that the attachment of an extra lead/reservoir can simulate a phase randomizing process in the central device [80]. The reasoning behind this goes as follows. If the extra lead does not draw current (we will call this a voltage probe), then for every electron entering the lead from the sample, another one has to come out. But since equilibration is taking place in the reservoir connected to the extra lead, the electron injected back into the sample is not coherent with the one that originally left it. So when an electron is absorbed (and later reemitted) from a voltage probe, it looses its phase memory and in this way it is possible to model a single phase breaking event with a voltage probe.

In practice, phase randomizing processes are distributed throughout the whole system, and a realistic modeling will therefore involve the attachment of a large number of extra voltage probes. In Fig. 6.1, a possible model setup is given. The central device is connected to real physical leads that are used to measure current-voltage characteristics of the sample. They would thus also be present in an experimental setup and will be referred to as *contacts* from now on (labeled by Latin letters $m, n, \ldots$). On the other hand, every phase randomizing process can be modeled by the attachment of a single *voltage probe*, as explained previously. The voltage probes can be thought to extend in a direction perpendicular to the two-

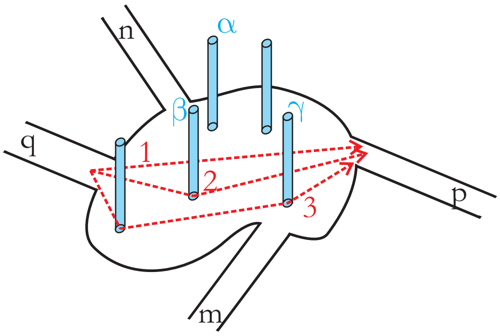

Figure 6.1: Modeling inelastic processes. Every voltage probe (blue tubes labeled $\alpha, \beta, \ldots$) models a single inelastic scatterer: after absorption (and reinjection) by one of them, an electron looses coherence. Transmission from contact q to p goes either coherently without any scattering (path 1), or after scattering inelastically a single (path 2) or multiple times (e.g., path 3).

dimensional sample (see Fig. 6.1) and are labeled by Greek letters. They are just there for model purposes, and would not be present in a real-life experiment.

To describe the outcome of an electrical measurement on this system, an expression for the currents and voltages through the contacts is needed, taking into account effectively the influence of the phase breaking voltage probes. For obtaining this relationship, one proceeds as follows. Within the LB formalism, the current at voltage probe α can be written in terms of transmission coefficients between the leads [Eq. (2.2)]:

$$I_\alpha = \frac{2e^2}{h} \sum_m T_{\alpha m} \big(V_\alpha - V_m \big) + \frac{2e^2}{h} \sum_{\beta \neq \alpha} T_{\alpha\beta} \big(V_\alpha - V_\beta \big). \tag{6.1}$$

Since lead α is a voltage probe, one has $I_\alpha = 0$, so that from the previous equation one can derive an expression for the voltage V_α:

$$V_\alpha = \frac{\sum_m T_{\alpha m} V_m + \sum_{\beta \neq \alpha} T_{\alpha\beta} V_\beta}{S_\alpha}, \tag{6.2}$$

where we have defined

$$S_\alpha = \sum_n T_{\alpha n} + \sum_{\gamma \neq \alpha} T_{\alpha\gamma}. \tag{6.3}$$

On the other hand, the current through contact p can be written as

$$I_p = \sum_{q \neq p} T_{pq} \big(V_p - V_q \big) + \sum_\alpha T_{p\alpha} \big(V_p - V_\alpha \big). \tag{6.4}$$

Inserting Eq. (6.2) for V_α into this expression, one obtains after some algebraic manipulation

$$I_p = \sum_q T_{pq}^{\text{eff}} \big(V_p - V_q \big), \tag{6.5}$$

with

$$T_{pq}^{\text{eff}} = T_{pq} + \sum_{\alpha} \frac{T_{p\alpha}T_{\alpha q}}{S_\alpha} + \sum_{\alpha}\sum_{\beta\neq\alpha} \frac{T_{p\alpha}T_{\alpha\beta}T_{\beta q}}{S_\alpha S_\beta} + \dots . \tag{6.6}$$

This is exactly the expression we are looking for. It has the same form as the LB formula for a system connected to the contacts only. Nevertheless the details of the voltage probe influence are taken into account by means of the effective transmission probabilities. The expression furthermore has a clear physical interpretation. The first term in Eq. (6.6) describes direct transmission from contact q to contact p without entering any voltage probe: it describes the coherent contribution. The next term incorporates absorption and reemission from a single voltage probe α, and thus describes a single inelastic scattering process. The following term describes two subsequent scattering processes during the transmission from q to p, and so on (see also Fig. 6.1).

Now that it has become clear how voltage probes attached to the central device can be used to describe phase randomizing processes in a phenomenological way, let's see how this idea can be implemented in a tight-binding description of the system.

6.2.2 Tight-binding implementation

In our tight-binding calculations, the voltage probes used to simulate inelastic effects will be modeled by a one-dimensional (1D) lead. Every single lattice site of the central device is connected to such a 1D voltage probe, so as to give a homogeneous distribution of inelastic scattering centers throughout the sample. As shown in Chap. 4, the influence of a lead on the central device can be described by adding its self-energy to the on-site energy of the site it is attached to. For a 1D lead, this self-energy is known analytically [2]:

$$\Sigma_{vp} = -t_{vp}\, e^{\mathrm{i}\,\arccos\left[1-(E_F-U)/(2t)\right]} . \tag{6.7}$$

In this expression, E_F is the Fermi energy of the electrons, and t is the hopping matrix element between sites in the lead, while t_{vp} describes the hopping element to the site in the device to which the lead is connected. The parameter U corresponds to the value of a fixed potential in the lead and can thus be used to shift the bottom of its energy band. We will choose $U = E_F - 2t$, so that the self-energy Σ_{vp} reduces to

$$\Sigma_{vp} = -\mathrm{i}t_{vp}. \tag{6.8}$$

The influence of the leads then would be to add a constant imaginary potential to every site in the device. Such an imaginary potential introduces a finite lifetime in the device, given by

$$\tau_\phi = \frac{\hbar}{2t_{vp}}, \tag{6.9}$$

which corresponds to the phase relaxation time introduced by the 1D voltage probes. We have control over this lifetime by tuning the hopping element t_{vp}.

But the approach goes further than just adding an imaginary potential: one has to solve the complete set of Landauer-Büttiker equations taking into account that the current through every voltage probe is zero. This will assure that current conservation is satisfied in the device: no current is lost via the extra leads attached to the sample. Solution of the equations results in expressions for the currents and voltages on the contacts in terms of effective transmission coefficients T^{eff}_{pq}, as was already shown in the preceding section [see Eqs. (6.5) and (6.6)]:

$$T^{\text{eff}}_{pq} = T_{pq} + \sum_{\alpha} \frac{T_{p\alpha}T_{\alpha q}}{S_\alpha} + \sum_{\alpha}\sum_{\beta\neq\alpha} \frac{T_{p\alpha}T_{\alpha\beta}T_{\beta q}}{S_\alpha S_\beta} + \dots . \tag{6.10}$$

To complete our discussion on the implementation of Büttiker's proposal, the only thing still missing is a numerical method for calculating the transmission coefficients in Eq. (6.10). They can be subdivided in three categories:

(1) transmission coefficients T_{pq} between mutual contacts
(2) transmission coefficients $T_{p\alpha}$ (or $T_{\alpha p}$) between a contact and a voltage probe
(3) transmission coefficients $T_{\alpha\beta}$ between mutual voltage probes.

Geometrically, we can always arrange our setup so that all contacts are attached at sites of the first and last column of the tight-binding lattice [compare, e.g., the ring setups in Figs. 6.2(a) and 6.2(b)]. As such, using Eq. (4.7) in Chap. 4, transmission coefficients of the first two types can be expressed in terms of Green's functions between the first and last column of the device (type 1), or between the first/last column and any other site in the device (type 2). This subset of Green's functions is available with the extended recursive technique explained in Chap. 4. However, for the calculation of transmittances of the third category, one needs access to the Green's function between every two sites in the tight-binding lattice. Unfortunately, there is no very efficient numerical technique for obtaining these: in principle one should resort to a direct inversion of the complete Hamiltonian, which is very costly for bigger systems. This inefficiency is the reason that Büttiker's proposal has not been implemented numerically very often in the literature: only a one-dimensional chain [81] and a small two-dimensional Hall cross [82, 83] were studied.

Our idea now is to neglect all terms in Eq. (6.10) involving two or more subsequent scattering events by putting the transmission coefficients $T_{\alpha\beta}$ equal to zero by hand. Such an approximation, in which only the coherent and the single inelastic scattering contribution are kept, would be valid only when the phase coherence length is larger than the system size. This is not a big problem since in principle this is exactly the regime one is interested in when studying mesoscopic systems. Nevertheless, the "perturbation" approach has one small disadvantage: current conservation will be violated since higher order terms in the effective transmission coefficients are simply truncated. In principle, small currents will be flowing through the voltage probes and are "lost" from the central device. However, in a regime where only weak inelastic scattering is considered, this error will be negligible since the hopping element from the sample to the voltage probes will be small [see Eq. (6.9)].

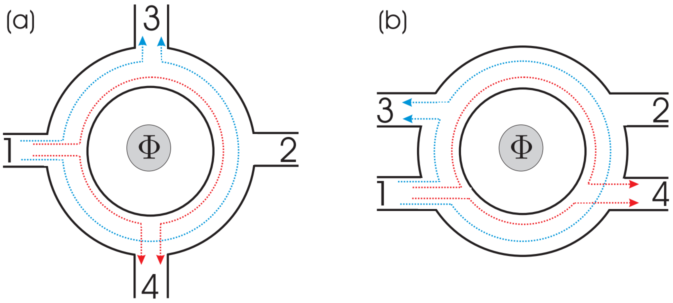

Figure 6.2: Two setups for a four-contact ring. Interference between paths between lead 1 and 3 (blue) and those between lead 1 and 4 (red) can give rise to a Hall voltage difference $V_3 - V_4$ when a magnetic flux pierces through the ring. In (a), the leads are contacted symmetrically so that red and blue paths are equivalent in the absence of magnetic flux and $V_3 - V_4 = 0$ (supposed no disorder is present). For numerical reasons however, we are forced to use a setup as in (b), with the leads attached at the left and right edges. In this case, blue and red paths are not equivalent and a voltage difference between contacts 3 and 4 develops even in the absence of a magnetic flux, so another observable is needed to quantify the Hall effect.

6.3 Transport in a four-contact ring

6.3.1 Hall effect without Lorentz force

In order to apply our phase breaking model, we will consider a four-contact ring setup as shown in Fig. 6.2. A magnetic flux is piercing through the center of the ring, while there is no field through the ring arms. Although there is no Lorentz force acting on the electrons moving in the arms of such a ring, a special kind of Hall effect can still be observed that is completely due to quantum interference.

Indeed, suppose an electron enters the ring through lead 1. It can reach lead 3 by different paths: there is a direct path between lead 1 and lead 3, but there is also a trajectory going as $1 \to 4 \to 2 \to 3$. These two trajectories will interfere with each other, and fix the voltage on lead 3 (neglecting paths encircling the ring more than once). The same can be applied to lead 4: again a direct and an indirect path are interfering and set the voltage on lead 4. The voltages on lead 3 and lead 4 are equal when no flux pierces through the ring [at least when the leads are positioned symmetrically as in Fig. 6.2(a)]. However, when a magnetic flux is applied through the ring center, the time reversal symmetry is broken and the phase difference between both paths going from 1 to 3 is different from that for the paths going from 1 to 4, so that a voltage difference $V_3 - V_4$ can develop. This Hall effect is closely related to the original Aharonov-Bohm effect [86]: although no Lorentz force acts on the electrons, they can feel the vector potential created by the flux tube which changes their phase in a way that is dependent upon their movement direction around the ring.

For a one-dimensional ring, this Hall effect was already described in some detail in Ref. [84], while numerical calculations for a simple model were shown in Ref. [85]. In a subsequent section, we will show numerical results for a more realistic and experimentally realizable four-contact ring, which will indeed reveal the existence of the Hall effect. Furthermore, since the effect is purely due to quantum interference, one expects it to be washed out when inelastic scatterers are introduced in the sample. As such, the four-contact ring can serve as a test bed for our implementation of Büttiker's proposal.

6.3.2 An expression for the Hall resistance

It should be noted that a nonzero transverse resistance $R_{12,34} = \frac{V_3 - V_4}{I_1}$ does not necessarily point to the Hall effect we are interested in. For instance, when leads 3 and 4 are placed asymmetrically, as in Fig. 6.2(b), the path length from 1 to 3 (or $1 \rightarrow 4 \rightarrow 2 \rightarrow 3$) is different from the one going from 1 to 4 (or $1 \rightarrow 3 \rightarrow 2 \rightarrow 4$), so that a voltage difference $V_3 - V_4$ will develop even in the absence of a magnetic flux. In principle, this is due to the fact that a part of the longitudinal resistance is picked up when measuring $R_{12,34}$ in a setup as in Fig. 6.2(b). To resolve this problem, one defines the Hall resistance as

$$R_H = \frac{1}{2}\big(R_{12,34} - R_{34,12}\big), \tag{6.11}$$

where we use the common notation

$$R_{kl,mn} = (V_m - V_n)/I_k \tag{6.12}$$

for a measurement where current is supplied through contacts k and l, and the voltage difference $V_m - V_n$ is measured, fixing $I_m = I_n = 0$. It was shown by Büttiker that the Hall resistance R_H in Eq. (6.11) is that part of the transverse resistance that is antisymmetric with respect to time reversal, and is thus zero when there is no magnetic field [36]. As such, this quantity is exactly what we need to quantify the Hall effect. In principle, this definition is equivalent to defining the Hall resistivity ρ_H in a macroscopic system as the antisymmetric part of the resistivity tensor: $\rho_H = 1/2\,(\rho_{xy} - \rho_{yx})$.

The four-contact resistances $R_{kl,mn}$ defined in Eq. (6.12) can be expressed in terms of transmission coefficients between the contacts by solving the Landauer-Büttiker equations of Eq. (6.5). One obtains [36]:

$$R_{kl,mn} = \frac{h}{2e^2}\frac{T^{\text{eff}}_{mk}T^{\text{eff}}_{nl} - T^{\text{eff}}_{nk}T^{\text{eff}}_{ml}}{D}, \tag{6.13}$$

where D is an arbitrary 3×3 subdeterminant of the matrix A relating the currents through the four contacts to their voltages [$I_p = \sum_q A_{pq} V_q$, c.f. Eq. (6.5)].

It is very important to understand that the Hall resistance R_H in a mesoscopic system will depend both on the geometry of the sample and on the exact configuration of impurities, because it is sensitive to interference effects. Indeed, the positions of impurities, the lengths of the sections between the contacts and the shape of the ring will set the lengths of different interfering paths. As such, the results will be quantitatively different for different samples, even different impurity configurations suffice. This however, is an integral part of the physics of mesoscopic systems.

6.3.3 Results

In this section, both the Hall resistance R_H and the longitudinal resistance $R_{12,12}$ will be calculated for a four-contact ring as depicted in Fig. 6.2(b), and the influence of inelastic scattering on these quantities will be made clear. The setup of Fig. 6.2(b) was chosen for numerical reasons: it has the leads attached to the left and right edge of the sample, so that recursive techniques can be applied to calculate the transmission coefficients. The ring parameters were chosen to mimic rings that can nowadays be fabricated easily in a two-dimensional electron gas at the interface of an GaAs-AlGaAs heterostructure. The density of the gas was chosen to be $n_s = 4 \times 10^{11}\,\text{cm}^{-2}$, corresponding to a Fermi wavelength of $40\,\text{nm}$. The ring has a mean radius of $0.6\,\mu$m, and the width of the arms is $200\,\text{nm}$, so that 10 transverse channels are available for conduction. The mobility of the electron gas is chosen to be $\mu = 5 \times 10^5\,\text{cm}^2\,\text{V}^{-1}\,\text{s}^{-1}$, giving a mean free path of $5.2\,\mu$m (quasiballistic regime).

In our tight-binding calculations, the lattice constant was chosen to be $a = 6.7\,\text{nm}$, giving a hopping parameter $t = \hbar^2/(2m^* a^2) = 12.4\,\text{meV}$. The parameters of the electron gas above then correspond to a wavelength $\lambda_F = 6a$ and a Fermi energy $E_f = 1.1t$. For the ring, the mean radius corresponds to $89a$, while the ring width is $29a$. Elastic scattering was modeled with the Anderson model, in which the on-site energies in the ring arms are distributed randomly in the interval $[-0.127t, 0.127t]$. Within the Born approximation, this gives a mean free path of $l_m = 780a$.

Inelastic scattering processes are modeled by the attachment of extra voltage probes to every site of the lattice, as explained in the preceding sections. The corresponding phase coherence length of the sample is given by $L_\phi = \sqrt{D\tau_\phi}$, where $D = 1/2\, v_F l_m$ is the diffusion constant (v_F is the fermi velocity of the electrons) and the phase relaxation time τ_ϕ was defined in Eq. (6.9): it can be controlled by tuning the hopping element between the voltage probes and the samples. Doing so, we have varied the phase coherence length between $L_\phi = 6\,\mu$m and $L_\phi = \infty$, thereby staying within the range of validity of our perturbative approach: L_ϕ is clearly larger than the system size.

In Fig. 6.3(a), the Hall resistance R_H in such a ring is calculated. The resistance varies periodically with the magnetic flux through its center, and the period corresponds to one fundamental flux quantum $\Phi_0 = h/e$. We have sufficed with showing only one period in the figure. A finite value of R_H is observed for almost all flux values, showing clearly the existence of a Hall effect. Please remember that there is no Lorentz force acting on the electrons since no magnetic field is present in the ring arms. Rather, as explained previously, the effect is due to quantum in-

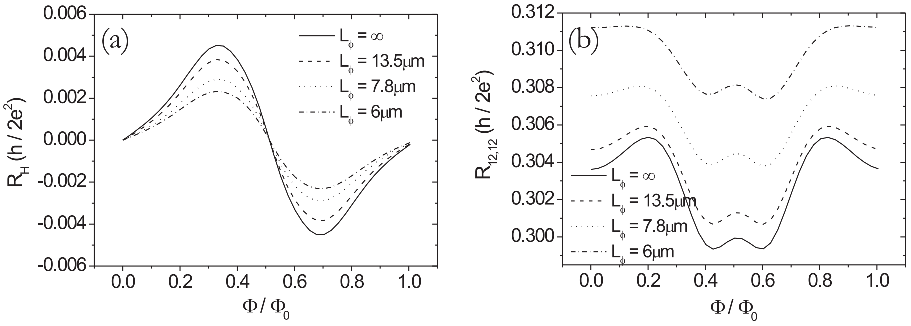

Figure 6.3: The Hall resistance (a) and longitudinal resistance (b) in the four-contact ring for different values of the phase coherence length.

terference. This explanation is supported by the fact that the effect is washed out slowly as we decrease the phase coherence length of the sample (compare the solid curve with the dotted/dashed ones in the figure).

At zero flux, R_H is equal to zero as it was defined to be antisymmetric with respect to the magnetic field direction. Because of the periodicity of the resistance, this zero value of course repeats whenever Φ/Φ_0 is integer. The combination of asymmetry/periodicity furthermore explains why R_H should be zero for half-integer ratios of Φ/Φ_0: on one hand we have $R_H(-\Phi_0/2) = R_H(\Phi_0/2)$ because of periodicity, while antisymmetry leads to $R_H(-\Phi_0/2) = -R_H(\Phi_0/2)$, so that indeed $R_H(\Phi_0/2) = 0$.

Turning our attention to the longitudinal resistance $R_{12,12}$ in Fig. 6.3(b), the well-known Aharonov-Bohm (AB) oscillations can be observed. They again have a period of Φ_0, since they result from interference between the two paths $1 \to 3 \to 2$ and $1 \to 4 \to 2$ that enclose the ring once. The small bump at $\Phi/\Phi_0 = 1/2$ is a signature of the second harmonic of the AB oscillations, which results from interference between two paths that separately encircle the complete ring once before interfering. The influence of inelastic scattering on the longitudinal resistance is twofold. First, the mean value of the resistance will increase because we are introducing extra scatterers: the resistance curves are shifted upwards when decreasing L_ϕ. Second, the amplitude of the AB oscillations decreases with decreasing coherence length, because they are the result of interference effects.

Comparing the magnitude of the Hall resistance in Fig. 6.3(a) with that of the longitudinal resistance fluctuations shown in Fig. 6.3(b), we see that they both are of the same order. Since the experimental study of Aharonov-Bohm oscillations is technically well-established nowadays, it should also be feasible to measure the Hall resistance in the four-contact ring. The only problem in an experimental setup is the confinement of the magnetic flux to a region inside the ring without any stray field penetrating the ring arms. In most experiments the magnetic field is therefore

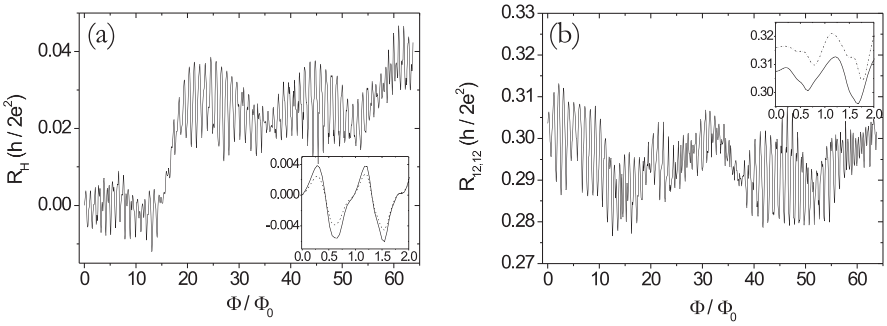

Figure 6.4: Hall resistance (a) and longitudinal resistance (b) of the four-contact ring when a magnetic field is applied across the whole sample. Φ is now defined as the flux through the mean radius of the ring. The effect of inelastic scattering is shown in the inset for the two first oscillation periods: $L_\phi = \infty$ (solid curve) and $L_\phi = 7.8\,\mu$m (dashed curve).

applied across the whole sample. By using rings with narrow arms compared to the ring diameter, one tries to minimize the effect of the field through the arms.

In Fig. 6.4, we show calculation results for such a case where the magnetic flux is applied in the whole sample, in order to compare with a realistic experimental setup. The resistances are not anymore strictly periodic with respect to the flux. Nevertheless quasiperiodic oscillations are visible resulting from quantum interference. Their amplitude will decrease when introducing inelastic scattering, as shown on the insets of Fig. 6.4. Another effect of the field through the arms is the beating pattern that can be observed in the oscillations of both the longitudinal and Hall resistances. It can be explained as follows. Because the ring arms are quite wide, electrons can propagate in different transverse channels through the ring. Their corresponding "classical" trajectories surround slightly different areas, and thus different fluxes since a magnetic field is present in the ring itself. The periodicity of the oscillations thus varies slightly for every channel, which results in a beating pattern when the contributions from all channels are summed up.

6.4 Conclusions

Incorporating the effect of phase randomizing processes in a phenomenological way can be done with the attachment of extra voltage probes to sample, an idea originally proposed by Büttiker [80]. In this chapter, we have described a perturbation approach to this idea that allows for calculating all necessary transmission coefficients with our extended recursive technique. Doing so, one is able to treat inelastic effects in a numerically very efficient way, which was not possible within the original proposal. The approach however consists of neglecting multiple inelastic scattering and is therefore only valid in a regime where the phase coherence length is larger than the system size.

The method was applied to an experimentally realizable ring with four attached contacts, and a Hall effect was observed which is due to quantum interference rather than an implicit Lorentz force acting on the electrons. For this reason, the observed Hall effect disappeared when decreasing the phase coherence length.

Chapter 7

Topological Hall effect

7.1 Introduction

During the last decades, a wide range of Hall effects has appeared in the literature [25, 27, 33]. In the classical Hall effect, discovered more than a century ago, the Lorentz force resulting from a magnetic field B_z applied perpendicular to a two-dimensional sample gives rise to an electric field E_y perpendicular to the applied current I_x through the sample. As a result, a transverse resistivity $\rho_{xy} = E_y/j_x$ can be defined (j_x is the current density). The Drude model [87] shows that this resistivity is linear in the magnetic field[1]: $\rho_{xy} = R_0 B_z$, with the Hall coefficient $R_0 = \frac{1}{n_q q}$ (q is the charge of the current carriers, n_q the carrier density).

In ferromagnetic systems, an extra contribution to the off-diagonal resistivity was found: $\rho_{xy} = R_0 B_z + R_s M$. This anomalous contribution is proportional to the magnetization M, and gives rise to a Hall effect even in the absence of an externally applied magnetic field. A lot of experimental work was devoted to this so-called anomalous Hall effect, and resulted in some empirical laws for the coefficient R_s. Nevertheless, it took more than sixty years to clear up the origin of the effect theoretically. Finally, it was agreed upon that the effect is due to spin-orbit coupling, which gives rise to two scattering mechanisms, skew scattering [88–90] and side jump [91, 92], that introduce different preferential scattering directions for spin-up and spin-down particles. As a result, the incoming spin-up particles would be scattered towards one edge of the sample, and spin downs to the opposite edge. In a ferromagnet, the spin subbands are unequally populated and this spin scattering imbalance leads to a charge accumulation at opposite edges, creating a transverse electrical field and thus explaining the anomalous contribution to the off-diagonal resistivity[2].

---

[1] In high magnetic fields, the linear relation between ρ_{xy} and B_z breaks down: instead ρ_{xy} shows flat plateaus with quantized resistance values at $\rho_{xy} = h/(n2e^2)$ with n integer. This is called the quantum Hall effect, and was discovered experimentally in the beginning of the eighties [33].

[2] In a normal semiconductor, the same spin-orbit scattering mechanisms are present, and although in this case there is no net charge accumulation, there will be a spin accumulation at opposite edges, giving rise to the so-called spin Hall effect [25].

Very recently however, the behavior of the anomalous coefficient R_s in certain types of frustrated ferromagnetic systems with noncoplanar magnetic moments, like some pyrochlore-type compounds [93] or spin glasses [94], was found to be in contradiction with the expectations from the spin-orbit scattering theory. In order to explain the anomalous Hall effect in these systems, a mechanism was proposed based on the Berry phase [95] an electron acquires when its spin follows the spatially varying magnetization that is present in such materials [96]. Since the effect can be attributed to the topology of the magnetization texture, the term topological Hall effect was coined [32].

However, a quantitative comparison between the proposed theory and the experiments on, e.g., the pyrochlore compounds proves to be difficult: in experiments, both the spin-orbit scattering and the Berry phase mechanism are simultaneously present, and it is therefore difficult to distinguish between them. Making such a distinction is further complicated by the fact that quantitative experimental information on the magnetization texture is not easily available as the magnetization varies on the microscopic scale in the considered compounds. In Ref. [32], it was therefore proposed to study the topological Hall effect in a two-dimensional electron gas (2DEG). In such a system an artificial magnetization texture can be introduced by the stray field of a lattice of ferromagnetic nanocylinders placed above the 2DEG. The advantage of such a setup is that all relevant parameters of the texture can be controlled to some extent by changing the nanocylinder lattice geometry, and that one can concentrate purely on the topological effect since spin-orbit scattering effects can be made small by choosing a semiconductor material with a small spin-orbit coupling constant for creating the 2DEG.

Theoretical studies of the topological Hall effect have mainly concentrated on the adiabatic regime, where the electron spin aligns perfectly with the local magnetization during its movement [32, 96, 97]. On the other hand, only very few papers have dealt with the nonadiabatic limit [98, 99], and even less is known about the transition between the two regimes. In this chapter therefore, we will study the topological Hall effect in the 2DEG systems mentioned above and we will try to improve our understanding of the effect in different regimes by means of numerical investigations.

The chapter is subdivided as follows. A short introduction to the Berry phase will be given first. This will aid in understanding the mechanism behind the topological Hall effect. Next, the topological Hall effect will be studied numerically in the adiabatic regime, making use of some simple models for the magnetization texture. Subsequently, a short discussion about adiabaticity criteria follows, in which a long-standing question about the relevant criterion in the diffusive transport regime is pointed out. An answer to this question will be formulated on the basis of numerical results dealing with the transition point between the nonadiabatic and adiabatic regime for different values of the mean free path in the sample.

7.2 Berry phase

7.2.1 Generalities

Although geometric phases in quantum physics are quite a young topic, a few textbooks have already appeared in which the origin and the mathematical description of such phases, together with their applications, have been discussed in detail [100, 101]. This proves the current high interest in the subject. In this section, only a brief account will be given on the Berry phase, discussing the main principles that are relevant for understanding the topological Hall effect in the next section. Parts of the discussion will proceed along the lines of what can be found in Refs. [95, 102–104].

We will start from a general "vector object" that is transported along a closed path on a curved surface, as depicted in Fig. 7.1. Even if the vector is not allowed to rotate around the normal to the surface at each point it passes (parallel transport), it will have been rotated over an angle Ω when returning to the starting position. The vector thus does not return to its initial state. This effect is of a purely geometrical/topological origin and is related to the intrinsic curvature of the surface on which the vector is transported. When moving the vector in a plane, or on the surface of a cylinder, no such phenomenon will occur.

In principle, quantum states are also described by vectors in a more abstract state space. Therefore they can "rotate" in a similar way when they are transported. The transport we have in mind now is not necessarily related to a physical motion. Rather, we are interested in how a particular eigenstate $|n[\mathbf{R}]\,\rangle$ evolves under influence of a Hamiltonian $H[\mathbf{R}]$ when some external parameters $\mathbf{R} = (R_1, R_2, \ldots)$ on which the Hamiltonian depends change in time: $\mathbf{R} = \mathbf{R}(t)$. In particular, we will ask how the final state $|n[\mathbf{R}(T)]\,\rangle$ differs from the initial state $|n[\mathbf{R}(0)]\,\rangle$ when the parameters in the Hamiltonian are carried adiabatically around some closed path $\mathcal{C} = \{\mathbf{R}(t)|t = 0 \to T, \mathbf{R}(T) = \mathbf{R}(0)\}$ in parameter space. To answer this question, one can proceed as follows.

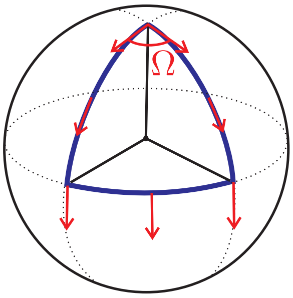

Figure 7.1: Parallel transport of a vector along a closed path on a sphere. When the vector arrives back at its starting position, it has undergone a rotation over an angle Ω.

For every set $\mathbf{R}$ of parameters, we can find the eigenstates $|n[\mathbf{R}]\,\rangle$ and their corresponding eigenvalues $E_n[\mathbf{R}]$ from the time-independent Schrödinger equation

$$H[\mathbf{R}]|n[\mathbf{R}]\,\rangle = E_n[\mathbf{R}]|n[\mathbf{R}]\,\rangle. \tag{7.1}$$

A first important point to note here is that this equation only defines the eigenvectors $|n[\mathbf{R}]\,\rangle$ up to a phase factor. We will assume that a particular choice of this phase has been made, only requiring that the ket $|n[\mathbf{R}]\,\rangle$ changes smoothly within the parameter range of interest, and that it is single valued for every $\mathbf{R}$.

Now suppose that the system initially starts in an eigenstate $|\psi(t=0)\,\rangle = |n[\mathbf{R}(t=0)]\,\rangle$. When the external parameters $\mathbf{R}(t)$ change sufficiently slow compared to typical orbital frequencies $\Delta E_n(t)$, the adiabatic theorem [105] states that the system will remain in the eigenstate $|n[\mathbf{R}(t)]\,\rangle$, picking up at most a time-dependent phase factor[3]. As such, we can write

$$\begin{aligned} |\psi(t)\,\rangle &= e^{\mathrm{i}\alpha(t)}\,|n[\mathbf{R}(t)]\,\rangle \\ &= e^{-\frac{\mathrm{i}}{\hbar}\int_0^t \mathrm{d}t' E_n(t')}\,e^{\mathrm{i}\gamma_n(t)}\,|n[\mathbf{R}(t)]\,\rangle, \end{aligned} \tag{7.2}$$

where in the second equation we have splitted off the usual dynamical phase factor which is a generalization of the phase picked up during the time evolution of an eigenstate evolving under a time-independent Hamiltonian. Inserting this in the Schrödinger equation (7.1), one finds for the phase $\gamma_n(t)$:

$$\frac{\mathrm{d}\gamma_n}{\mathrm{d}t}(t) = \mathrm{i}\langle\, n[\mathbf{R}(t)]\,|\,\mathrm{d}n[\mathbf{R}(t)]/\mathrm{d}t\,\rangle \tag{7.3a}$$

$$= \mathrm{i}\langle\, n[\mathbf{R}(t)]\,|\,\nabla_{\mathbf{R}} n[\mathbf{R}(t)]\,\rangle \cdot \frac{\mathrm{d}\mathbf{R}}{\mathrm{d}t}(t). \tag{7.3b}$$

All this, namely that the dynamical phase is accompanied by a phase $\gamma_n(t)$ that satisfies Eq. (7.3) was already known since the development of the adiabatic theorem, and there is thus nothing new about it. However, it was always assumed that a gauge transformation can be undertaken so as to redefine the phase of the basis vectors $|n[\mathbf{R}]\,\rangle$ (remember that this phase was not uniquely defined) in such a way that the phase factor $\gamma_n(t)$ would be eliminated. If this would be possible, this phase does not have any physical meaning as it would be gauge dependent.

It was Berry who realized that such a gauge transformation cannot be defined globally because $\gamma_n(t)$ will depend on the geometry of the path taken in parameter space, and $\gamma_n(t)$ at a certain time t will therefore be different for different paths [95]. Thus γ_n cannot be written as a function of $\mathbf{R}$ alone, and a gauge transformation of the form $|n[\mathbf{R}]\,\rangle \to e^{\mathrm{i}\gamma_n(\mathbf{R})}|n[\mathbf{R}]\,\rangle$ cannot be defined uniquely. In particular $\gamma_n(t)$ is not single valued under continuation around a circuit: if $\mathbf{R}$ evolves along a closed path so that $\mathbf{R}(T) = \mathbf{R}(0)$, then $\gamma_n(T)$ is not equal to $\gamma_n(0)$ and the difference will depend on the geometrical details of the path taken. The phase

---

[3] At least when $|n[\mathbf{R}]\,\rangle$ is nondegenerate for all $\mathbf{R}$, which we will assume here.

$\gamma_n(T)$ could thus in principle easily be observed by setting up an interference experiment between the states $|n[\mathbf{R}(t=0)]\,\rangle$ and $|n[\mathbf{R}(t=T)]\,\rangle$.

A possible "gedanken experiment" illustrating the statements above is the following [95]. A mono-energetic beam of electrons polarized along a magnetic field $\mathbf{B}$ is split at some point in two separate beams. One beam moves along a path where the magnetic field is kept constant, while the other beam will experience a field $\mathbf{B}(t)$ that slowly rotates around a cone. When the rotating field has returned to its original direction, the two beams are recombined to interfere. If the spin follows adiabatically the field direction, then according to the theory above, the second beam will pick up an extra phase γ_n compared to the first one. This phase difference γ_n can be modified by altering the geometry of the path that is followed by the magnetic field: in this example this could be realized by changing the angle θ of the cone. Doing so, the interference between both beams can be modulated between constructive and destructive, and the geometrical phase could in principle be visualized.

So it is the phase that is picked up when the external parameters describe a closed path that can be attributed a clear physical meaning and is called the Berry phase. This phase can be written as

$$\begin{aligned}
\gamma_n(T)-\gamma_n(0)=\gamma_n(\mathcal{C}) \quad &= \quad \int_0^T \mathrm{d}t\,\frac{\mathrm{d}\gamma_n}{\mathrm{d}t}(t) && \text{(7.4a)}\\
&= \quad \mathrm{i}\int_0^T \mathrm{d}t\,\frac{\mathrm{d}\mathbf{R}}{\mathrm{d}t}\cdot\langle\, n[\mathbf{R}(t)]\,|\,\nabla_{\mathbf{R}} n[\mathbf{R}(t)]\,\rangle && \text{(7.4b)}\\
&= \quad \mathrm{i}\oint \mathrm{d}\mathbf{R}\cdot\langle\, n[\mathbf{R}(t)]\,|\,\nabla_{\mathbf{R}} n[\mathbf{R}(t)]\,\rangle && \text{(7.4c)}
\end{aligned}$$

where the last integration is along the closed loop in parameter space. The physical significance of this phase can be made more clear by writing $\gamma_n(\mathcal{C})$ as

$$\begin{aligned}
\gamma_n(\mathcal{C}) \quad &= \quad \mathrm{i}\oint \mathrm{d}\mathbf{R}\cdot \mathrm{A}_n(\mathbf{R}) && \text{(7.5)}\\
&= \quad \iint_{S_\mathcal{C}} \mathrm{d}S\ \nabla\times\mathbf{A}_n(\mathbf{R}), && \text{(7.6)}
\end{aligned}$$

with the "vector potential"

$$\mathbf{A}_n(\mathbf{R}) = \mathrm{i}\langle\, n[\mathbf{R}]\,|\,\nabla_{\mathbf{R}} n[\mathbf{R}]\,\rangle. \tag{7.7}$$

In Eq. (7.6), Stokes theorem[4] has been used to write the path integral in terms of an integral over the surface $S_\mathcal{C}$ bounded by the path $\mathcal{C}$. Although the vector potential $\mathbf{A}_n(\mathbf{R})$ is not gauge invariant and therefore not an observable quantity, the Berry phase is. Indeed, consider a general gauge transformation $|n\,\rangle \rightarrow e^{\mathrm{i}\xi(\mathbf{R})}|n\,\rangle$

---

[4] Stokes theorem should be suitably generalized when the vector $\mathbf{R}$ is not three-dimensional. This is possible using the language of differential geometry [101].

changing the phases of the basis vectors. This will change $\mathbf{A}_n \to \mathbf{A}_n + \mathrm{i}\nabla\xi$, but since $\nabla\times\nabla\xi = 0$, the Berry phase $\gamma_n(\mathcal{C})$ stays invariant under such a transformation.

Looking back at Eqs. (7.4), the Berry phase depends only on the geometry of the closed path $\mathcal{C}$ that is traversed by $\mathbf{R}(t)$ in parameter space. It is therefore called a geometrical phase. On the other hand, the dynamical phase [see Eq. (7.2)] is dependent upon the rate at which the path in parameter space is completed, and thus gives us information about the time evolution of the system. Roughly speaking, the dynamical phase results from a local rotation of the state vector, while the Berry phase is analogous to a rotation due to parallel transport.

Several restrictions on the states $|n[\mathbf{R}]\,\rangle$ were made in deriving the Berry phase. Since the original paper by Berry, most of them have been loosened: e.g., degenerate basis states were treated in Ref. [106], while in Ref. [107] it was shown that even during a nonadiabatic evolution a geometrical phase will be picked up.

7.2.2 A simple example

The classic example illustrating Berry's phase is that of an electron at the origin subjected to a magnetic field $\mathbf{B}(t)$ of constant magnitude but changing direction, as depicted in Fig. 7.2.

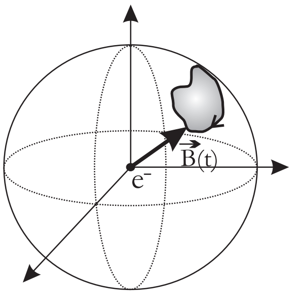

Figure 7.2: Electron in a time-dependent magnetic field. When the field describes a closed trajectory along the surface of a sphere, the electron will pick up a Berry phase.

The Hamiltonian for this problem is given by

$$H = -g\,\mathbf{B}(t)\cdot\boldsymbol{\sigma}, \tag{7.8}$$

with $\boldsymbol{\sigma}$ the vector of Pauli spin matrices, and g a coupling constant. In this case, the external parameters $\mathbf{R}(t)$ on which the Hamiltonian depends are the spherical angles describing the direction of the time-dependent field: $\mathbf{R}(t) = [\theta(t), \phi(t)]$.

The electron spin will follow the field direction adiabatically whenever

$$\omega_s/\omega \gg 1, \tag{7.9}$$

where $\omega_s = eB/m^*$ is the spin precession frequency, and ω is the rotation frequency of the magnetic field $\mathbf{B}(t)$[5]. The state of the electron is then given by the spin-up spinor with respect to $\mathbf{B}(t)$:

$$|n_+[\theta,\phi]\,\rangle = \begin{pmatrix} \cos\frac{\theta}{2}\, e^{-\mathrm{i}\phi} \\ \sin\frac{\theta}{2} \end{pmatrix}. \tag{7.10}$$

To calculate the Berry phase picked up when the magnetic field follows a closed path, we need the quantity $\nabla\times\langle\, n_+|\nabla n_+\,\rangle$. Expressing the gradient operator in spherical coordinates, we find

$$\nabla\times\langle\, n_+|\nabla n_+\,\rangle = \frac{\mathrm{i}}{2r^2}\mathbf{e}_r, \tag{7.11}$$

where r is the radial component of the magnetic field, and $\mathbf{e}_r$ is a unit vector in this direction. Using Eq. (7.4c), one finds for the Berry phase

$$\gamma_+(\mathcal{C}) = -\frac{1}{2}\int\frac{1}{r^2}\,\mathbf{e}_r\cdot\mathrm{d}\mathbf{S}. \tag{7.12}$$

The integral is over the area on the sphere swept out by $\mathbf{B}$ in the course of its closed path, so $\mathrm{d}\mathbf{S} = r^2\mathrm{d}\Omega\,\mathbf{e}_r$, and hence

$$\gamma_+(\mathcal{C}) = -\frac{1}{2}\int\mathrm{d}\Omega = -\frac{1}{2}\Omega. \tag{7.13}$$

So the net geometric phase picked up by the electron will be half of the solid angle Ω subtended by the path the magnetic field followed on the sphere. In the derivation, it was implicitly assumed that the magnetic field rotates clockwise. For a counterclockwise rotation, the Berry phase will just change its sign. The obtained result is very simple, but the physics behind it will in principle suffice for understanding the physical origin of the topological Hall effect.

7.3 Topological Hall effect

7.3.1 Theory

When an electron moves in a two-dimensional electron gas which is subjected to a spatially varying magnetization, it will follow the local magnetization direction adiabatically when the magnetization is strong enough. In its rest frame, the electron will thus see a time-dependent magnetic field and, as explained in the simple example above, will pick up a Berry phase that depends on the solid angle subtended by the magnetization direction as the electron follows its path. As we will see next, the effect of this Berry phase can be mapped onto that of an effective magnetic flux applied perpendicular to the sample. By means of this mapping, it is clear then that the spatially varying magnetization and its related Berry phase can induce a Hall effect, which was termed topological Hall effect [32] as it depends solely on the topology of the magnetization texture in the sample and does not rely explicitly on spin-orbit coupling nor on any real magnetic flux piercing through the sample.

---

[5] A derivation of this expression can be found in any textbook of quantum mechanics, e.g., in Ref. [105].

We will consider the following Hamiltonian:

$$H = -\frac{\hbar^2}{2m^*}\nabla^2 - g\,\mathbf{M}(\mathbf{r})\cdot\boldsymbol{\sigma}. \tag{7.14}$$

The first term describes the kinetic energy of the electron in the 2DEG (m^* is its effective mass), while the second is the exchange splitting induced by a spatially varying magnetization $\mathbf{M}(\mathbf{r})$. We will assume the magnitude M of the magnetization to be constant, while its direction is position dependent: $\mathbf{M}(\mathbf{r}) = M\mathbf{n}(\mathbf{r})$, with $\mathbf{n}(\mathbf{r})$ a unit vector in the magnetization direction. For our numerical purposes, we need the tight-binding equivalent of this Hamiltonian (see Chap. 3):

$$\mathcal{H} = -t\sum_{\langle ij\rangle}\sum_{\alpha}|i\alpha\,\rangle\langle\, j\alpha| - gM\sum_{i}\sum_{\alpha,\beta}|i\alpha\,\rangle\,\boldsymbol{\sigma}_{\alpha\beta}\cdot\mathbf{n}_i\,\langle\, i\beta|, \tag{7.15}$$

where i, j label the lattice sites, α, β are spin indices, t is the hopping amplitude between neighboring sites, and $\mathbf{n}_i = \mathbf{n}(\mathbf{r}_i)$. We can define a basis set $\{|i,\pm\,\rangle\}$ of states at site i with their spin parallel (+) or antiparallel (-) with respect to the magnetization direction at that site:

$$|i,+\,\rangle = \begin{pmatrix} \cos\frac{\theta_i}{2}\, e^{-\mathrm{i}\phi_i} \\ \sin\frac{\theta_i}{2} \end{pmatrix}; \quad |i,-\,\rangle = \begin{pmatrix} -\sin\frac{\theta_i}{2} \\ \cos\frac{\theta_i}{2}\, e^{\mathrm{i}\phi_i} \end{pmatrix}, \tag{7.16}$$

where (θ_i, ϕ_i) are the spherical angles of the local magnetization direction $\mathbf{n}_i$. Defining the operators

$$\mathcal{P}_\pm = \sum_i |i,\pm\,\rangle\langle\, i,\pm|, \tag{7.17}$$

which project on the subspace spanned by the spin-up (-down) states, and using $\mathcal{P}_+ + \mathcal{P}_- = 1$, one can write

$$\mathcal{H} = \Big(\mathcal{P}_+ + \mathcal{P}_-\Big)\,\mathcal{H}\,\Big(\mathcal{P}_+ + \mathcal{P}_-\Big) \tag{7.18}$$

$$= \mathcal{P}_+\mathcal{H}\mathcal{P}_+ + \mathcal{P}_-\mathcal{H}\mathcal{P}_+ + \mathcal{P}_+\mathcal{H}\mathcal{P}_- + \mathcal{P}_-\mathcal{H}\mathcal{P}_-. \tag{7.19}$$

When the exchange splitting $\Delta = 2gM$ is large enough, the spin-up state with respect to the local magnetization direction will be energetically so favorable that spin-flip transitions will be absent. In this adiabatic regime, the electron spin will thus follow exactly the local magnetization direction as the electron moves through the 2DEG, so that we can confine ourselves to the subspace spanned by spin-up states and neglect all other terms in Eq. (7.19). Doing so, one finds an effective Hamiltonian governing the dynamics in the perfectly adiabatic regime [96, 108] (see Appendix F for a detailed derivation):

$$\mathcal{H}^{\text{eff}} = \mathcal{P}_+\mathcal{H}\mathcal{P}_+ = -\sum_{\langle i,j\rangle} t^{\text{eff}}_{ij}|i,+\,\rangle\langle\, j,+| - gM, \tag{7.20}$$

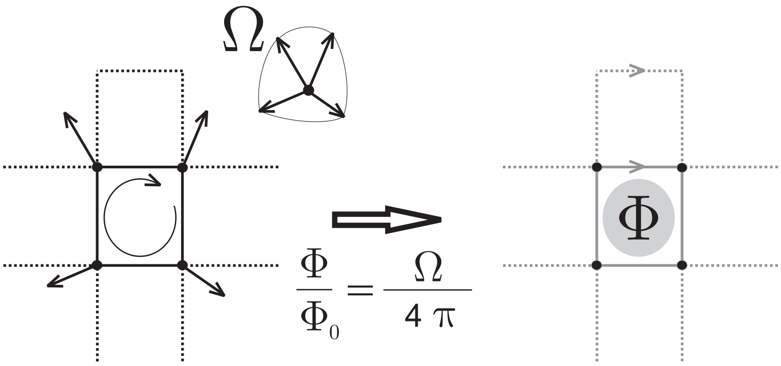

Figure 7.3: Mapping of an electron moving in a magnetic texture to a spinless electron moving around a flux tube distribution. The gray color of the vertices on the right picture stand for a change in hopping amplitude, while the arrows denote a change in hopping phase at the respective vertices.

with

$$t_{ij}^{\text{eff}} = t\cos\frac{\theta_{ij}}{2}\, e^{\mathrm{i}\gamma_{ij}}. \tag{7.21}$$

As such, we have mapped the original problem to a free electron like tight-binding Hamiltonian, with renormalized hopping parameters between nearest neighbors. The magnitude of the hopping parameter is decreased depending on the angle θ_{ij} between the magnetization direction at sites i and j. But more importantly for us, a phase factor $e^{\mathrm{i}\gamma_{ij}}$ is picked up, which describes the effect of the Berry phase. Let's see how this can be understood.

Suppose an electron makes a closed trajectory around a lattice cell as depicted in Fig. 7.3. Since its spin follows adiabatically the local magnetization direction, the electron will pick up a Berry phase that is equal to half the solid angle Ω subtended by the magnetization directions at the four corners of the cell. On the other hand, when a magnetic flux $\Phi = Ba^2$ would pierce through the same lattice cell, an electron moving around it would acquire a phase $2\pi\Phi/\Phi_0$ ($\Phi_0 = h/e$ is the magnetic flux quantum). So in principle, the effect of the Berry phase picked up around a lattice cell is equivalent to that of a magnetic flux $\Phi/\Phi_0 = \Omega/4\pi$ piercing through this cell.

This analogy becomes more clear when looking back at the Peierls method we used for describing such a flux tube: the hopping parameters in the complete lattice were changed as

$$t_{ij} \to t\, e^{-\mathrm{i}e/\hbar\int_i^j \mathbf{A}\cdot\mathrm{d}\mathbf{l}}, \tag{7.22}$$

in which $\mathbf{A}$ describes the vector potential generated by the flux tube. Comparing with Eq. (7.21), we see that the γ_{ij} can be generated by the same vector potential $\mathbf{A}$ describing flux tubes with values of $\Phi/\Phi_0 = \Omega/(4\pi)$ piercing through the lattice cells:

$$\gamma_{ij} = -e/\hbar \int_i^j \mathbf{A} \cdot \mathrm{d}\mathbf{l}. \tag{7.23}$$

So for expressing the γ_{ij}, one can proceed as follows. One calculates the solid angle subtended by the magnetization directions at the corners of every single lattice cell, and translates this into a flux tube distribution with fluxes $\Phi/\Phi_0 = \Omega/(4\pi)$. Subsequently, one describes this flux tube arrangement in terms of a vector potential $\mathbf{A}$, and calculates the phases γ_{ij} with Eq. (7.23). As such, the γ_{ij} are uniquely defined once we have made a choice of gauge for the vector potential $\mathbf{A}$ describing the flux tubes. For example, for describing the effect of a single flux tube, one could make a choice of gauge for $\mathbf{A}$ such that the hopping phase on all the vertices above the flux tube change as $t \rightarrow t \exp(\mathrm{i}2\pi\Phi/\Phi_0) = t \exp(\mathrm{i}\Omega/2)$ (see Fig. 7.3). This would correspond to the same gauge we used in Sec. 3.1.2 for describing inhomogeneous magnetic fields.

In summary, the Hamiltonian for an electron moving in a magnetization texture can be mapped onto a Hamiltonian of spinless electrons moving in an inhomogeneous magnetic flux distribution. The former will be referred to as the magnetization model, while the latter will be called the flux model. In the flux model, the value of the effective magnetic flux through a lattice cell is given by $\Phi/\Phi_0 = \frac{\Omega}{4\pi}$, where Ω is the solid angle subtended by the magnetization directions at the four corners of the lattice cell. Also, the magnitude of the hopping parameters depends on the angle between the magnetization directions. By means of this mapping it should be clear now that the magnetization texture can indeed give rise to a Hall effect. Since the effective flux is given by a solid angle, it is obvious that the topological Hall effect can be nonzero only for noncoplanar textures.

7.3.2 A first example

The existence of the topological Hall effect will now be illustrated with a few model calculations in a four-terminal geometry as depicted in Fig. 7.4. The quantity under

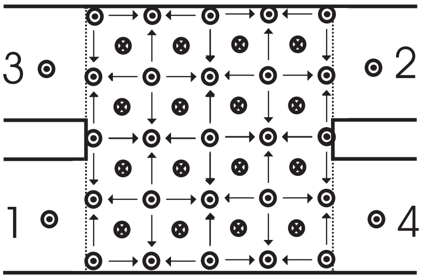

Figure 7.4: Four-terminal setup for calculating the Hall resistance R_H. A magnetization texture is fitted in the central device, while in the leads, the magnetization is pointing out of the plane of the paper.

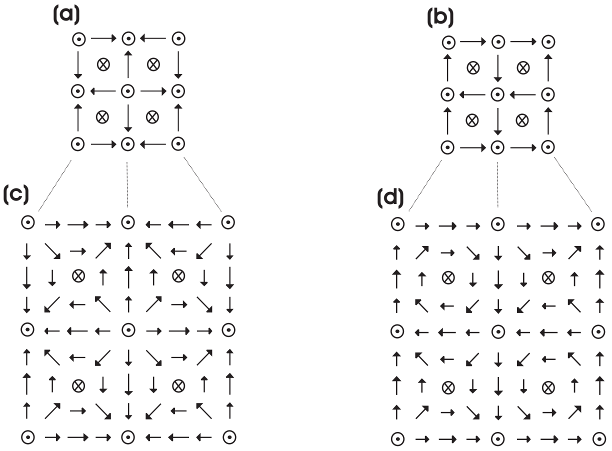

Figure 7.5: Basic unit cells for the magnetization texture used in the numerical calculations. The magnetization direction at every site is indicated by an arrow. Magnetization is projected onto the plane of the paper: a longer arrow stands for a longer projection. The textures in (a,c) have a nonzero net chirality and give therefore rise to a topological Hall effect. The textures in (b,d) only differ slightly from (a,c), but they have a zero net chirality and give no topological Hall effect at all. The larger unit cells (c,d) are obtained by scaling up the smaller ones.

consideration is the Hall resistance R_H as it was defined in the preceding chapter [see the discussion around Eq. (6.11)]: $R_H = 1/2\,(R_{12,34} - R_{34,12})$. To stress the importance of topology in the observed Hall effect, results will be shown for two magnetization textures that are at first sight similarly looking, but which will give completely different results. Some details about these magnetization textures will now be given first.

We start from the magnetization textures shown in Figs. 7.5(a)/(b). The magnetization has constant magnitude, but changes its direction according to the arrows drawn on every lattice site. In Fig. 7.5(a), the solid angle subtended by the magnetization directions is equal to $\Omega = +\pi$ for every single lattice cell, while in Fig. 7.5(b) it is $\Omega = +\pi$ for one half of the lattice cells and $\Omega = -\pi$ for the other half [the sign of the solid angle depends on the rotation direction of the field: it is positive (negative) for a counterclockwise (clockwise) rotation]. Translating this into the flux model, we would have corresponding fluxes of $\Phi/\Phi_0 = \pm 1/4$ through single lattice cells. In Fig. 7.5(a), all fluxes have the same sign and would add up to a net total flux of $4\Phi_0$ through the complete magnetization texture. On the other hand, the opposite fluxes in Fig. 7.5(b) would cancel each other exactly and give a net flux of zero. One says that the structure of Fig. 7.5(a) has a nonzero chirality, while in Fig. 7.5(b) the chirality is zero. In the first case, one would expect a net Hall effect, while the second one gives no Hall effect at all. By this simple reasoning, it is clear that the topology of the magnetization texture is of prime importance.

We can scale up the magnetization textures of Figs. 7.5(a)/(b) by introducing extra lattice sites in between the original sites, and by interpolating the direction of the magnetization at these new sites between those of the original ones. For example, scaling up the magnetization textures in Figs. 7.5(a)/(b) once, one finds the textures depicted in Figs. 7.5(c)/(d). Since the magnetization now varies more slowly from site to site, the solid angle subtended by a single cell of the lattice, and thus the corresponding effective flux piercing through, is smaller. The upscaling procedure can be repeated a number of times: every time we scale up the cell, it will comprise four times the original number of sites, so that the average flux per lattice cell will be decreased by a factor of four. It should be noted that although the effective flux per lattice cell for the original magnetization texture is homogeneously distributed (exactly $\Phi_0/4$ per lattice cell), this is not longer the case for the textures found by scaling up the first one.

The calculations in this section will be done with a 16×16 cell found by scaling up the magnetic textures in Figs. 7.5(a)/(b) two times. We will consider a square geometry as in Fig. 7.4 consisting of 65×65 sites, in which 16 such magnetization cells are fitted. The four attached leads have a width of 30 sites, and the magnetic field in these leads is completely fixed, pointing out of the plane of the paper. Results for the Hall resistance R_H as a function of the energy above the bottom of the spin-up subband are shown in Fig. 7.6. The exchange splitting was chosen to be $\Delta = 2gM = 100t$ in order to make sure we are in the adiabatic regime (see also next section). When the magnetization cell with nonzero chirality [derived from Fig. 7.5(a)] is used, a nonzero R_H is clearly observed in Fig. 7.6. In fact, one can clearly see the integer quantum Hall effect with its well-defined plateaus at $R_H = h/(e^2 n)$ for integer n [33]. This regime could be expected: mapping the

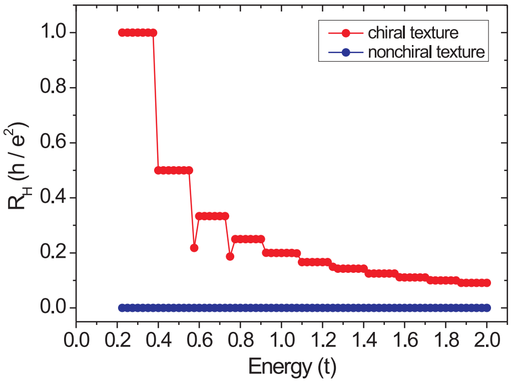

Figure 7.6: Hall resistance as a function of energy above the bottom of the spin-up subband. Only the chiral magnetization texture gives a nonzero Hall effect.

magnetization texture onto flux tubes would give an average flux of $\Phi/\Phi_0 = 1/64$ per lattice cell, leading to a cyclotron radius $r_C = 10a$ (for $E_F = t$) which is smaller than the system size. On the other hand, for the magnetization distribution derived from Fig. 7.5(b), no Hall effect is observed in Fig. 7.6 as expected.

When we did the mapping onto the flux model, we found perfect overlapping with the magnetization model results presented in Fig. 7.6. It can be claimed that this perfect overlap does not come as a surprise because in the quantum Hall regime the Hall resistance is quantized into exact plateaus. However, by using magnetization textures that are scaled up more than two times one can reduce the effective magnetic fluxes to values outside the quantum Hall regime. Even in such calculations, the overlap between the magnetization and the flux model was found to be always exact within our numerical accuracy. Nevertheless, the main point is that a Hall effect can be observed that is due to the electron adiabatically following a certain magnetization structure, and which does not invoke any real magnetic flux nor any form of spin-orbit coupling. This point is clearly demonstrated by the results in Fig. 7.6.

7.4 Transition between nonadiabatic and adiabatic regime

7.4.1 Adiabaticity criteria

For the topological Hall effect to appear, the electron spin should follow adiabatically the local magnetization direction. It is intuitively clear that this happens when the exchange splitting is large enough, in which case spin-flip transitions are energetically unfavorable. In this section, we will quantify what is meant with “large enough”.

For an electron placed at rest in a time dependent magnetic field, as in Sec. 7.2.2, the adiabaticity criterion yields $\omega_s/\omega \gg 1$, with ω_s the spin precession frequency and ω the rotation frequency of the magnetic field. For the topological Hall effect, it is the electron that moves through a spatially varying magnetic structure, so the rotation frequency ω should be replaced by the inverse of a time scale τ that quantifies how fast the electron “sees” the magnetization change upon its movement through the structure. When no disorder is present in the system, it is clear that this time scale τ is given by $\tau = \xi/v_F$, with v_F the Fermi velocity of the electron, and ξ a characteristic distance over which the magnetization changes its direction substantially (e.g., by an angle π). The adiabaticity criterion in the ballistic regime thus yields

$$Q = \frac{\omega_s \xi}{v_F} \gg 1. \tag{7.24}$$

When introducing disorder in the system, it is clear that this criterion is still valid as long as the mean free path l_m is larger than ξ. However, when going to the strongly diffusive regime $l_m < \xi$, two different time scales τ appear in the literature and there is still a discussion going on about the relevant one [109–113]. Intuitively, one might expect that the relevant time scale would now be the time the electron needs to diffuse over a distance ξ, i.e., the Thouless time $\tau_{\text{th}} = (\xi/l_m)^2\,\tau_m$. This was put forward by Loss and coworkers [109, 110], and leads to the criterion

$$Q \gg \frac{l_m}{\xi}. \tag{7.25}$$

Since $l_m/\xi < 1$ in the diffusive regime, this criterion tells us that adiabaticity is reached faster in a strongly disordered system compared to the ballistic one, and it is therefore referred to as the "optimistic criterion" in the literature. On the other hand, analytical calculations by Stern [111] have found that the relevant time scale is the elastic scattering time $\tau = \tau_m$, leading to a more pessimistic criterion

$$Q \gg \frac{\xi}{l_m}. \tag{7.26}$$

These criteria were derived while studying Berry phase interference effects in (ring) structures that are subjected to a spatially varying magnetic field. The pessimistic criterion predicts the need for experimentally unrealizable large magnetic fields to observe such effects, while the optimistic criterion would allow for such an experiment given a sufficiently disordered system. Unfortunately, in a paper of van Langen *et al.* the pessimistic criterion was confirmed by a semiclassical analysis [112], and later numerically by Popp *et al.* [113]. In subsequent sections, we will have a closer look at the transition point between the adiabatic and nonadiabatic regimes for our problem of the topological Hall effect, and try to shed some more light on the discussion.

7.4.2 Calculation of the Hall resistivity

To resolve the issue of finding the correct adiabaticity criterion in the diffusive regime, one could think of calculating the Hall resistance R_H as a function of the adiabaticity parameter Q and compare the rate at which the adiabatic regime is reached for samples with different mean free paths. However, the Landauer-Büttiker formalism we use for calculating R_H describes a phase coherent (mesoscopic) system, and all properties of such system are heavily dependent upon the exact placement of impurities throughout the system. This means that the Hall resistance R_H will be different for different disorder configurations, even when they are characterized by the same mean free path. Although such resistance fluctuations are an integral part of the physics of mesoscopic systems [6], they make a quantitative comparison of R_H between samples with different mean free paths useless: the results will depend on the particular choice of disorder configuration in every sample.

We would like to compare properties of a macroscopic system, i.e., a system with a finite phase coherence length in which such fluctuations are absent. For doing so, one can introduce some kind of (phase) averaging over different disorder configurations to find a description of the transport properties in terms of a macroscopic material constant, like the Hall resistivity. Some care should be taken in defining such an averaging procedure: e.g., just calculating the mathematical average $R_H = \frac{1}{N}\sum_{i=1}^{N} R_H^i$ of the Hall resistances R_H^i found for N different impurity configurations does not give a quantity that is directly related to the Hall resistivity ρ_H of a macroscopic system. We have developed an averaging procedure based on the idea that a macroscopic system ($L \gg L_\phi$) can be thought to consist of smaller phase coherent sections of size $L \approx L_\phi$. For every smaller section, we can use the Landauer-Büttiker formalism to derive its transport properties, and the properties of a macroscopic system can then be found by attaching such sections in an incoherent way. Since a more detailed discussion on our particular averaging procedure and the corresponding Hall resistivity ρ_H is rather technical, it is given in Appendix G at the end of this thesis.

7.4.3 Results

In this section, plots for the Hall resistivity ρ_H will be shown as a function of the adiabaticity parameter $Q = \omega_s \xi / v_F$ for different values of the mean free path: Q can be changed by tuning the exchange splitting Δ, since $\hbar\omega_s = \Delta$. This will allow us to determine whether the adiabatic regime is reached faster or slower as the mean free path is decreased, and thus whether the optimistic [Eq. (7.26)] respectively the pessimistic criterion [Eq. (7.25)] is the correct one.

The starting point for obtaining ρ_H with the procedure described in Appendix G is the structure that was shown in Fig. 7.4: a square region of 65×65 sites is connected to leads with a width of 30 sites. The magnetization texture in the square region is now obtained by scaling up the unit cell in Fig. 7.5(a) three times, giving us a magnetization structure of 64×64 sites. For this particular texture, the shortest distance over which the magnetization rotates by an angle π is $\xi \approx 22$ sites. The magnetization now varies slowly enough so that the effective magnetic flux the electrons see when hopping through the lattice lies far outside the quantum Hall regime. In the leads, the magnetization is chosen to be perpendicular to the plane of the leads (pointing out of the plane of the paper), and is kept constant throughout.

For a given mean free path, 500 different impurity configurations are then generated. Subsequently, 4900 structures as in Fig. 7.4, with impurity configurations chosen randomly from these 500, are wired together in a 70×70 array using the wiring scheme in Fig. G.2 of Appendix G, and the Hall resistivity ρ_H is calculated with the averaging procedure described there. It was made sure that the calculated value of ρ_H converged in the sense that it does not change by either choosing more than 500 impurity configurations, nor by attaching more than 4900 sections.

Results for the quasiballistic regime $l_m > \xi$ are shown in Fig. 7.7. For both mean free paths $l_m = 64a$ and $l_m = 32a$ the adiabatic limit is reached simultaneously for a value of $Q \approx 20$: from this point on, the resistivity stays constant upon increasing Q further. This is in good agreement with the criterion $Q \gg 1$ expected in this regime of parameters [Eq. (7.24)]. It can further be seen that the adiabatic value of $\rho_H \approx 5 \times 10^{-3}\hbar/e^2$ is practically independent of the mean free path. We furthermore checked numerically that this value is the same as the one that would

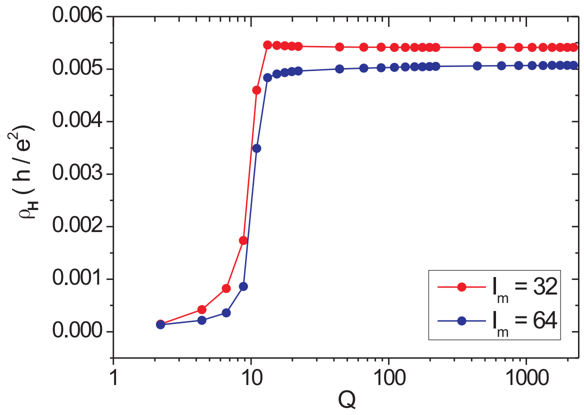

Figure 7.7: Hall resistivity as a function of the adiabaticity parameter Q for mean free path values $l_m > \xi$. The adiabatic limit is reached when $Q \gg 1$.

be obtained by mapping the magnetization model to the effective magnetic flux model (defined in Sec. 7.3.1).

In the nonadiabatic limit, the Hall resistivity does not increase smoothly with increasing the exchange splitting. Rather, ρ_H stays almost zero for small Q and an abrupt transition takes place around $Q \approx 20$ which corresponds to the exchange splitting Δ equaling the Fermi energy ($E_F = 1t$ above the bottom of the spin-up subband in our calculations). So the adiabatic limit is reached on a short scale as soon as the spin-down subband lies above the Fermi energy.

The diffusive regime ($l_m < \xi$) is studied in Fig. 7.8(a). Generally speaking, the same behavior as before can be observed: an abrupt transition takes place around $Q \approx 20$ after which the Hall resistivity takes again the same value of $\rho_H \approx 5 \times 10^{-3}\hbar/e^2$ independent of the mean free path. However, looking closer at the transition point, one can clearly see that the adiabatic limit is reached more slowly for the mean free path $l_m = 9a$: ρ_H first overshoots its adiabatic value, and then slowly converges to it. This difference is made clear in Fig. 7.8(b), where we plotted the difference between the Hall resistivity ρ_H and the adiabatic value it reaches (so that all curves converge to 0), for mean free paths $l_m = 9a, 12a,$ and$16a$. In this figure, there is a clear tendency of slower convergence upon decreasing the mean free path. This speaks in favor of the pessimistic adiabaticity criterion. Although for our limited range of parameters the two adiabaticity criteria do not differ very much quantitatively, namely $Q \gg 0.45$ versus $Q \gg 2$ for $l_m = 9a$, the optimistic criterion would predict the opposite behavior.

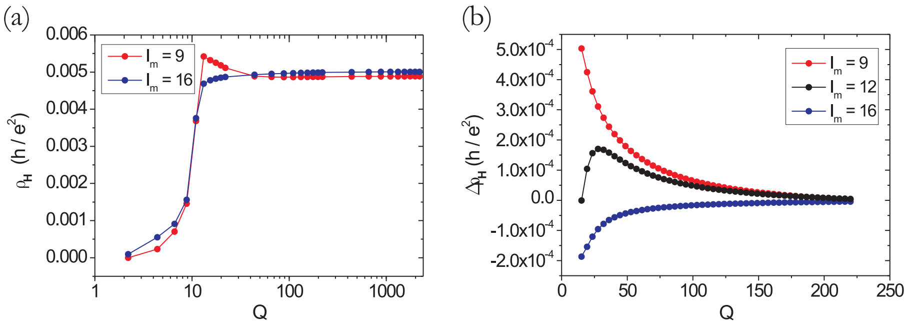

Figure 7.8: Hall resistivity as a function of the adiabaticity parameter Q for values of the mean free path in the diffusive regime. In (b) the region $20 < Q < 250$ is zoomed in upon. The curves in this plot are shifted so they all converge to zero: $\Delta\rho_H(Q) = \rho_H(Q) - \rho_H(Q \to \infty)$.

7.5 Conclusions

In this chapter, we have shown numerical calculations confirming the existence of a fully topological Hall effect, that is due to the Berry phase an electron picks up when moving adiabatically in a noncoplanar magnetization texture. In the adiabatic regime, the governing Hamiltonian can be mapped onto a model of spinless electrons moving in a magnetic flux. Both models indeed give the same numerical results for the Hall resistance/resistivity. A closer look at the transition point between the nonadiabatic and adiabatic regime revealed a rather abrupt transition upon increasing the exchange splitting. The transition takes place around the point where the spin-down subband becomes depopulated. Furthermore, we were able to find confirmation for the pessimistic adiabaticity criterion in Ref. [111] by looking at the transition point for different mean free paths in the strongly diffusive regime. In this regime, a special method for phase averaging was introduced for getting rid of conductance fluctuations, which enabled us to describe the transport properties of a large system ($L > L_\phi$) in terms of a Hall resistivity.

Chapter 8

Conclusions

The study of mesoscopic systems, although it is still a relatively young topic, has already evolved into a major branch of condensed matter physics. It is both the sheer interest in the amazing quantum properties of such systems, and the prospect of future technological applications, that has nucleated a large amount of theoretical and experimental research. In this thesis, we have tried to contribute to this fast growing field by developing and implementing a numerical approach in order to model transport in two-dimensional mesoscopic devices in general. Within our numerical framework, we are able to describe different system geometries, include multiple leads connected to the sample, and take into account the influence of magnetic fields. Moreover, we can include the electronic spin degrees of freedom, i.e., we can describe correctly the influence of exchange fields and spin-orbit interactions. Furthermore, by extending existing numerical techniques, we were able to obtain a very efficient method that gives access to a wealth of physical transport quantities. As such, we have a general purpose tool at our hand that can be used to attack a wide variety of mesoscopic transport questions.

As a first application, the numerical code has shown its capabilities by aiding in the interpretation of a recent series of scanning probe experiments, in which the conductance decrease of a sample as a function of the position of the perturbing tip can give local information about the coherent flow of electrons through the sample. We have been able to simulate such experiments in a very efficient way, and obtained a striking agreement with the experimental flow maps. In particular, the division of the flow in several branches after leaving a narrow constriction (essentially a disorder effect) could be reproduced, as well as an interference effect due to scattering between tip and constriction. By comparing the obtained simulation images with a plot of the calculated current density in the sample, we have been able to show that the experiment indeed probes the current flow through the system. In order to image electron flow in the presence of high magnetic fields, a different scanning probe setup had to be proposed, which allowed cyclotron orbits of the electrons to be visualized clearly. The new flow maps gave a different view on electron transport through the sample, as evidenced by the asymmetry of the images with respect to magnetic field reversal, contrary to the symmetric picture obtained with the original method. At the end of the chapter, quantum coherence of the electron flow through a 2DEG has been beautifully illustrated by the observation of interference fringes at crossings between coherent electron beams, an effect that has not yet been observed experimentally.

In a subsequent chapter, we have seen how our numerical method allows for modeling inelastic scattering events in a mesoscopic sample. This was done by attaching extra artificial leads to the sample, where each lead effectively models a single inelastic scattering center. Although this phenomenological model was already known for some time, it was not very satisfying from a practical point of view. However, we have shown that a perturbation approach to the original proposal allows for an efficient implementation within our numerical framework. This implementation was tested on a ring system, in which a special interference based Hall effect was seen to disappear with increasing the inelastic scattering strength.

In the last chapter, we have studied the motion of electrons in a noncoplanar magnetic texture. When the electron spin follows adiabatically the local magnetization direction while moving through the sample, the Berry phase picked up by the electron leads to a Hall effect, even in the absence of a net magnetic flux or any form of spin-orbit coupling. We have investigated this so-called topological Hall effect in a few simple magnetization textures. In the adiabatic regime, the governing Hamiltonian can be mapped onto a model of spinless electrons moving in a magnetic flux. Numerical evaluation of both models indeed gave the same numerical results for the Hall resistance/resistivity. Furthermore, a detailed study of the transition point between the nonadiabatic and adiabatic regimes made it clear that the criterion to reach adiabaticity is more stringent as the disorder in the system increases.

As one can see, we were able to tackle quite distinct problems. This general applicability of our method opens up the way for several new projects in the future. For example, we did not yet make use of the possibility to introduce spin-orbit coupling in our calculations. One interesting topic in this respect is the spin Hall effect [25–27], which states that a longitudinal unpolarized current can give rise to a transverse pure spin current in the presence of spin-orbit coupling. This topic is quite controversial nowadays, and several questions remain to be answered [114]. For example, since spin is not a conserved quantity when spin-orbit coupling is present, a spin current cannot be defined on the basis of a normal continuity equation, and the definition of spin current itself is therefore under heavy debate [115, 116]. We could think of doing a scanning probe imaging experiment, measuring the change of Hall resistance when a magnetic tip is scanned over the surface. This conductance change is well defined, and the obtained flow map might lead to some insight into the understanding of spin currents.

On the other hand, the topological Hall effect should be studied in more detail in the nonadiabatic regime, in order to check that the Hall resistance increases proportional to the third power of the spin splitting, something that was obtained within perturbation theory recently [98]. Similarly, one might check what the influence of inelastic scattering is on the adiabaticity criterion. Maybe this can lead to a more optimistic criterion, so that the fully adiabatic regime might be easier to reach in an experiment than believed up to now. In every case, the amount of information that can be obtained from calculations with our numerical method, and the variety of systems that can be studied with it look promising for the future.

Zusammenfassung

Die Phasenkohärenz der Ladungsträger ist verantwortlich für einzigartige Transporteigenschaften in mesoskopischen Systemen. Dies macht mesoskopische Systeme interessant für die Grundlagenforschung und gibt ihnen darüberhinaus eine mögliche Zukunft in nanoelektronischen Anwendungen.

In der vorliegenden Arbeit wird eine numerische Methode implementiert um die Eigenschaften zweidimensionaler mesoskopischer Systeme zu untersuchen. Diese Methode erlaubt die Berechnung vielfältiger Transporteigenschaften, einschließlich einer kompletten Beschreibung der Ladungs- und Spin-Freiheitsgrade. Sie erweist sich deshalb als wertvoll für die Untersuchungen in der mesoskopischen Physik. Dies wird anhand von drei unterschiedlichen Problemen veranschaulicht, auf die diese numerische Methode angewandt wird.

Erstens ermöglicht die Methode eine effiziente Simulation neuer Rastertunnelmikroskopieexperimente, in denen der kohärente Elektronenfluss durch eine zweidimensionale Probe sichtbar gemacht wird. Bei diesen Experimenten wird die Erhöhung des Probenwiderstandes in Abhängigkeit von der Spitzenposition gemessen. Passieren Elektronen eine schmale Engstelle, spaltet sich der Stromfluss in verschieden Äste auf - was auch eperimentell nachgewiesen wurde. Es wird der Einfluss eines Magnetfeldes auf diese Äste untersucht und die Formierung von Zyklotronumlaufbahnen an den Probenkanten visualisiert, jedoch nur nachdem ein neuer Messaufbau vorgeschlagen wurde. Darüberhinaus können vielfältige Interferenzphänomene beobachtet werden, die die kohärente Natur der Elektronen veranschaulichen.

Zweitens erlaubt das numerische Verfahren eine phänomenologische Modellierung phasenbrechender Streuzentren im System. Beispielhaft wird deren Einfluss auf die Transporteigenschaften eines Vierkontaktringes näher untersucht.

Drittens verursacht der Transport von Elektronen durch eine nicht-koplanare magnetische Textur einen Hall-Effekt, und dies sogar in Abwesenheit einer Netto-Lorentz-Kraft und ohne Berücksichtigung der Spin-Bahnkopplung. Dieser Hall-Effekt kann auf die Berry-Phase zurückgeführt werden, die von den Elektronen aufgenommen wird wenn ihre Spins der lokalen Magnetisierungsrichtung folgen. In dieser Arbeit wird mittels eines einfachen Modells der magnetischen Textur sowohl der adiabatische Grenzfall als auch sein nicht-adiabatisches Gegenstück behandelt, einschließlich des Effektes der Unordnung. Mit der Untersuchung des Übergangs zwischen beiden Regimen wird zu einer fortlaufenden Diskussion bezüglich des relevanten Adiabatizitätskriteriums im diffusiven Grenzfall Stellung genommen.

Part III

Appendix

Appendix A

Tight-binding model for the spin-orbit coupling Hamiltonian

In this Appendix, technical details can be found concerning the derivation of a tight-binding Hamiltonian describing spin-orbit coupling. We will discuss the spin-orbit Hamiltonian for an ideal two-dimensional system, as well as the Rashba spin-orbit Hamiltonian for electrons in a quantum well that are only effectively confined to move in a plane.

A.1 Strictly two-dimensional system

In a perfect 2D system, the electrostatic potential V an electron feels depends only on the coordinates (x, y) and the spin-orbit Hamiltonian was given by [c.f. Eq. (3.19)]

$$H_{\mathrm{SO}} = \lambda\,\sigma^z \left[\left(\frac{\hbar}{\mathrm{i}} \partial_x + eA^x \right) \partial_y V - \left(\frac{\hbar}{\mathrm{i}} \partial_y + eA^y \right) \partial_x V \right], \tag{A.1}$$

For deriving the tight-binding model, we will calculate the action of this Hamiltonian on a spinor wavefunction $\psi = (\psi_\uparrow, \psi_\downarrow)$ in a point (na, ma) of the tight-binding lattice. Since $A^y = 0$ in the gauge we defined in Sec. 3.1.2, we have only three terms to be considered in Eq. (A.1). In order to obtain the tight-binding model, the following approximations are made ($\psi_{nm} = \psi(na, ma)$):

$$\begin{aligned}
\left[\frac{\partial}{\partial x} \Big(\partial_y V\, \psi \Big) \right]_{n,m} &\approx \frac{1}{2a} \Big([\partial_y V]_{n \leftrightarrow n+1,m}\, \psi_{n+1,m} - [\partial_y V]_{n \leftrightarrow n-1,m}\, \psi_{n-1,m} \Big) \\
\left[\frac{\partial}{\partial y} \Big(\partial_x V\, \psi \Big) \right]_{n,m} &\approx \frac{1}{2a} \Big([\partial_x V]_{n,m \leftrightarrow m+1}\, \psi_{n,m+1} - [\partial_x V]_{n,m \leftrightarrow m-1}\, \psi_{n,m-1} \Big) \\
\Big[A^x\, \partial_y V\, \psi \Big]_{n,m} &\approx \frac{1}{2} \Big(A^x_{n \leftrightarrow n+1,m} [\partial_y V]_{n \leftrightarrow n+1,m}\, \psi_{n+1,m} + \\
&\qquad + A^x_{n \leftrightarrow n-1,m} [\partial_y V]_{n \leftrightarrow n-1,m}\, \psi_{n-1,m} \Big).
\end{aligned} \tag{A.2}$$

These equations need to be commented upon: in general, there are different ways of discretizing an operator, but one should make sure that the result in the end is physically reasonable. This means, e.g., that the obtained tight-binding Hamiltonian should be hermitian and should have the same symmetry properties as the original Hamiltonian. The equations above, although looking a bit arbitrary in the beginning, are chosen so as to satisfy such conditions. For example, to retain hermiticity it is necessary to evaluate the derivatives of the potential V on the vertices instead of the nodes in the first two equations [the vertex between (n,m) and $(n+1,m)$ is written as $(n \leftrightarrow n+1, m)$]. On the other hand, in Eq. (3.11) of Sec. 3.1.2 we have defined the vector potential A^x only on the vertices, so that the approximation in the last equation of Eqs. (A.2) is also necessary.

With these approximations, and using the gauge defined in Eq. (3.11) of Chap. 3, one finds for the action of the Hamiltonian $H_{\rm SO}$ in Eq. (A.1):

$$\begin{aligned}\langle\, n,m|H_{\rm SO}|\psi\,\rangle &= [H_{\rm SO}\psi]_{n,m}\\ &\approx -\frac{\mathrm{i}\lambda\hbar}{2a}\sigma^z\sum_{\pm}\Bigg\{[\partial_y V]_{n\leftrightarrow n\pm1,m}\Bigg(1\mp \mathrm{i}2\pi\sum_{l<m}\Phi_{n,l}/\Phi_0\Bigg)\psi_{n\pm1,m}-\\ &\qquad -[\partial_x V]_{n,m\leftrightarrow m\pm1}\,\psi_{n,m\pm1}\Bigg\}. \end{aligned}\tag{A.3}$$

When the fluxes through the different lattice cells are small, we can further approximate

$$\Bigg(1\pm \mathrm{i}\,2\pi\sum_{l<m}\Phi_{n,l}/\Phi_0\Bigg)\approx\exp\Bigg[\pm \mathrm{i}\,2\pi\sum_{l<m}\Phi_{n,l}/\Phi_0\Bigg].\tag{A.4}$$

Combining the equations (A.3) and (A.4), one can read off immediately the matrix elements of the tight-binding spin-orbit Hamiltonian by looking at the coefficients in front of the terms $\psi_{n'm'}$. One finds the following tight-binding representation:

$$\begin{aligned}\mathcal{H}_{\rm SO} &= \frac{\lambda\hbar}{2a}\sum_{n,m}\Bigg\{[\partial_x V]_{n,m\leftrightarrow m+1}\,\Big(|n,m\,\rangle\langle\, n,m+1|\otimes \mathrm{i}\sigma^z\Big) \\ &-[\partial_y V]_{n\leftrightarrow n+1,m}\,\exp\Bigg[-\mathrm{i}\,2\pi\sum_{l<m}\frac{\Phi_{n,l}}{\Phi_0}\Bigg]\,\Big(|n,m\,\rangle\langle\, n+1,m|\otimes \mathrm{i}\sigma^z\Big)+\text{H.c.}\Bigg\}.\end{aligned}\tag{A.5}$$

The derivatives of the potential on the vertices in this expression can be defined as

$$\begin{aligned}[]
[\partial_y V]_{n\leftrightarrow n+1,m} &\approx \frac{1}{2a}\left[\frac{1}{2}\Big(V_{n,m+1}+V_{n+1,m+1}\Big)-\frac{1}{2}\Big(V_{n,m-1}+V_{n+1,m-1}\Big)\right]\\
[\partial_x V]_{n,m\leftrightarrow m+1} &\approx \frac{1}{2a}\left[\frac{1}{2}\Big(V_{n+1,m}+V_{n+1,m+1}\Big)-\frac{1}{2}\Big(V_{n-1,m}+V_{n-1,m+1}\Big)\right]
\end{aligned}$$

It should be noted that by making the particular choice (A.2) it is made sure that if a vector potential is present, the phase an electron picks up when hopping is the same as the one obtained in Sec. 3.1.2, reassuring us that the Eqs. (A.2) are physically reasonable and consistent.

A.2 Rashba spin-orbit coupling

The Rashba Hamiltonian is given by [c.f. Eq. (3.22)]

$$H_{\text{RSO}} = \frac{\alpha}{\hbar}\left(P_y\sigma^x - P_x\sigma^y\right), \tag{A.6}$$

The tight-binding representation for this Hamiltonian is obtained by making the approximations

$$\begin{aligned} \left[\partial_x\psi\right]_{n,m} &= \frac{\psi_{n+1,m}-\psi_{n-1,m}}{2a} && \text{(A.7a)} \\ \left[\partial_y\psi\right]_{n,m} &= \frac{\psi_{n,m+1}-\psi_{n,m-1}}{2a}. && \text{(A.7b)} \end{aligned}$$

We then find

$$\begin{aligned} \langle\, n,m|H_{\text{RSO}}|\psi\,\rangle = &-\mathrm{i}\frac{\alpha}{2a}\left[\sigma^x\Big(\psi_{n,m+1}-\psi_{n,m-1}\Big)-\sigma^y\Big(\psi_{n+1,m}-\psi_{n-1,m}\Big)\right] \\ &-\frac{e\alpha}{\hbar}\,A^x_{nm}\,\sigma^y\,\psi_{n,m}. \end{aligned} \tag{A.8}$$

In this expression, we used that $A^y = 0$ in our gauge (defined in Sec. 3.1.2). The problem now arising again is that the vector potential A^x is defined on the vertices between the sites, and not on the nodes. We solve this by approximating

$$A^x_{nm}\psi_{n,m} \approx \frac{1}{2}\Big[A^x_{n\leftrightarrow n+1,m}\,\psi_{n+1,m} + A^x_{n-1\leftrightarrow n,m}\,\psi_{n-1,m}\Big]. \tag{A.9}$$

By now using Eq. (3.11) for the vectorpotential, and Eq. (A.4) , one obtains finally the tight-binding representation for the Rashba Hamiltonian:

$$\begin{aligned} \mathcal{H}_{\text{RSO}} = -t_{\text{SO}}\sum_{n,m}\Bigg\{ &\exp\Big[-\,\mathrm{i}2\pi\sum_{l<m}\Phi_{n,l}/\Phi_0\Big]\Big(|n,m\,\rangle\langle\, n+1,m|\otimes\mathrm{i}\sigma^y\Big) \\ &-\Big(|n,m\,\rangle\langle\, n,m+1|\otimes\mathrm{i}\sigma^x\Big)\;+\;\text{H.c.}\Bigg\} \end{aligned} \tag{A.10}$$

where we defined $t_{\text{SO}} = \alpha/2a$. By proceeding as in Eq. (A.9), it is made sure the phase an electron picks up when hopping is the same as the one obtained in Sec. 3.1.2, giving again a consistent result.

Appendix B

Surface Green's function of a semiinfinite lead

For the calculation of the self-energies of the semiinfinite leads, it is necessary to evaluate the surface Green's function of the isolated lead, i.e., the Green's function between points in the first column of the lead that attaches to the central device. The technique we are using for obtaining this Green's function was first derived in Ref. [51]. We will briefly explain this method now, following closely the discussion in Ref. [117].

Formally, the total retarded Green's function matrix g of an isolated lead is given by the inverse of the matrix:

$$g = \left[E + \mathrm{i}\eta - H_l\right]^{-1}, \tag{B.1}$$

where H_l is the Hamiltonian matrix of the lead. Since the leads connected to the sample in the Landauer-Büttiker formalism are considered to be perfect conductors, i.e., they are translationally invariant, the matrix representation of $E + \mathrm{i}\eta - H_l$ can be written in the following block tridiagonal form:

$$E + \mathrm{i}\eta - H_l = \begin{pmatrix} d & -A & 0 & 0 & \cdots \\ -B & D & -A & 0 & \cdots \\ 0 & -B & D & -A & \cdots \\ \vdots & 0 & -B & D & \ddots \\ & \vdots & \vdots & \ddots & \ddots \end{pmatrix}, \tag{B.2}$$

where d, D, A and B are all $2M \times 2M$ matrices (M is the width of the lead, while the factor 2 comes from spin). The matrix D represents a single isolated column of sites in the lead, while the matrices A and B describe the hopping between neighboring columns. The matrix d is equal to D, but it represents the column at the surface of the lead and is therefore given a separate notation.

By partitioning the total Green's function matrix G in a similar manner in $2M \times$

$2M$ submatrices, one can write Eq. (B.1) as follows:

$$\begin{pmatrix} d & -A & 0 & 0 & \cdots \\ -B & D & -A & 0 & \cdots \\ 0 & -B & D & -A & \cdots \\ \vdots & 0 & -B & D & \ddots \\ & \vdots & \vdots & \ddots & \ddots \end{pmatrix} \cdot \begin{pmatrix} g_{11} & g_{12} & g_{13} & \cdots & \\ g_{21} & g_{22} & g_{23} & g_{24} & \cdots \\ g_{31} & g_{32} & g_{33} & g_{34} & \cdots \\ \vdots & g_{42} & g_{43} & g_{44} & \cdots \\ & \vdots & \vdots & \vdots & \ddots \end{pmatrix} = 1. \quad \text{(B.3)}$$

The subdivision corresponds to the division of the lead in columns: g_{11} is the Green's function matrix between lattice sites of the first column of the lead, g_{12} connects lattice sites from the second to the first column, and so on (see Fig. 4.1 in Chap. 4). The surface Green's function that we are interested in is thus given by g_{11}.

By calculating the first column of the matrix product in Eq. (B.3), one obtains the following (infinite) set of equations for g_{11}:

$$d\,g_{11} = 1 + A\,g_{21}, \quad \text{(B.4a)}$$

$$D\,g_{p1} = B\,g_{p-1,1} + A\,g_{p+1,1}, \quad \forall p \geqslant 2. \quad \text{(B.4b)}$$

So, in order to calculate the surface Green's function g_{11}, one would need to know all matrices g_{p1} with $p \geqslant 2$. Now, by using Eq. (B.4b), one can express the Green's functions g_{p1} with even indices $p = 2r$ ($r = 1, 2, ...$), as a function of Green's functions with odd indices:

$$g_{2r,1} = D^{-1}B\,g_{2r-1,1} + D^{-1}A\,g_{2r+1,1} \quad \text{(B.5)}$$

Inserting this into Eqs. (B.4), one can obtain g_{11} as a function of only the g_{p1} with p odd:

$$\begin{aligned} \left(d - AD^{-1}B\right) g_{11} &= 1 + \left(AD^{-1}A\right) g_{31}, \\ \left(D - AD^{-1}B - BD^{-1}A\right) g_{2r+1,1} &= \left(BD^{-1}B\right) g_{2r-1,1} + \left(AD^{-1}A\right) g_{2r+3,1} \end{aligned}$$

Comparing these equations with Eqs. (B.4), one can see that they have exactly the same form if we define the renormalized matrices:

$$\begin{aligned} d' &= d - AD^{-1}B, \\ D' &= D - AD^{-1}B - BD^{-1}A, \\ A' &= AD^{-1}A, \\ B' &= BD^{-1}B, \\ g'_{r,1} &= g_{2r-1,1}, \quad r = 2, 3, \ldots . \end{aligned}$$

As such, we can iterate the previous procedure on the renormalized equations over and over again.

The physical meaning of this procedure is the following: originally, one looks at the lead as a stacking of layers, where each layer is originally composed of a single column. After the first iteration, the lead is seen as a stacking of layers composed of two columns, with renormalized interaction matrices A' and B' between neighboring layers. With each iteration, the number of columns from which a layer is composed of is doubled. After iteration n, one will find an equation of the following form for the surface Green's function:

$$d_n \, g_{11} = 1 + A_n \, g_{2^n+1,1}. \tag{B.8}$$

After a sufficiently large number n of iterations, the effective interaction A_n between the layers will become considerably small and the surface Green's function can be approximated by:

$$g_{11} \approx d_n^{-1}. \tag{B.9}$$

As such, one has an iterative procedure for calculating the surface Green's functions of the leads. Their self-energies can then be calculated with Eq. (4.13) of Chap. 4.

Appendix C

Derivation of the current density expressions

In this Appendix, expressions for the vertex currents of a tight-binding lattice in terms of Green's functions will be derived in detail. Such expressions were first given in Ref. [118] for a simple one-dimensional model. In Refs. [66, 67], this approach was generalized to two dimensions. Parts of the following derivation will therefore follow closely the discussions found in these references. Only the spin-degenerate case will be treated.

At certain stages, we will need to use some notions from the Keldysh formalism for nonequilibrium processes [76, 119]. Since a thorough introduction to this formalism would be out of the scope of this thesis, we will suffice by just "importing" the necessary equations and making them plausible with a small discussion. Full details of the Keldysh method can be found in some review papers, like Refs. [77–79] and in the book by Kadanoff and Baym [76].

C.1 Current operator

Consider a site (m, n) of the tight-binding lattice, as depicted in Fig. C.1. Since particle currents result from a difference in electrons flowing in opposite directions through the vertex, one expects the current operators to have the form (see Fig. C.1)

$$J_H \sim \sum_{\substack{p \geqslant n \\ q \leqslant n-1}} A_{pq}\, c_{pm}^\dagger c_{qm} - \sum_{\substack{p \leqslant n-1 \\ q \geqslant n}} A_{pq}\, c_{pm}^\dagger c_{qm}, \tag{C.1a}$$

$$J_{H'} \sim \sum_{\substack{p \geqslant n+1 \\ q \leqslant n}} B_{pq}\, c_{pm}^\dagger c_{qm} - \sum_{\substack{p \leqslant n \\ q \geqslant n+1}} B_{pq}\, c_{pm}^\dagger c_{qm}, \tag{C.1b}$$

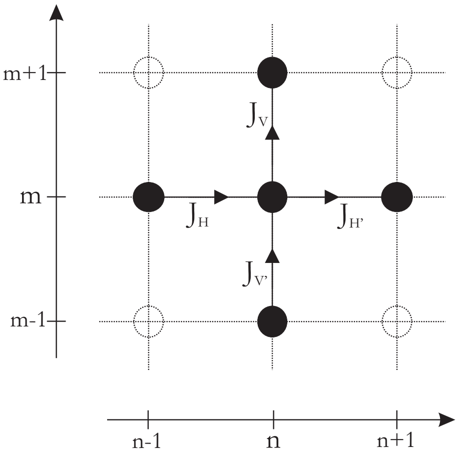

Figure C.1: Particle currents through the vertices of a tight-binding lattice.

$$J_V \sim \sum_{\substack{p\geqslant m+1\\ q\leqslant m}} C_{pq}\, c^\dagger_{np} c_{nq} - \sum_{\substack{p\leqslant m\\ q\geqslant m+1}} C_{pq}\, c^\dagger_{np} c_{nq}, \tag{C.2a}$$

$$J_{V'} \sim \sum_{\substack{p\geqslant m\\ q\leqslant m-1}} D_{pq}\, c^\dagger_{np} c_{nq} - \sum_{\substack{p\leqslant m-1\\ q\geqslant m}} D_{pq}\, c^\dagger_{np} c_{nq}, \tag{C.2b}$$

where the $c^\dagger_{nm}$ and c_{nm} are creation and annihilation operators for an electron at site (m, n). Expressions for the coefficients A_{pq}, B_{pq}, ... can be found through the continuity equation

$$J_H - J_{H'} + J_{V'} - J_V = \frac{\partial\, c^\dagger_{nm} c_{nm}}{\partial t} \tag{C.3}$$

with $c^\dagger_{nm} c_{nm}$ the operator counting the number of particles at site (m, n). Evaluating the time derivative by using the Liouville equation

$$\frac{\partial\, c^\dagger_{nm} c_{nm}}{\partial t} = \frac{1}{\mathrm{i}\hbar}\big[c^\dagger_{nm} c_{nm}, H\big], \tag{C.4}$$

where H is the tight-binding Hamiltonian of the system [Eq. (3.2) of Chap. 3], one obtains

$$\begin{aligned} \frac{\partial\, c^\dagger_{nm} c_{nm}}{\partial t} = \frac{1}{\mathrm{i}\hbar}\Big\{ & t^x_{n-1m}\, c^\dagger_{nm} c_{n-1m} - (t^x_{n-1m})^*\, c^\dagger_{n-1m} c_{nm} \\ & + (t^x_{nm})^*\, c^\dagger_{nm} c_{n+1m} - t^x_{nm}\, c^\dagger_{n+1m} c_{nm} \\ & + (t^y_{nm})^*\, c^\dagger_{nm} c_{nm+1} - t^y_{nm}\, c^\dagger_{nm+1} c_{nm} \\ & + t^y_{nm-1}\, c^\dagger_{nm} c_{nm-1} - (t^y_{nm-1})^*\, c^\dagger_{nm-1} c_{nm} \Big\}. \end{aligned} \tag{C.5}$$

Comparing with the Eqs. (C.1) and (C.2) one finds the following expressions for the particle current operators:

$$J_H = \frac{1}{\mathrm{i}\hbar}\left\{t^x_{n-1m}\, c^\dagger_{nm}c_{n-1m} - (t^x_{n-1m})^*\, c^\dagger_{n-1m}c_{nm}\right\} \tag{C.6a}$$

$$J_V = \frac{1}{\mathrm{i}\hbar}\left\{t^y_{nm}\, c^\dagger_{nm+1}c_{nm} - (t^y_{nm})^*\, c^\dagger_{nm}c_{nm+1}\right\}, \tag{C.6b}$$

and similar equations for $J_{H'}$ and $J_{V'}$.

C.2 Green's function expression for the currents

The vertex currents can now be calculated by evaluating the operator averages over the available states:

$$I_{(n-1,m)\to(n,m)} = -2e\big\langle J_H\big\rangle, \tag{C.7}$$

$$I_{(n,m)\to(n,m+1)} = -2e\big\langle J_V\big\rangle. \tag{C.8}$$

In these expressions we have multiplied with the electronic charge $-e$ to obtain a charge current (instead of the particle current). The factor 2 takes into account the spin degeneracy: we will only consider spin-degenerate systems from now on.

The connection with the Green's function formalism now arises because averages of the form $\langle c^\dagger_{nm}c_{n'm'}\rangle$ are related to the so-called "less-than" Green's function $G^<(t',t)$:

$$G^<_{n'm',nm}(t',t) = \frac{\mathrm{i}}{\hbar}\big\langle c^\dagger_{nm}(t)c_{n'm'}(t')\big\rangle. \tag{C.9}$$

This is a nonequilibrium Green's function, different from the retarded and advanced Green's functions defined in Chap. 4. More details about it can be found in one of the references on the Keldysh formalism given above. We will suffice here with the definition given in Eq. (C.9). In steady state, $G^<$ only depends on the difference $\tau = t - t'$, and one can Fourier transform $G^<$ into the energy domain. This gives a relation of the form

$$G^<_{n'm',nm}(\tau) = \frac{\mathrm{i}}{\hbar}\big\langle c^\dagger_{nm}(\tau)c_{n'm'}(0)\big\rangle = \frac{1}{2\pi\hbar}\int \mathrm{d}E\, G^<_{n'm',nm}(E)\; e^{-\mathrm{i}E\tau/\hbar}. \tag{C.10}$$

Since the creation and annihilation operators in Eqs. (C.6) act at the same instant in time (i.e., $\tau = 0$), one finds for the vertex currents

$$\begin{aligned} I_{(n-1,m)\to(n,m)} &= \frac{2e}{\hbar}\int\frac{\mathrm{d}E}{2\pi}\Big[t^x_{n-1m}\, G^<_{n-1m,nm} - (t^x_{n-1m})^*\, G^<_{nm,n-1m}\Big], \\ I_{(n,m)\to(n,m+1)} &= \frac{2e}{\hbar}\int\frac{\mathrm{d}E}{2\pi}\Big[t^y_{nm}\, G^<_{nm,nm+1} - (t^y_{nm})^*\, G^<_{nm+1,nm}\Big], \end{aligned}$$

with all Green's functions in this expression in the energy domain. From the definition (C.9), it is clear that $(G^<_{nm,n'm'})^* = -G^<_{n'm',nm}$, so that one can write

$$I_{(n-1,m)\to(n,m)} = \frac{-2e}{\hbar}\int\frac{\mathrm{d}E}{2\pi}2\,\mathrm{Re}\Big[(t^x_{n-1m})^*\,G^<_{nm,n-1m}\Big], \tag{C.11}$$

$$I_{(n,m)\to(n,m+1)} = \frac{-2e}{\hbar}\int\frac{\mathrm{d}E}{2\pi}2\,\mathrm{Re}\Big[(t^y_{nm})^* G^<_{nm+1,nm}\Big]. \tag{C.12}$$

In the following, we will see how these equations can be expressed in terms of the retarded and advanced Green's functions calculated in Chap. 4.

C.2.1 Longitudinal current

Consider a system as shown in Fig. C.2. We will use the same notation as in Chap. 4: O_{nn} is a submatrix of the operator O, with elements $\langle\, m|O_{nn'}|m'\,\rangle = \langle\, n,m|O|n',m'\,\rangle$. For example, the hopping matrix $V_{n,n-1}$ describes hopping from column $n-1$ to column n, and has elements $\langle\, m|V_{n,n-1}|m'\,\rangle = t^x_{n-1m}\delta_{mm'}$ in our tight-binding description [see Eq. (3.2) in Chap. 3]. Since $V_{n-1,n} = V^\dagger_{n,n-1}$, one can write from Eq. (C.11)

$$I_{(n-1,m)\to(n,m)} = \frac{-2e}{\hbar}\int\frac{\mathrm{d}E}{2\pi}2\,\mathrm{Re}\left\langle m\left|\, G^<_{n,n-1}V_{n-1,n}\,\right| m\right\rangle. \tag{C.13}$$

Now, for obtaining an equation expressing $G^<$ in retarded and advanced Green's functions, one proceeds as follows. The device is split into three uncoupled parts, as shown in Fig. C.2: a single column n is uncoupled from the parts to its left and right. The relation between Green's function operators of the uncoupled system and those of the coupled system is given in terms of a Dyson's equation. For the lesser-than Green's function, this equation looks like [76]

$$G^< = g^< + GVg^< + G^<Vg^\dagger, \tag{C.14}$$

where V describes the hopping between the three subsystems. Green's function operators denoted by a capital are for the coupled system, while those denoted by a small letter are for the uncoupled system. G and g are retarded Green's function operators, as defined in Chap. 4. Projecting this Dyson's equation between columns n and $n-1$, and multiplying with $V_{n-1,n}$ one finds

$$G^<_{n,n-1}V_{n-1,n} = G_{nn}V_{n,n-1}g^<_{n-1,n-1}V_{n-1,n} + G^<_{nn}V_{n,n-1}g^\dagger_{n-1,n-1}V_{n-1,n}. \tag{C.15}$$

We will define

$$\Sigma^{<,l}_n = V_{n,n-1}g^<_{n-1,n-1}V_{n-1,n}, \tag{C.16}$$

$$\Sigma^{<,r}_n = V_{n,n+1}g^<_{n+1,n+1}V_{n+1,n}, \tag{C.17}$$

$$\Sigma^l_n = V_{n,n-1}g_{n-1,n-1}V_{n-1,n}, \tag{C.18}$$

$$\Sigma^r_n = V_{n,n+1}g_{n+1,n+1}V_{n+1,n}. \tag{C.19}$$

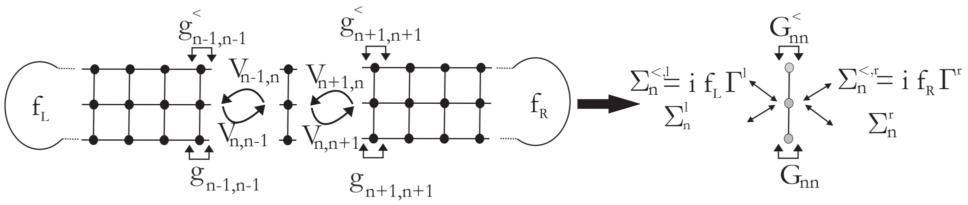

Figure C.2: Green's functions for the evaluation of the vertex currents.

These expressions can be interpreted as being self-energies describing the influence of the part of the device to the left (superscript l) or right (superscript r) of column n. With these definitions, Eq. (C.15) becomes

$$G^<_{n,n-1}\, V_{n-1,n} = G_{nn}\, \Sigma_n^{<,l} + G^<_{nn}\left(\Sigma_n^l\right)^\dagger \tag{C.20}$$

Now, we need to resort to three equations that can only be fully understood within the Keldysh formalism.

The first one

$$\Sigma_n^{<,l(r)} = \mathrm{i} f_{L(R)}\, \Gamma_n^{l(r)}, \tag{C.21}$$

with

$$\Gamma_n^{l(r)} = \mathrm{i}\Big[\Sigma_n^{l(r)} - \big(\Sigma_n^{l(r)}\big)^\dagger\Big] \tag{C.22}$$

describes that the left (right) part of the device, decoupled from column n, will be in thermodynamic equilibrium with the left (right) reservoir [$f_L(R)$ is the Fermi-Dirac distribution in the left (right) reservoir].

The second one is a kinetic equation describing the injection and extraction of carriers from the leads

$$\begin{aligned} G^<_{nn} &= G_{nn}\big[\Sigma_n^{<,l} + \Sigma_n^{<,r}\big] G^\dagger_{nn} \\ &= \mathrm{i} f_L G_{nn}\Gamma_n^l G^\dagger_{nn} + \mathrm{i} f_R G_{nn}\Gamma_n^r G^\dagger_{nn} \\ &= \mathrm{i} f_L G_{nn}\big[\Gamma_n^l + \Gamma_n^r\big] G^\dagger_{nn} - \mathrm{i}(f_L - f_R)\, G_{nn}\Gamma_n^r G^\dagger_{nn}. \end{aligned} \tag{C.23}$$

The third equation is a generally valid relation

$$G_{nn} - G^\dagger_{nn} = -\mathrm{i}\, G_{nn}\big[\Gamma_n^l + \Gamma_n^r\big] G^\dagger_{nn}, \tag{C.24}$$

that can be used to write Eq. (C.23) as

$$G^<_{nn} = -f_L\big[G_{nn} - G^\dagger_{nn}\big] - \mathrm{i}\big(f_L - f_R\big) G_{nn}\Gamma_n^r G^\dagger_{nn} \tag{C.25}$$

Finally, substituting Eqs. (C.21) and (C.25) in Eq. (C.20) gives

$$G^<_{n,n-1} V_{n-1,n} = -f_L\big[G_{nn}\Sigma_n^l - G^\dagger_{nn}(\Sigma_n^l)^\dagger\big] - \mathrm{i}(f_L - f_R)\big[G_{nn}\Gamma_n^r G^\dagger_{nn}\big(\Sigma_n^l\big)^\dagger\big] \tag{C.26}$$

Putting this in Eq. (C.13), and using the fact that $\mathrm{Re}(-\mathrm{i}z) = \mathrm{Im}(z)$, one obtains the final expression for the longitudinal current:

$$I_{(n-1,m)\to(n,m)} = \frac{2e}{\hbar}\int\frac{\mathrm{d}E}{2\pi}\,\Big[f_L A - \big(f_L - f_R\big)B\Big], \tag{C.27}$$

with the matrix elements

$$\begin{aligned} A &= 2\,\mathrm{Re}\left\langle m\middle|\, G_{nn}\,\Sigma_n^l - \Sigma_n^l\,G_{nn}\,\middle| m\right\rangle, && \text{(C.28a)}\\ B &= 2\,\mathrm{Im}\left\langle m\middle|\, G_{nn}\,\Gamma_n^r\,G_{nn}^\dagger\,(\Sigma_n^l)^\dagger\,\middle| m\right\rangle. && \text{(C.28b)} \end{aligned}$$

C.2.2 Transverse current

The transverse current now needs less work. From Eq. (C.12), we just write

$$I_{(n,m)\to(n,m+1)} = \frac{-2e}{\hbar}\int\frac{\mathrm{d}E}{2\pi}2\,\mathrm{Re}\left\langle m+1\middle|\,(t^y_{nm})^* G^<_{nn}\,\middle| m\right\rangle \tag{C.29}$$

Substituting Eq. (C.25) for $G^<_{nn}$, one immediately finds the expression for the transverse current in terms of Green's functions calculated in Chap. 4:

$$I_{(n,m)\to(n,m+1)} = \frac{2e}{\hbar}\int\frac{\mathrm{d}E}{2\pi}\,\Big[f_L C - \big(f_L - f_R\big)D\Big], \tag{C.30}$$

with the matrix elements

$$\begin{aligned} C &= 2\,\mathrm{Re}\left\langle m+1\middle|\,(t^y_{m,n})^*\,(G_{nn} - G^\dagger_{nn})\,\middle| m\right\rangle, && \text{(C.31a)}\\ D &= 2\,\mathrm{Im}\left\langle m+1\middle|\,(t^y_{m,n})^*\,G_{nn}\,\Gamma_n^r\,G^\dagger_{nn}\,\middle| m\right\rangle. && \text{(C.31b)} \end{aligned}$$

Appendix D

Persistent and transport contributions to the current density

In Sec. 5.3.3, the total current density in a nonequilibrium situation was written as a sum of two parts. It was argued that an interpretation of these two parts in terms of a persistent and a transport contribution, as put forward in Refs. [66, 67], cannot be physically relevant because such an interpretation is not unique. In this Appendix, we will look at this issue again in some more detail.

In a nonequilibrium situation, a bias voltage is applied so that the chemical potential of one of the leads is higher than that of the other lead. In the present discussion, we will assume that $\mu_L > \mu_R$. Since the reservoirs connected to the leads are assumed to be in thermal equilibrium, the chemical potentials μ_L and μ_R are well-defined. In the central device however, the Fermi level E_F is not known a priori, and it should in principle be calculated self-consistently. Nevertheless, in most calculations (ours also), the redistribution of charges in the sample as a result of the current flowing is not taken into account, and one then puts the Fermi energy in the device at a more or less arbitrary level between μ_L and μ_R.

In Refs. [66, 67], the total current density in nonequilibrium is divided in what is called an "equilibrium" (or persistent) and a "nonequilibrium" (or transport) part: $\mathbf{j}_{\text{tot}} = \mathbf{j}_{\text{pers}} + \mathbf{j}_{\text{transp}}$. The persistent part is defined as the current arising from states below the Fermi energy in the device, which are *assumed to be all occupied* (at temperature $T = 0$). The transport part is defined as the remaining current resulting from the states with energies between μ_L and μ_R. Since the position of the Fermi level in the device is completely arbitrary (without a self-consistent calculation), this subdivision cannot be a physically relevant one, and it can lead to some confusion as to how the transport current density distribution looks like. This will be made clearer with the help of Figs. D.1 and D.2.

Take as an example a quantum wire with a constriction in the middle, and let's have a look at the scattering states in this system. In presence of a high magnetic

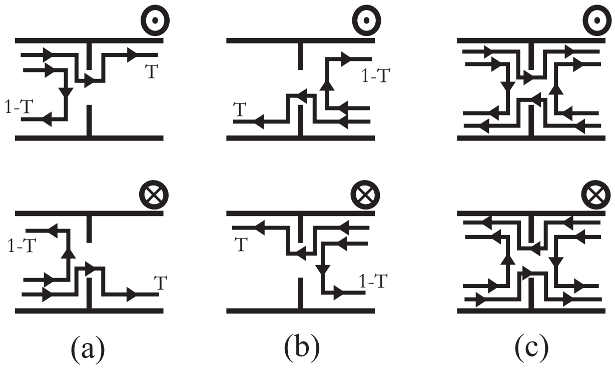

Figure D.1: Scattering states emerging from the left (a) and right (b) lead, for opposite directions of the magnetic field. The persistent current density (c) will look like the sum of (a) and (b).

field, electrons will move along the edges of the system. An electron with a certain energy has a probability T for being transmitted through the structure, and a probability $1 - T$ of being reflected. Scattering states emerging from the left are schematically drawn in Fig. D.1(a), while those emerging from the right lead are shown in Fig D.1(b).

The persistent part of the current $\mathbf{j}_{\text{pers}}$ results from all states below E_F. According to the definition above, both the states emerging from the left and the right lead are assumed to be occupied up to the Fermi level when calculating the persistent current, and therefore the persistent current density always looks as in Fig. D.1(c), namely a sum of the currents in Figs. D.1(a) and (b).

Now we turn our attention to the transport part $\mathbf{j}_{\text{trans}}$. Suppose that we have put the Fermi energy in the device E_F equal to μ_R, as in Fig. D.2(a). The transport part of the current distribution was defined as that part resulting from states between μ_L and μ_R. Since all states between μ_R and μ_L that are occupied with electrons are emerging from the left lead, the transport density distribution will look as the middle panel of Fig. D.2(a), it is the same as Fig. D.1(a).

Had we put the Fermi energy equal to μ_L as in Fig. D.2(b), then the persistent part of the current would contain a too large contribution: remember that all states below $E_F = \mu_L$ are assumed to be occupied in the persistent part, so also those emerging from the right lead with energies between μ_R and μ_L. Since these are not occupied in real life, the transport part should even things out and is obtained by subtracting the contribution from these states in order to obtain the correct total current density. The transport current density for this situation is depicted in the middle panel of Fig D.2(b); it is the same as that of Fig. D.1(b), but with the sign reversed because we have to subtract this contribution.

Yet another picture emerges when one puts the Fermi energy in the middle between μ_L and μ_R [as in Fig. D.2(c)]. In this case, for the persistent current, we have taken a too large contribution of currents emerging from the right lead,

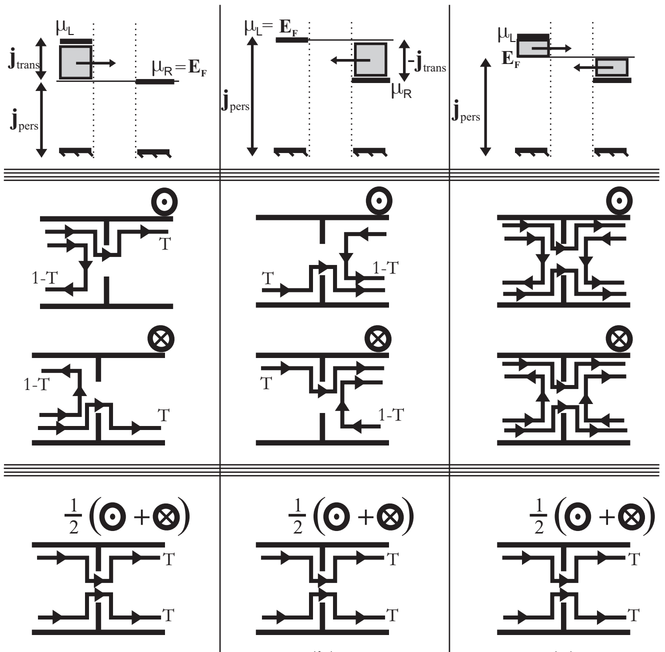

(a) (b) (c)

Figure D.2: The transport current distribution $\mathbf{j}_{\text{trans}}$ depends upon the choice of the Fermi level in the device. From left to right, the distributions that result for $E_F = \mu_L$ (a), $E_F = \mu_R$ (b), and $E_F = \frac{\mu_L+\mu_R}{2}$ (c) are shown, and this for different directions of the magnetic field. Symmetrizing the distributions with respect to the magnetic field direction gives a unique picture for all possible choices of the Fermi level (lowest three pictures).

and a too small contribution of currents emerging from the left lead. By evening things out in the transport part in order to obtain the correct total current density, the transport current for this part now will look as the middle panel of Fig. D.2(c).

It is clear that, depending on where the Fermi level is put in the device, the transport current density $\mathbf{j}_{\text{trans}}$ looks completely different. In one picture, it seems that electrons are flowing on the upper edge of the sample, in the other pictures they flow on the lower edge or even on both edges. Therefore, splitting the current density distribution in a persistent and transport part in the way it is done in Refs. [66, 67] cannot be physically relevant, and only the sum of both contributions can be attributed a physical meaning.

Nevertheless, we have found a unique way of defining persistent and transport contributions of the current density by looking at its symmetric and antisymmetric parts. This was already mentioned in Sec. 5.3.3: persistent currents are antisymmetric in the magnetic field, and a transport contribution to the current density could thus be defined as the symmetric part of the total current density. As shown in the lower panel of Fig. D.2, doing this symmetrization gives us a definition of the transport current density distribution that is unique, whatever choice we make for the value of E_F in the device. It gives us only that part of the current that is really flowing from one lead into the other, describing a real transport current.

Appendix E

Efficient evaluation of the conductance decrease flow map

For the local scatterer method in Chap. 5, it is necessary to calculate the difference ΔG between the conductances in the absence and presence of the scanning probe tip [see Eq. (5.2]. When the tip influence on site (m, n) is introduced via Dyson's equation, this can be done with a numerical effort scaling as $M^3 N$, as will be shown next.

One can write from Eq. (5.5):

$$G_{N1} = G^0_{N1} + A, \tag{E.1}$$

with the $M \times M$ matrix:

$$A = G^0_{Nn}\, V^{\text{tip}}_{nn}\, (1 - G^0_{nn}\, V^{\text{tip}}_{nn})^{-1}\, G^0_{n1}. \tag{E.2}$$

Since V^{tip}_{nn} has only one nonzero element, namely on position (n, m), one can write A as a product of a column matrix and a row matrix:

$$A = [G^0_{Nn}]_{m^{\text{th}}\text{column}}\; \tau\; [G^0_{n1}]_{m^{\text{th}}\text{row}}, \tag{E.3}$$

with the scalar τ given by (w is the magnitude of the repulsive tip potential):

$$\tau = \frac{w}{1 - w\, \langle m|G^0_{nn}|m\rangle}. \tag{E.4}$$

By substituting Eq. (E.1) into Eq. (5.3), one obtains:

$$\begin{aligned} T(m,n) &= \text{Tr}\,[\Gamma_R(G^0_{N1} + A)\Gamma_L(G^0_{N1} + A)^\dagger \\ &= \text{Tr}\,[\Gamma_R G^0_{N1}\Gamma_L(G^0_{N1})^\dagger] + \text{Tr}\,[\Gamma_R G^0_{N1}\Gamma_L(A)^\dagger + \Gamma_R A\Gamma_L(G^0_{N1})^\dagger] \\ &\qquad + \text{Tr}[\Gamma_R A \Gamma_L A^\dagger] \\ &= T_0 + 2\text{Re}\,\text{Tr}\,[\Gamma_R A\Gamma_L(G^0_{N1})^\dagger] + \text{Tr}[\Gamma_R A\Gamma_L A^\dagger]. \end{aligned}$$

In order to evaluate the conductance difference $\Delta g = 2e^2/h(T_0 - T(m, n))$, we need to evaluate only the last two terms. The last term only involves products of the

$M \times M$ matrices $\Gamma_{L(R)}$ with row or column matrices because of the special form of A. The computational effort for such terms scales as M^2, which corresponds to a total effort of M^3N for all tip locations. Furthermore, since the product $\Gamma_L(G^0_{N1})^\dagger$ in the other term is independent of the tip position, it has to be calculated only once (with an effort M^3). When this matrix is known, the trace contains only products of an $M \times M$ matrix with a row or column matrix, so the total effort for this term also scales as M^3N in the limit of large N.

Appendix F

Effective Hamiltonian for an electron in a discretized magnetic texture

The effective Hamiltonian $\mathcal{H}_{\text{eff}}$ that was given in Eq. (7.20) of Chap. 7 for electrons moving in a magnetic texture will be derived in more detail in this Appendix, and an analytical criterion for its validity will be obtained. Our starting point is the Hamiltonian Eq. (7.15). Calculating the matrix representation of this Hamiltonian in the basis of states $|i,\pm\rangle$ with their spins aligned parallel or antiparallel with respect to the local magnetization direction at site i according to Eq. (7.16), one finds (we will consider only two sites here for the ease of writing):

$$\mathcal{H} = \left[\begin{array}{cc} A & T \\ T^\dagger & A \end{array} \right], \tag{F.1}$$

where A describes the on-site terms, and is given by the diagonal matrix

$$A = \Delta \left[\begin{array}{cc} -1/2 & 0 \\ 0 & 1/2 \end{array} \right], \tag{F.2}$$

while the matrix T describes hopping between the sites, and is given by

$$T = -t \left[\begin{array}{cc} \sin\frac{\theta_1}{2}\sin\frac{\theta_2}{2} + \cos\frac{\theta_1}{2}\cos\frac{\theta_2}{2} e^{\mathrm{i}(\phi_1-\phi_2)} & \sin\frac{\theta_1}{2}\cos\frac{\theta_2}{2} e^{\mathrm{i}\phi_2} - \cos\frac{\theta_1}{2}\sin\frac{\theta_2}{2} e^{\mathrm{i}\phi_1} \\ \cos\frac{\theta_1}{2}\sin\frac{\theta_2}{2} e^{-\mathrm{i}\phi_1} - \sin\frac{\theta_1}{2}\cos\frac{\theta_2}{2} e^{-\mathrm{i}\phi_2} & \sin\frac{\theta_1}{2}\sin\frac{\theta_2}{2} + \cos\frac{\theta_1}{2}\cos\frac{\theta_2}{2} e^{-\mathrm{i}(\phi_1-\phi_2)} \end{array} \right]. \tag{F.3}$$

Calculating the module of the elements of T, one can write

$$T = -t \left[\begin{array}{cc} \cos\frac{\theta_{12}}{2} e^{\mathrm{i}\gamma_{12}} & \sin\frac{\theta_{12}}{2} e^{\mathrm{i}\delta_{12}} \\ -\sin\frac{\theta_{12}}{2} e^{-\mathrm{i}\delta_{12}} & \cos\frac{\theta_{12}}{2} e^{-\mathrm{i}\gamma_{12}} \end{array} \right], \tag{F.4}$$

where θ_{12} is the angle between the magnetization directions at site 1 and 2. An expression for the phase γ_{12} will be derived further down.

If the exchange splitting would be infinite, we could neglect the matrix T, and obtain two energy levels that are twofold degenerate, corresponding to an electron sitting in site 1 or 2, with spin up or down with respect to the local magnetization direction. For finite splitting Δ, the matrix T will give two different hopping contributions: the diagonal elements of T describe hopping within the same spin subband, keeping the spin aligned to the local magnetization direction upon hopping. In perturbation theory, these terms will give rise to corrections of the order of t. The off-diagonal elements of T will couple both spin subbands, and give only second order contributions in perturbation theory. These will be of magnitude $\big(t^2/\Delta\big)\sin(\theta_{12})$. As such, these second order contributions can be neglected when the condition

$$\left(\frac{t^2}{\Delta}\right)\sin(\theta_{12}) \approx \frac{t^2}{\Delta}\,\theta_{12} \ll t \tag{F.5}$$

is fulfilled, which is the tight-binding version of the adiabaticity criterion we defined in Eq. (7.24) in Chap. 7. In this limit, the spin-up and spin-down subband are decoupled and can be treated independently. For the spin-up subband, we then find (generalized to an arbitrary number of sites):

$$\mathcal{H}^{\text{eff}} = -\sum_{\langle i,j\rangle} t_{ij}^{\text{eff}}|i,+\rangle\langle j,+| - \Delta/2, \tag{F.6}$$

with t_{ij}^{eff} found from Eq. (F.4):

$$t_{ij}^{\text{eff}} = t\cos\frac{\theta_{ij}}{2}\, e^{\mathrm{i}\gamma_{ij}}. \tag{F.7}$$

Let's see now how one can evaluate the phases γ_{ij}. We will use from now on the shorthand notation $|\mathbf{n}_i\rangle = |i,+\rangle$ for a spin-up state with respect to the local magnetization direction $\mathbf{n}_i$ at site i. Looking back at Eq. (F.3), it should be clear that $t_{ij}^{\text{eff}} = t\langle\mathbf{n}_i|\mathbf{n}_j\rangle$, so the phase γ_{ij} can be found by evaluating the argument of this scalar product. As such, it is clear that γ_{ij} is not gauge invariant since multiplying the basis states with a phase factor will give different results. In particular, suppose we fix the phase of the state $|\mathbf{n}_i\rangle$, and do parallel transport (see Sec. 7.2.1) of this state to obtain the state $|\mathbf{n}_j\rangle$. On the sphere geometry, parallel transport just means that we rotate $|\mathbf{n}_i\rangle$ around an axis $\boldsymbol{\omega} \sim \mathbf{n}_i \times \mathbf{n}_j$ to obtain $|\mathbf{n}_j\rangle$. It is not so difficult to show that with this gauge choice, one finds that the scalar product $\langle\mathbf{n}_i|\mathbf{n}_j\rangle$ is real, so that the quantity γ_{ij} is zero.

Naively, one might argue now that one can always make a similar construction, so that the γ_{ij} will be zero for every i and j. However, this is not true, as the gauge defined by the "parallel transport construction" cannot be defined globally. Indeed, consider three sites with magnetization directions $\mathbf{n}_1, \mathbf{n}_2, \mathbf{n}_3$ and now we make a closed loop $1 \to 2 \to 3 \to 1$. The phase picked up by the electron along this path is then given by

$$\arg\big(\langle\mathbf{n}_1|\mathbf{n}_2\rangle\langle\mathbf{n}_2|\mathbf{n}_3\rangle\langle\mathbf{n}_3|\mathbf{n}_1\rangle\big) = \arg\langle\mathbf{n}_1|\mathbf{n}_2\rangle + \arg\langle\mathbf{n}_2|\mathbf{n}_3\rangle + \arg\langle\mathbf{n}_3|\mathbf{n}_1\rangle, \tag{F.8}$$

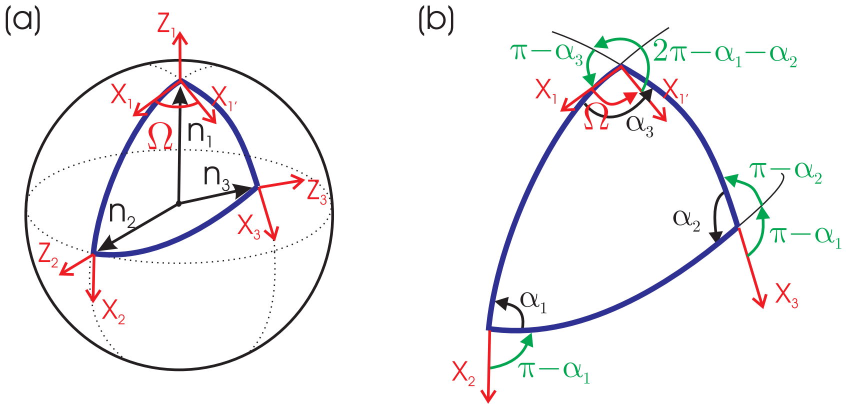

Figure F.1: Parallel transport of a local X axis along a closed loop on the unit sphere (a), and a visualization of how to calculate the angle between the original and the transported axis (b).

and corresponds to the Berry phase. This phase is gauge invariant as can be seen since every state appears both as a bra and as a ket. We choose the following gauge to evaluate this Berry phase: we first obtain $|\mathbf{n}_2\rangle$ from parallel transport of $|\mathbf{n}_1\rangle$, and in the same way we get $|\mathbf{n}_3\rangle$ from $|\mathbf{n}_2\rangle$. We then know that by construction the first two arguments on the right hand side of Eq. (F.8) are zero. For the third argument however, we cannot make such a construction anymore because parallel transport of $|\mathbf{n}_3\rangle$ will give a state $|\mathbf{n}_1'\rangle$ that differs from the state $|\mathbf{n}_1\rangle$ we have started from:

$$|\mathbf{n}_1\rangle = e^{\mathrm{i}\frac{\Omega}{2}}|\mathbf{n}_1'\rangle, \tag{F.9}$$

and the Berry phase will thus be equal to the phase $\Omega/2$. Let's see now why this phase factor appears, and what its meaning is.

First, note that with every state $|\mathbf{n}_i\rangle$, or equivalently with every point on the unit sphere, a local $X_iY_iZ_i$-frame can be associated, with the Z_i axis pointing along the vector $\mathbf{n}_i$ as depicted in Fig. F.1(a). When this frame is rotated around the Z_i axis, the state $|\mathbf{n}_i\rangle$ will pick up a phase factor, because

$$\mathcal{R}_{\mathbf{n}_i}(\Omega)\,|\mathbf{n}_i\rangle = e^{\mathrm{i}\frac{\Omega}{2}\sigma_{\mathbf{n}_i}}|\mathbf{n}_i\rangle = e^{\mathrm{i}\frac{\Omega}{2}}|\mathbf{n}_i\rangle, \tag{F.10}$$

where $\mathcal{R}_{\mathbf{n}_i}(\Omega)$ is the operator for rotation over an angle Ω. As such, one can state that fixing the phase of $|\mathbf{n}_1\rangle$ corresponds to defining the orientation of a local X_1 axis associated with this state. Now, when doing parallel transport of this state, the X_1 axis associated with it will simultaneously also be parallel transported, as shown in Fig. F.1(a). As we already pointed out in Sec. 7.2.1, after parallel transport along the closed path $1 \to 2 \to 3 \to 1$, the X axis will have rotated compared to the orientation it started from. The rotation angle can be found with the help of Fig. F.1(b), in which we give a more detailed view of the triangle on the unit sphere defined by the vectors $\mathbf{n}_1, \mathbf{n}_2, \mathbf{n}_3$. The angle the X axes make with successive sides of the triangle jumps at each vertex, by π minus the angle α_i at the vertex. This gives a total angle of

$$3\pi - \sum \alpha_i = 2\pi - \Omega, \tag{F.11}$$

between the transported X axis ($X_{1'}$ in the figure) and the original X axis (X_1). The angle $\Omega = \sum \alpha_i - \pi$ is known to be the solid angle subtended on the unit sphere by the three vectors $\mathbf{n}_1, \mathbf{n}_2, \mathbf{n}_3$ [120]. For the rotation of a geometric vector, the factor 2π is unimportant since it is equal to the identity operation. However, for a spin-1/2 state, a rotation around 2π introduces a factor of -1 [see Eq. (F.10)]. Therefore, it is important to really measure the correct angle going "directly", i.e., without winding an extra time around the Z_1 axis, from the X_1 axis to the $X_{1'}$ axis: this angle is given by 2π minus the rotation angle in Eq. (F.11) [see Fig. F.1(b)], so that finally we obtain the angle $+\Omega$. From Eq. (F.10), it is clear then that this rotation of the local X axis after parallel transport around the loop corresponds to a Berry phase of $\Omega/2$ that the electronic state picks up along the same loop.

In conclusion, we can say that the phases γ_{ij} of the effective hopping elements are not gauge invariant. Only the total phase picked up along a closed path, i.e, the Berry phase, is gauge invariant. This means that we can choose the γ_{ij} more or less freely, as long as we make sure that the phase picked up along any closed loop equals half of the solid angle subtended by the magnetization vectors along that loop. The gauge choice we have made in Chap. 7, defined in Fig. 7.3 clearly fulfills such condition.

One final note. When considering the effective Hamiltonian for the spin-down subband, one can make exactly the same construction to obtain the Berry phase of the spin-down electron. However, since $\sigma_{\mathbf{n}_i}|\mathbf{n}_i, -\rangle = -|\mathbf{n}_i, -\rangle$, the phase picked up by this state will be $-\Omega/2$, as is clear from Eq. (F.10) and the discussion above.

Appendix G

Calculation of the Hall resistivity

In Chap. 7, there was need for a phase averaging procedure in order to find the Hall resistivity of a macroscopic system based on calculations on smaller phase coherent sections with the Landauer-Büttiker formalism. In order to discuss the subtleties related to such an averaging procedure, we will first look at how we can retrieve Ohm's law for the longitudinal resistivity of a wire based on resistance calculations within the Landauer-Büttiker formalism. Although this can be found in textbooks nowadays (see, e.g., Ref. [2]), it will pave the way for the slightly more involved procedure we need for defining the Hall resistivity.

The main idea is that a macroscopic system can be build up from small phase coherent subsections that are attached in an incoherent way. For example, a macroscopic wire can be subdivided in small sections of length $L \approx L_\phi$. The resistance $R_i = \frac{V_2 - V_1}{I}$ between two leads attached to such a section [depicted in Fig. G.1(a)] can be calculated within the Landauer-Büttiker formula: $R_i = \frac{h}{2e^2 T_i}$ with T_i the transmission coefficient between the two terminals. R_i will of course be dependent upon the impurity configuration in the section. Now one could combine a number of small sections in series to form a macroscopic wire as in Fig. G.1(c). Each section will be treated as a classical resistor with a current-voltage relationship $I = R_i V$, and as such we introduce an effective phase breaking event at the connection between every two resistors: only current and voltage information is kept, and any phase information of electrons flowing out of the section is lost. The total resistance of this wire is then just the sum $R = \sum_i R_i$. When enough sections (with different impurity configurations) are attached, it is clear that R will be independent of the choice of impurity configurations in the separate subsections. Therefore, one can find the resistivity of the system as $\rho = RW/L$, where W is the width of the sections, and L is the length of the complete wire. In this way, one obtains Ohm's law with an essentially mesoscopic approach in which phase breaking is introduced phenomenologically by applying classical circuit theory to connect smaller phase coherent sections.

However, there is a subtle point that we have glossed over in the calculation of the individual resistances R_i. For calculating R_i, we attach two leads (connected

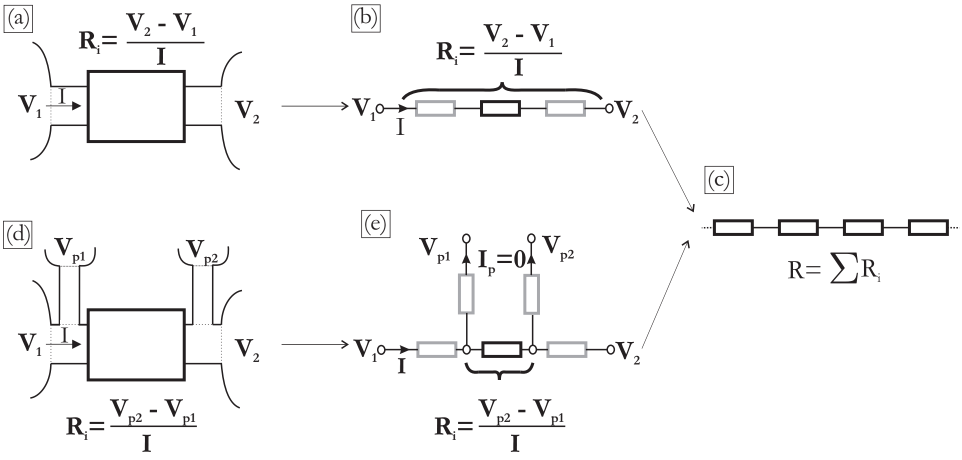

Figure G.1: Phase averaging procedure for obtaining resistivity properties of a wire. A four-terminal measurement procedure is necessary for obtaining the resistances R_i of the separate sections in order to remove contact resistance effects.

to large electron reservoirs) at the sample edges. But it is known that at every reservoir-lead interface, a so-called contact resistance is build up (see, e.g., p.94 in Ref. [3] and references cited there). Essentially such contact resistance results because on one side (the reservoir) current is carried by an infinite number of modes, while on the other side (the mesoscopic lead) there are only a finite number of modes transporting current. So when calculating R_i as the voltage drop between the reservoirs divided by the current flowing through the sample, R_i will also incorporate two such contact resistances, and does not correspond to the pure resistance of the sample itself. This is made clear in Fig. G.1(b). It means that R_i will be nonzero even when section i would not contain any scatterers at all! The resistivity ρ obtained from the procedure described above will thus depend strongly on such contact resistances, which is clearly unwanted.

The standard way of getting rid of this contact resistance is to calculate R_i with a four-terminal setup as in Fig. G.1(d). Current is passed through the sample by two leads, while two extra leads are used to measure the voltage drop over the sample. Since these extra voltage probes do not draw any current, there will be no voltage drop over their contact resistances, and they will measure the voltage at the point where they are attached. Placing them as in Fig. G.1(d), one is able to measure the voltage drop over the sample, excluding the voltage drop over the contact resistances of the current-carrying leads [Fig. G.1(e)]. As such the resistance $R_i = \frac{V_{p2}-V_{p1}}{I}$ is the pure resistance of the sample only and it is these resistances that should be added in series to find the longitudinal resistivity ρ.

Now we come to the point of calculating the Hall resistivity ρ_H, which is slightly more complicated although it follows the same philosophy. This time, the smaller sections we want to start from in order to build up a macroscopic sys-

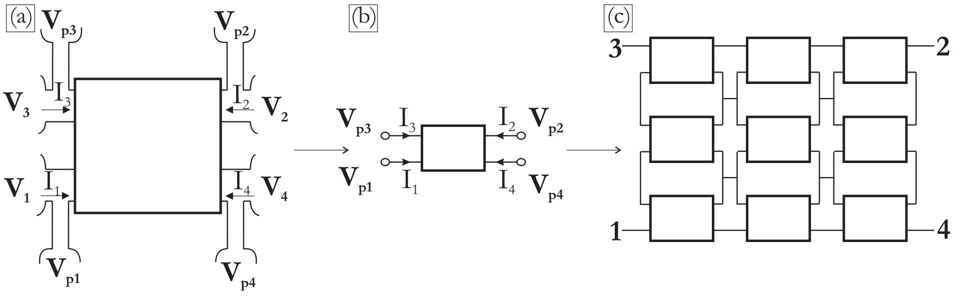

Figure G.2: Averaging procedure for defining the Hall resistivity. An eight-terminal measurement gets rid of contact resistances (a). Since the current through the voltage probes is zero, effective four-terminal current-voltage relations can be derived (b). These four-terminal sections are wired together using classical circuit theory (c).

tem already have four terminals, and were depicted in Fig. 7.4. In order to get rid of contact resistance effects, we will make an eight-terminal structure out of it by attaching four extra voltage probes as in Fig. G.2(a). The Landauer-Büttiker formalism can then be used to derive a set of linear equations relating the currents and voltages at the eight leads:

$$\begin{bmatrix} \mathbf{I} \\ \mathbf{I_p} \end{bmatrix} = \begin{bmatrix} A & B \\ C & D \end{bmatrix} \begin{bmatrix} \mathbf{V} \\ \mathbf{V_p} \end{bmatrix}, \tag{G.1}$$

where $\mathbf{I} = (I_1, \ldots, I_4)$ is a vector containing the currents through the original four terminals, and $\mathbf{I_p} = (I_{p1}, \ldots, I_{p4})$ are the currents through the voltage probes; the same notation convention is used for the voltages on the leads. The 4×4 matrices A, B, C and D consist of transmission coefficients between all eight leads, and are found directly from the Landauer-Büttiker equations [c.f. Eq. (2.2) in Chap. 2].

Since the voltage probes do not draw current, we find

$$\mathbf{I_p} = 0 = C\mathbf{V} + D\mathbf{V_p}, \tag{G.2}$$

which can be used to express the currents through the four current-carrying leads as a function of the voltage on the attached voltage probes:

$$\mathbf{I} = \big[B - AC^{-1}D\big]\mathbf{V_p}. \tag{G.3}$$

Doing so, we have found current-voltage relations for the original *four-terminal* structure in which spurious contact resistances have been got rid off. Next, such structures [depicted in Fig. G.2(b)] with different impurity configurations will be wired up together as in Fig. G.2(c) treating every structure as a classical circuit obeying Eq. (G.3) and taking care of current conservation laws at the connecting points. Since classical laws are used in wiring up the system, all phase information is lost at the connection points, and an effective phase coherence length is introduced which corresponds to the size of a single section.

In the end, one obtains current-voltage relations between the unconnected leads at the four corners of the structure [labeled $1, \ldots, 4$ in Fig. G.2(c)], and these can be used to find the resistances $R_{12,34}, R_{34,12}, R_{14,23}$ and $R_{42,31}$ between the corners of the large structure. The properties of the complete system can then be expressed in terms of resistivities by making use of the van der Pauw technique [121], which gives the Hall resistivity as [121, 122]

$$\rho_H = R_H = \frac{1}{2}\left(R_{12,34} - R_{34,12}\right) \tag{G.4}$$

while the longitudinal resistivity ρ_L can be found from solving the equation [121]

$$\exp\left(-\pi R_{14,23}/\rho_L\right) + \exp\left(-\pi R_{42,31}/\rho_L\right) = 1. \tag{G.5}$$

When enough sections are wired up together, these transport coefficients will be independent of the impurity configurations in the separate sections.

A small comment should be made here. Because of the attachment procedure described above, one cannot expect the resistivities calculated in Eqs. (G.4) and (G.5) to correspond exactly to the real resistivities of a “bulk” system with the same mean free path. In particular, the resistivities as calculated above depend on the width of the leads attached to the smaller sections, and also on the scheme of wiring the sections together. In theory one could take into account these effects (see, e.g., Ref. [121]), and one would find that the real ”bulk”resistivity and the resistivity calculated above are equal up to a factor that is purely geometrical. Calculating this factor explicitly however is practically quite difficult. Since the factor is of a purely geometric origin and does not have any physical implications, we did not proceed in this direction.

Bibliography

[1] R. A. Webb, S. Washburn, C. P. Umbach, and R. B. Laibowitz, Phys. Rev. Lett. **54**, 2696 (1985).

[2] S. Datta, *Electronic Transport in Mesoscopic Systems* (Cambridge University Press, Cambridge, 1995).

[3] Y. Imry, *Introduction to Mesoscopic Physics* (Oxford University Press, New York, 1997).

[4] B. J. van Wees, H. van Houten, C. W. J. Beenakker, J. G. Williamson, L. P. Kouwenhoven, D. van der Marel, and C. T. Foxon, Phys. Rev. Lett. **60**, 848 (1988).

[5] D. A. Wharam, T. J. Thornton, R. Newbury, M. Pepper, H. Ahmed, J. E. F Frost, D. G. Hasko, D. C. Peacock, D. A. Ritchie, and G. A. C. Jones, J. Phys. C **21**, L209 (1988).

[6] P. A. Lee, A. D. Stone, and H. Fukuyama, Phys. Rev. B **35**, 1039 (1987).

[7] G. Bergmann, Phys. Rep. **107**, 1 (1984).

[8] P. A. Lee and T. V. Ramakrishnan, Rev. Mod. Phys. **57**, 287 (1985).

[9] D. M. Eigler and E. K. Schweizer, Nature **344**, 524 (1990).

[10] A. Yacoby, Solid State Comm. **111**, 1 (1999).

[11] N. B. Zhitenev, T. A. Fulton, A. Yacoby, H. F. Hess, L. N. Pfeiffer, and K. W. West, Nature **404**, 473 (2000).

[12] S. H. Tessmer, P. I. Glicofridis, R. C. Ashoori, L. S. Levitov, and M. R. Melloch, Nature **392**, 51 (1998).

[13] G. Finkelstein, P. I. Glicofridis, R. C. Ashoori, and M. Shayegan, Science **289**, 90 (2000).

[14] M. A. Topinka, B. J. LeRoy, S. E. J. Shaw, E. J. Heller, R. M. Westervelt, K. D. Maranowski, and A. C. Gossard, Science **289**, 2323 (2000).

[15] M. A. Topinka, B. J. LeRoy, R. M. Westervelt, S. E. J. Shaw, R. Fleischmann, E. J. Heller, K. D. Maranowski, and A. C. Gossard, Nature **410**, 183 (2001).

[16] M. N. Baibich, J. M. Broto, A. Fert, F. Nguyen Van Dau, F. Petroff, P. Eitenne, G. Creuzet, A. Friederich, and J. Chazelas, Phys. Rev. Lett. **61**, 2472 (1988).

[17] J. Barnas, A. Fuss, R. E. Camley, P. Grünberg, and W. Zinn, Phys. Rev. B **42**, 8110 (1990).

[18] G. Schmidt, D. Ferrand, L. W. Molenkamp, A. T. Filip, and B. J. van Wees, Phys. Rev. B **62**, 4790 (2000).

[19] E. I. Rashba, Phys. Rev. B **62**, 16267 (2000).

[20] F. G. Monzon and M. L. Roukes, J. Magn. Magn. Mater. **198**/**199**, 632 (1999).

[21] D Frustaglia, M Hentschel, and K Richter, Phys. Rev. Lett. **87**, 256602 (2001).

[22] S. Datta and B. Das, Appl. Phys. Lett. **56**, 665 (1990).

[23] D Frustaglia and K Richter, Phys. Rev. B **69**, 235310 (2004).

[24] R. Ionicioiu and I. D'Amico, Phys. Rev. B **67**, 041307 (2003).

[25] J. E. Hirsch, Phys. Rev. Lett **83**, 1834 (1999).

[26] S. Murakami, N. Nagaosa, and S.-C. Zhang, Science **301**, 1348 (2003).

[27] J. Sinova, D. Culcer, Q. Niu, N. A. Sinitsyn, T. Jungwirth, and A. H. MacDonald, Phys. Rev. Lett **92**, 126603 (2004).

[28] C. W. J. Beenakker and H. van Houten, in *Solid State Physics,* ***44***, edited by H. Ehrenreich and D. Turnbull (Academic Press, New York, 1991).

[29] F. A. Buot, Phys. Rep. **234**, 73 (1993).

[30] S. A. Wolf, D. D. Awschalom, R. A. Buhrman, J. M. Daughton, S. von Molnár, M. L. Roukes, A. Y. Chtchelkanova, and D. M. Treger, Science **294**, 1488 (2001).

[31] D. K. Ferry and S. M. Goodnick, *Transport in Nanostructures* (Cambridge University Press, Cambridge, 1997).

[32] P. Bruno, V. K. Dugaev, and M. Taillefumier, Phys. Rev. Lett. **93**, 096806 (2004).

[33] K. von Klitzing, G. Dorda, and M. Pepper, Phys. Rev. Lett. **45**, 494 (1980).

[34] R. Landauer, Phil. Mag. **21**, 863 (1970).

[35] M. Büttiker, Y. Imry, R. Landauer, and S. Pinhas, Phys. Rev. B **31**, 6207 (1985).

[36] M. Büttiker, Phys. Rev. Lett. **57**, 1761 (1986).

[37] R. P. Feynman, *Lectures on Physics Vol.III* (Addison-Wesley, New York, 1965).

[38] R. E. Peierls, Z. Phys. **80**, 763 (1933).

[39] D. R. Hofstadter, Phys. Rev. B **14**, 2239 (1976).

[40] H. U. Baranger and A. D. Stone, Phys. Rev. B **40**, 8169 (1989).

[41] J. D. Jackson, *Classical Electrodynamics* (Wiley, New York, 1998).

[42] E. I. Rashba, Sov. Phys. Solid State **2**, 1109 (1960).

[43] Yu. A. Bychkov and E. I. Rashba, JETP Lett. **39**, 78 (1984).

[44] J. Nitta, T. Akazaki, H. Takayanagi, and T. Enoki, Phys. Rev. Lett. **78**, 1335 (1997).

[45] D. Grundler, Phys. Rev. Lett. **84**, 6074 (1999).

[46] E. N. Economou, *Green's Functions in Quantum Physics* (Springer Verlag, Berlin, 1983).

[47] G. D. Mahan, *Many Particle Physics* (Kluwer Acad./Plenum Publ., New York, 2000).

[48] F. Sols, Ann. Phys. (N.Y.) **214**, 386 (1992).

[49] D. S. Fisher and P. A. Lee, Phys. Rev. B **23**, 6851 (1981).

[50] D. Guan, U. Ravailoi, R. W. Giannetta, M. Hannan, I. Adesida, and M. R. Melloch, Phys. Rev. B **67**, 205328 (2003).

[51] M. P. Lopéz Sancho, J. M. Lopéz Sancho, and J. Rubio, J. Phys. F **15**, 851 (1985).

[52] D. J. Thouless and S. Kirkpatrick, J. Phys. C: Solid State Phys. **14**, 235 (1981).

[53] B. J. LeRoy, J. Phys.: Condens. Matter **15**, 1835 (2003).

[54] G.-P. He, S.-L. Zhu, and Z. D. Wang, Phys. Rev. B **65**, 205321 (2002).

[55] S. E. J. Shaw, Ph.D. thesis, Harvard university, 2002.

[56] H. A. Fertig and B. I. Halperin, Phys. Rev. B **36**, 7969 (1987).

[57] L. I. Glazman, G. B. Lesovik, D. E. Khmel'nitskii, and R. I. Shekhter, JETP Lett. **48**, 238 (1988).

[58] B. J. LeRoy, M. A. Topinka, R. M. Westervelt, K. D. Maranowski, and A. C. Gossard, Appl. Phys. Lett. **80**, 4431 (2002).

[59] L. Kaplan, Phys. Rev. Lett. **89**, 184103 (2002).

[60] B. J. LeRoy, M. A. Topinka, A. C. Bleszynski, R. M. Westervelt, S. E. J. Shaw, E. J. Heller, K. D. Maranowski, and A. C. Gossard, Appl. Surf. Sci. **210**, 134 (2003).

[61] J. Vaníček and E. J. Heller, Phys. Rev. E **67**, 016211 (2003).

[62] P. Muralt and D. W. Pohl, Appl. Phys. Lett. **48**, 514 (1986).

[63] J. R. Kirtley, S. Washburn, and M. J. Brady, Phys. Rev. Lett. **60**, 1546 (1988).

[64] T. Gramespacher and M. Büttiker, Phys. Rev. B **56**, 13026 (1997).

[65] T. Gramespacher and M. Büttiker, Phys. Rev. B **60**, 2375 (1999).

[66] A. Cresti, R. Farchioni, G. Grosso, and G. P. Parravicini, Phys. Rev. B **68**, 075306 (2003).

[67] A. Cresti, G. Grosso, and G. P. Parravicini, Phys. Rev. B **69**, 233313 (2004).

[68] P. W. Anderson, Phys. Rev. **109**, 1492 (1958).

[69] J. H. Davies, *The Physics of Low-Dimensional Semiconductors: an Introduction* (Cambridge University Press, Cambridge, 1998).

[70] A. Kumar, S. E. Laux, and F. Stern, Phys. Rev. B **42**, 5166 (1990).

[71] S. E. Laux, D. J. Frank, and F. Stern, Surf. Sci. **196**, 101 (1988).

[72] J. A. Nixon, J. H. Davies, and H. U. Baranger, Phys. Rev. B **43**, 12638 (1991).

[73] M. Büttiker, Phys. Rev. B **41**, 7906 (1990).

[74] F. A. Maaø, I. V. Zozulenko, and E. H. Hauge, Phys. Rev. B **50**, 17320 (1994).

[75] E. J. Heller, Phys. Rev. Lett **53**, 1515 (1984).

[76] L. P. Kadanoff and G. Baym, *Quantum Statistical Mechanics* (Benjamin, New York, 1962).

[77] P. Danielewicz, Ann. Phys. (N.Y.) **152**, 239 (1984).

[78] G. D. Mahan, Phys. Rep. **145**, 251 (1987).

[79] J. Rammer and H. Smith, Rev. Mod. Phys. **58**, 323 (1986).

[80] M. Büttiker, Phys. Rev. B **32**, 1846 (1985).

[81] J. L. D'Amato and H. M. Pastawski, Phys. Rev. B **41**, 7411 (1990).

[82] F. Gagel and K. Maschke, Phys. Rev. B **54**, 13885 (1996).

[83] T. Ando, Surf. Sci. **361**/**362**, 270 (1996).

[84] S. J. Robinson, J. Phys.: Condens. Matter **7**, 6675 (1995).

[85] P. Gartner and A. Aldea, Z. Phys. B **99**, 367 (1996).

[86] Y. Aharonov and D. Bohm, Phys. Rev. **115**, 485 (1959).

[87] P. Drude, Ann. Physik **1**, 566 (1900).

[88] R. Karplus and J. M. Luttinger, Phys. Rev. **95**, 1154 (1954).

[89] J. M. Luttinger, Phys. Rev. **112**, 739 (1958).

[90] J. Smit, Physica (Amsterdam) **24**, 39 (1958).

[91] L. Berger, Phys. Rev. B **2**, 4559 (1970).

[92] L. Berger, Phys. Rev. B **5**, 1862 (1972).

[93] Y. Taguchi, Y. Oohara, H. Yoshizawa, N. Nagaosa, and Y. Tokura, Science **291**, 2573 (2001).

[94] P. Pureur, F. Wolff Fabris, J. Schaf, and I. A. Campbell, Europhys. Lett. **67**, 123 (2004).

[95] M. V. Berry, Proc. R. Soc. London Ser. A **392**, 45 (1984).

[96] K. Ohgushi, S. Murakami, and N. Nagaosa, Phys. Rev. B **62**, (2000).

[97] S. Onoda and N. Nagaosa, Phys. Rev. Lett. **90**, 196602 (2003).

[98] G. Tatara and H. Kawamura, J. Phys. Soc. Jpn. **71**, 2613 (2002).

[99] M. Onoda, G. Tatara, and N. Nagaosa, J. Phys. Soc. Jpn. **73**, 2624 (2004).

[100] A. Shapere and F. Wilczek, *Geometric Phases in Physics* (World Scientific, Singapore, 1989).

[101] A. Bohm, *The Geometric Phase in Quantum Systems: Foundations, Mathematical Concepts, and Applications in Molecular and Condensed Matter Physics* (Springer, Berlin, 2003).

[102] B. R. Holstein, Am. J. Phys. **57**, 1079 (1989).

[103] J. F. Zwanziger, M. Koenig, and A. Pines, Annu. Rev. Phys. Chem. **41**, 601 (1990).

[104] P. Bruno, in *Lecture Manuscripts of the* 36^{th} *Spring School of the Institute of Solid State Research: Magnetism goes Nano*, Vol. 26 of *Schriften des Forschungszentrum Jülich Reihe Materie und Material*, edited by S. Blügel, T. Brückel, and C. M. Schneider (Forschungszentrum Jülich GmbH, Jülich, 2005), cond-mat/0506270.

[105] L. I. Schiff, *Quantum Mechanics* (McGraw-Hill, New York, 1968).

[106] F. Wilczek and A. Zee, Phys. Rev. Lett. **52**, 2111 (1984).

[107] Y. Aharonov and J. Anandan, Phys. Rev. Lett. **58**, 1593 (1987).

[108] P. W. Anderson and H. Hasegawa, Phys. Rev. **100**, 675 (1955).

[109] D. Loss, H. Schöller, and P. M. Goldbart, Phys. Rev. B **48**, 15218 (1993).

[110] D. Loss, H. Schöller, and P. M. Goldbart, Phys. Rev. B **59**, 13328 (1999).

[111] A. Stern, Phys. Rev. Lett. **68**, 1022 (1992).

[112] S. A. van Langen, H. P. A. Knops, J. C. J. Paasschens, and C. W. J. Beenakker, Phys. Rev. B **59**, 2102 (1999).

[113] M. Popp, D. Frustaglia, and K. Richter, Phys. Rev. B **68**, 041303 (2003).

[114] J. Sinova, S. Murakami, S.-Q. Shen, and M.-S. Choi, , cond-mat/0512054.

[115] E. I. Rashba, Phys. Rev. B **68**, 241315 (2003).

[116] J. Shi, P. Zhang, D. Xiao, and Q. Niu, Phys. Rev. Lett. **96**, 076604 (2006).

[117] I. Turek, V. Drchal, J. Kudrnovský, M. Šob, and P. Weinberger, *Electronic Structure of Disordered Alloys, Surfaces and Interfaces* (Kluwer, Boston, 1997).

[118] C. Caroli, R. Combescot, P. Nozieres, and D. Saint-James, J. Phys. C: Solid St. Phys. **20**, 1018 (1965).

[119] L. V. Keldysh, Sov. Phys. JETP **20**, 1018 (1965).

[120] I. N. Bronstein and K. A. Semendjajew, *Taschenbuch der Mathematik* (Nauka, Moscow, 1981).

[121] L. J. van der Pauw, Philips Res. Repts. **13**, 1 (1958).

[122] I. Janeček and P. Vašek, Physica C **402**, 199 (2004).

Eidesstattliche Erklärung:

Hiermit erkläre ich, dass ich keine anderen als die von mir angegebenen Quellen und Hilfsmittel zur Erstellung meiner Dissertation verwendet habe. Den benutzten Werken wörtlich oder inhaltlich entnommene Stellen sind als solche gekennzeichnet. Die Dissertation wurde bisher an keiner anderen Universität oder Hochschule vorgelegt.

Halle (Saale), den 19. Februar 2007,

Georgo Metalidis

Curriculum Vitae

Personal data:

Name: Georgo Jan Metalidis
Date of birth: June 18, 1980
Place of birth: Genk, Belgium

Education:

September 1985 - June 1992:
Primary school "Vrije basisschool - Oud Waterschei", Genk, Belgium

September 1992 - June 1998:
Secondary school "Sint-Jan-Berchmanscollege Genk", Genk, Belgium

September 1998 - July 2000:
Faculty of Physics at "Limburgs Universitait Centrum", Diepenbeek, Belgium

September 2000 - August 2003:
Faculty of Applied Physics at "Technische Universiteit Eindhoven", Eindhoven, The Netherlands.
Master of science in applied physics with the thesis: *Strongly correlated bosons in one-dimensional optical lattices*.
Thesis was prepared at the "Max-Planck-Institute of Quantum Optics", Garching, Germany, under supervision of Prof. Dr. J.I. Cirac.

October 2003 - October 2006:
Ph.D. candidate at the "Max-Planck-Institute of Microstructure Physics", Halle, Germany. Supervisor: Prof. Dr. Patrick Bruno

List of Publications:

- G. Metalidis and P. Bruno, *Magnetic Casimir effect*, Phys. Rev. A **66**, 062102 (2002).
- G. Metalidis and P. Bruno, *Green's function technique for studying electron flow in two-dimensional mesoscopic samples*, Phys. Rev. B **72**, 235304 (2005).
- G. Metalidis and P. Bruno, *Inelastic scattering effects and the Hall resistance in a four-probe ring*, Phys. Rev. B **73**, 113308 (2006).
- G. Metalidis and P. Bruno, *Topological Hall effect studied in simple models*, Phys. Rev. B **74**, 045327 (2006).